Exploring the Nature of Chemically Exfoliated Molybdenum Disulfide and the Design of a Heterointerface Structure for Photocatalytic Applications

LEANDDAS NURDIWIJAYANTO

May 2018

Exploring the Nature of Chemically Exfoliated Molybdenum Disulfide and the Design of a Heterointerface Structure for Photocatalytic Applications

LEANDDAS NURDIWIJAYANTO
Doctoral Program in *Materials Science and Engineering*

Submitted to the Graduate School of
Pure and Applied Sciences
in Partial Fulfilment of the Requirements
for the Degree of Doctor of Philosophy in
Engineering

at the
University of Tsukuba

ABSTRACT

This thesis describes detailed studies on the nature of chemically exfoliated molybdenum disulfide (MoS_2) nanosheets in an aqueous suspension and their potential application as building blocks for the fabrication of a new class of photocatalyst materials when coupled with titanium dioxide nanosheets ($Ti_{1-\delta}O_2^{4\delta-}$). The unique and attractive properties of 2D nanomaterials have triggered tremendous interest in exploring new intriguing properties for various applications. In particular, the hetero-assembly of two types of 2D nanomaterials has emerged as an attractive strategy to design new and unique artificial materials and systems, which offer an opportunity to discover unprecedented functionalities that arise from intimate interfacial interactions. Although most fundamental studies of 2D heterostructures have been carried out on specimens fabricated *via* the scotch-tape transferring method, a large-scale production process is necessary for practical applications. Therefore, solution-based assembly techniques (*e.g.,* Langmuir-Blodgett, sequential electrostatic adsorption, and spontaneous flocculation) have been considered to be an alternative, through which a wide variety of nanosheets can be easily integrated into desired structures from their colloidal form.

Molybdenum disulfide (MoS_2) is an important inorganic two-dimensional nanomaterial that is the member of the family of layered transition metal dichalcogenides. MoS_2 has been attracting considerable attention because of the intriguing electronic properties, showing a semiconducting band gap transition from an indirect (1.2 eV) when in the bulk form to a direct band gap (1.9 eV) upon reducing the thickness toward single layer. In addition, MoS_2 adopts two distinct crystal structures, *i.e.,* a trigonal prismatic 2H phase (semiconducting) and an octahedral 1T (metallic). Due to these unique properties, MoS_2 offers a wide range of potential applicability's in electronics and optoelectronics, energy conversion and storage, and catalysis. Large-scale production of MoS_2 nanosheets can be prepared *via* chemical exfoliation, where a colloidal form of unilamellar MoS_2 nanosheets is achieved by treating the Li-intercalated MoS_2 crystals with water under ultrasonication. Although this process was established more than three decades ago, detailed studies on the underlying mechanism, production of high-quality nanosheets, and long-term stability have been limited. One challenge arising from MoS_2 nanosheets, prepared *via* the chemical exfoliation, is the instability of the resultant colloidal suspension, causing it to aggregate over time, which certainly hampers the utilization of these nanosheets. Therefore, the present study examines the nature and behavior of chemically exfoliated MoS_2, particularly in terms of their suspension stability, morphology, chemical and electronic nature, and phase and 2D structure.

The nature and behavior of chemically exfoliated MoS_2 nanosheets were studied in two different atmospheric conditions, *i.e.*, inert N_2 gas and ambient air. Since chemical exfoliation of MoS_2 applies a reductive intercalation *via* a reaction with *n*-butyllithium, it is hypothesized that the stability and quality of chemically exfoliated MoS_2 nanosheets may be associated with a redox process. The UV-visible absorption spectra of the suspension sample stored in ambient air exhibited a drastic change with time by decreasing its absorbance over the whole measured wavelength range. These changes were accompanied by lateral

fracturing of the nanosheets into smaller fragments. By contrast, these changes were hardly observed when storing the suspension in an inert N_2 gas. X-ray photoelectron spectroscopy analysis indicated that exposing the suspensions to ambient air led to reoxidation of the nanosheets, during which the nanosheets released their residual negative charges into the environment, accompanied by the restoration of the oxidation states to the original Mo^{4+}. The restacking of the nanosheets provided an important information on the behavior of the reoxidation process, in which the chemical-nature changes of the nanosheets were studied from the structural evolution of the restacked nanosheets. The restacked nanosheets from the freshly as-prepared suspension exhibited an expanded structure due to intercalation of the bilayer hydrates accommodating Li-ions. Upon aging of the suspension, the bilayer-hydrate structure gradually collapsed into a deintercalated phase. Eventually, the deintercalated phase became dominant and the bilayer hydrates totally disappeared. This structural evolution suggested that the reoxidation process proceeded sheet by sheet and the oxidation state of the nanosheets directly restored to the original Mo^{4+}. Consequently, the oxidation states of the sheets might be discrete only at two values of 4+ and (4–δ)+. A continuous change of the oxidation state should not be possible upon the reoxidation. In-plane XRD and electron diffraction pattern analyses indicated that the nanosheets retained their 1T phase upon the reoxidation, suggesting the formation of metastable neutral 1T MoS_2.

In the second step, the author attempts to utilize the prepared MoS_2 nanosheets as a building block to design a new class of photocatalyst materials from the hetero-assembly with $Ti_{1-\delta}O_2^{4\delta-}$ nanosheets. A two-dimensional (2D) heterointerface structure was constructed from a monolayer modification of restacked $Ti_{0.87}O_2^{0.52-}$ nanosheets with metallic 1T-phase MoS_2 *via* a facile two-step flocculation of their colloidal suspensions. This modification was found to be driven by the difference in the critical concentrations of H^+ ions required for inducing flocculation of the respective nanosheets, allowing the attachment of monolayer 1T-phase MoS_2 on restacked $Ti_{0.87}O_2^{0.52-}$ nanosheets. The process resulted in the porous flaky microstructure of $Ti_{0.87}O_2^{0.52-}/MoS_2$ crystallites, which is beneficial for photocatalytic applications due to the largely exposed MoS_2 surface serving as an electron collector and catalytically active site. As a result, the MoS_2-modified restacked-$Ti_{0.87}O_2^{0.52-}$ nanosheets showed highly efficient photocatalytic activity for hydrogen generation from an aqueous methanol solution (~1.2 mmol h^{-1} g^{-1}), which was three times higher than those of control samples from physical mixtures of bulk aggregates of independently flocculated $Ti_{0.87}O_2^{0.52-}/MoS_2$ nanosheets and composites of P25-nanoparticles/MoS_2. The monolayer attachment of metallic MoS_2 on restacked $Ti_{0.87}O_2^{0.52-}$ nanosheets was demonstrated to significantly enhance the yield of evolved hydrogen. The enhancement could be ascribed to the extensive molecular-level interfacial contact between the 2D nanosheets, which could not be achieved with conventional hybridization of the bulk or nanoparticle counterparts. This study provides a novel strategy for the versatile fabrication of specially designed hybrid materials made of different 2D molecularly thin nanosheets. In addition, the designed hybrid structure may offer a promising pathway for a range of applications, such as catalysis/photocatalysis, energy conversion and storage, and even optoelectronics.

Table of Contents

List of Figures

List of Tables

This page is intentionally left blank

Chapter 1.
Introduction

1.1. Background

1.1.1. Two-dimensional (2D) Nanomaterials

The downscaling of particle dimensions at the nanometer scale[1] significantly alters the physicochemical properties of a material, in which the reactivity is controlled by the integration of a number of atoms or molecules within the materials.[2] Such low-dimensional particles bring about tremendous interest from the viewpoints of both fundamental sciences and practical applications. To this aspect, size-dependent quantum effects have been demonstrated, such as surface plasmon resonance in metallic nanoparticles,[3–5] quantum confinement in semiconducting materials,[6–9] and superparamagnetism or superconductivity in magnetic materials.[10–13]

On the basis of geometry, nanomaterials are classified into four dimensions, *i.e.*, three dimensional (3D) such as nanoparticles, nano-flower, nano-cones, *etc.*, two dimensional (2D) such as nanosheets, one dimensional (1D) such as nanotubes, nanowires, and nanorods, and zero dimensional (0D) such as quantum dots, fullerenes, and so on. Interestingly, it is not only the size of the nanomaterial but also the dimensionality that acts as one of the most contributing factors in determining the properties.[2] For instance, allotropes of sp^2 carbon such as fullerenes (0D), carbon nanotubes (1D), graphene (2D), and graphite (3D) exhibit very distinct physicochemical properties from one to another.

Particular research attention has been addressed to two-dimensional (2D) nanomaterials since the successful isolation of graphene (a monolayer of carbon atoms arranged in a 2D honeycomb lattice) from layered graphite crystals, followed by the discovery of its extraordinary mechanical, electronic, and optical properties by Geim *et al*. in 2004.[14] Following this discovery, graphene has been extensively explored for use in many applications, ranging from next-generation electronics and optoelectronic devices (such as transistors, photodetectors, sensors, *etc*.) to energy storage and conversion systems (such as Li-ion batteries, photovoltaics, photocatalysts for hydrogen generation, *etc*.).[15,16] However, graphene is a semimetal and a simple material with only one element (carbon), which sometimes limits its versatility in terms of structure, composition, and functionality. This limitation drives a motivation to discover alternative 2D nanomaterials with diverse compositions, structures, and functionalities.[17–20]

Recently, the family of 2D nanomaterials has begun to grow consistently. For example, inorganic nanosheets have been derived from layered transition-metal oxides.[21–24] This aspect enriches the diversity of crystal structures and chemical compositions of 2D nanomaterials. To this point, various transition-metal oxide nanosheets have been successfully synthesized thus far, such as $Ti_{0.91}O_2^{0.36-}$,[25,26] $Ca_2Nb_3O_{10}^-$,[27–30] $MoO_2^{\delta-}$,[31] $MnO_2^{0.4-}$,[32–34] $Nb_6O_{17}^{4-}$,[35] TaO_3^-,[36] $TiNbO_5^-$,[37–40] and $Cs_4W_{11}O_{36}^{2-}$.[41] Typically, the exfoliated oxide nanosheets exhibit wide band-gap semiconducting properties for those based on Ti, Nb,

and Ta, and hold great promise for use in high-*k* dielectrics, magneto-optics, photocatalysis, and so on.[22,23] In contrast, a reversible redox activity has been demonstrated for those based on Mn, Mo, and W, which suggests their potential for use in photochemistry, photochromic, and energy storage applications.[33,42–45] It is also possible to tune the chemical composition of the nanosheets by chemical doping with transition metals (Fe, Co, *etc*.) to produce fascinating optical, electronic, magnetic, and catalytic properties, which has increasingly attracted the research attention.[21,22,46–48]

Single-layer hydroxide nanosheets are another class of 2D nanomaterials derived from the delamination of layered metal hydroxides.[21,49–51] Typically, they show a facile redox activity, which makes them suitable for use in catalysis and energy storage applications.[52–58] Recently, rare-earth-based hydroxide nanosheets with interesting luminescent properties have been successfully delaminated from layered rare-earth hydroxides $RE(OH)_{2.5}xH_2O\cdot A^{n-}_{0.5/n}$ (RE = Nd, Sm, Eu, Gd, Tb, Dy, Ho, Er, Tm, Yb, Lu, Y).[50,59–64] Hydroxide-based nanosheets are of particular interest because positively charged nanosheets can only be produced from this type of nanosheet. This feature makes it possible to fabricate a unique superlattice structure by hetero-assembly with positively charged nanosheets such as reduced graphene oxide,[65,66] highlighting the possibility for facile design of an artificial structure.

Another example of 2D nanomaterials analogous to graphene are those based on layered transition metal dichalcogenides (LTMDs), which exhibit diverse properties ranging from semiconductors (MoS_2, $MoSe_2$, and WS_2), semimetals ($TiSe_2$ and WTe_2), true metals (NbS_2 and VSe_2), and insulators (HfS_2).[17,67–70] Generally, they have a sandwich layered structure in the form of X-M-X, where M is the transition metal from group IV, V, or VI, and X is the chalcogen atom such as S, Se, or Te. Similar to layered graphite, the interlayers of LTMD materials are weakly bound by van der Waals forces. This feature makes the LTMD materials relatively easy to exfoliate using simple scotch tape mechanical cleavage. Semiconductor TMD materials typically show interesting electronic properties, where the characteristics of the electronic band gap can be tuned upon reducing the layer thickness (Table 1.1).[67,71] In addition, the electronic band gap also varies with the composition.[67] These unique characteristics are attractive for use in electronic and optoelectronic devices as a supplementary to the zero band gap of graphene.

Table 1.1. Electronic band gaps of bulk and monolayer TMD semiconductor materials.[67]

TMD	Electronic band gap (eV)	
	Bulk	Monolayer
$MoTe_2$	1.0	1.1
$MoSe_2$	1.1	1.5
WSe_2	1.2	1.6
MoS_2	1.2	1.8
WS_2	1.4	2.1

1.1.2. Molybdenum Disulfide (MoS_2) Nanosheets

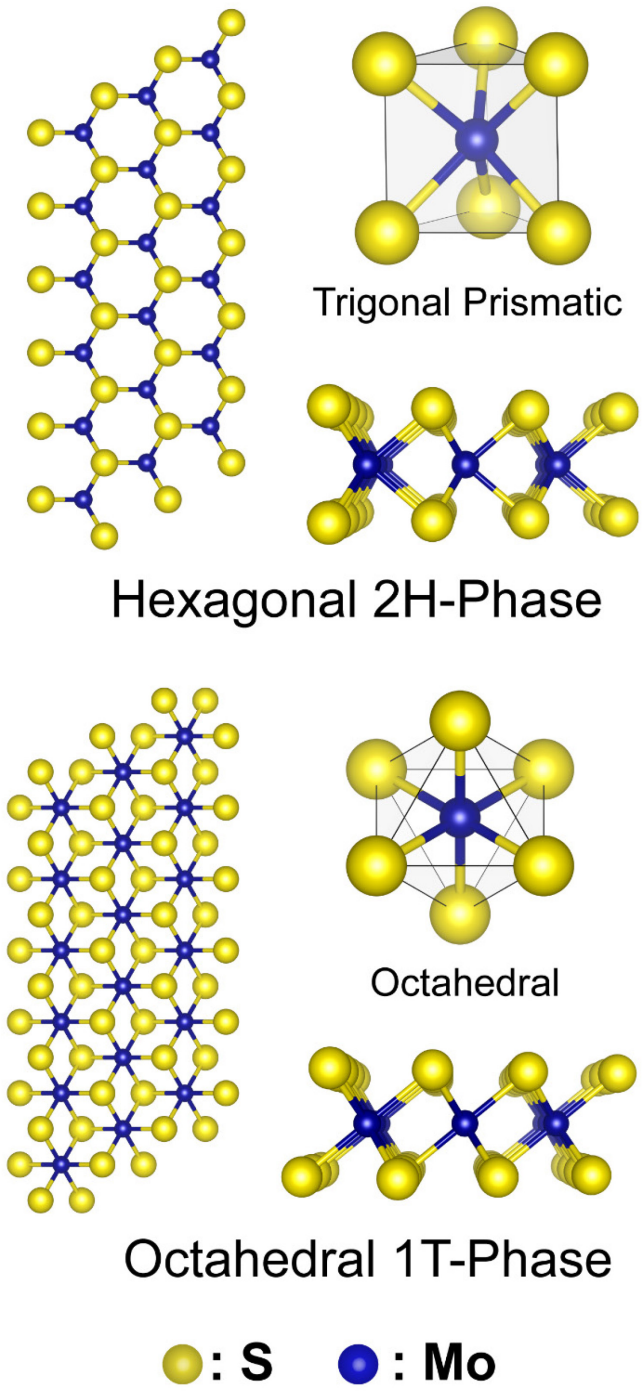

Figure 1.1. Schematic crystal structures of 2H and 1T polytypes.

Molybdenum disulfide (MoS_2) is one of the most studied and widely used layered materials from the transition metal dichalcogenides due to its versatile abundance in nature.[71–74] To this benefit, MoS_2 has a long history of applications in solid state lubricants,[75–77] photovoltaic devices,[78–80] hydrodesulfurization

catalysts,[81,82] and rechargeable batteries.[83] In light of these longstanding historical benefits, MoS_2 has recently been considered as one of the most promising semiconductors due to its thickness-dependent electronic properties.[73,84–86] These unique properties has opened up new possibilities to utilize single-layer MoS_2 nanosheets in electronic and optoelectronic devices.[17,67,68,84,87,88] MoS_2 nanosheets have also shown a promising applicability as an electrode in electrocatalysis and Li-ion batteries.[89–92] Therefore, MoS_2 offers a wide range of potential applications from electronics and optoelectronics to energy storage and catalysis.

In general, MoS_2 nanosheets have two polytypes, *i.e.*, 2H and 1T,[93] which depend on the coordination of sulfur atoms with respect to the molybdenum atom as the metal center (Figure 1.1). The coordination environment of the molybdenum atom determines the electronic structure of MoS_2, either semiconducting or metallic. From these two polytypes, only 2H MoS_2 can be found stable in nature.[93–95] In the 2H polytype, the molybdenum atoms exhibits a trigonal prismatic coordination, with the crystallographic parameters as follows: the nearest Mo–S distance is 2.41 Å, and the thickness of the layer (S to S in the *c* direction) and the distance between adjacent layers are 3.15 and 3.49 Å, respectively.[94] 2H MoS_2 is a semiconductor because the *d* orbitals of the metal center are fully occupied. In contrast, 1T MoS_2 adopts an octahedral coordination for the molybdenum atoms, where the *d* orbitals of the metal center are partially filled. Thus, 1T MoS_2 exhibits a metallic property. 1T MoS_2 is not available in nature and can only be synthesized through the intercalation of pristine MoS_2 with alkali metals, through which the MoS_2 undergoes a structural transformation from trigonal prismatic to octahedral.[96,97]

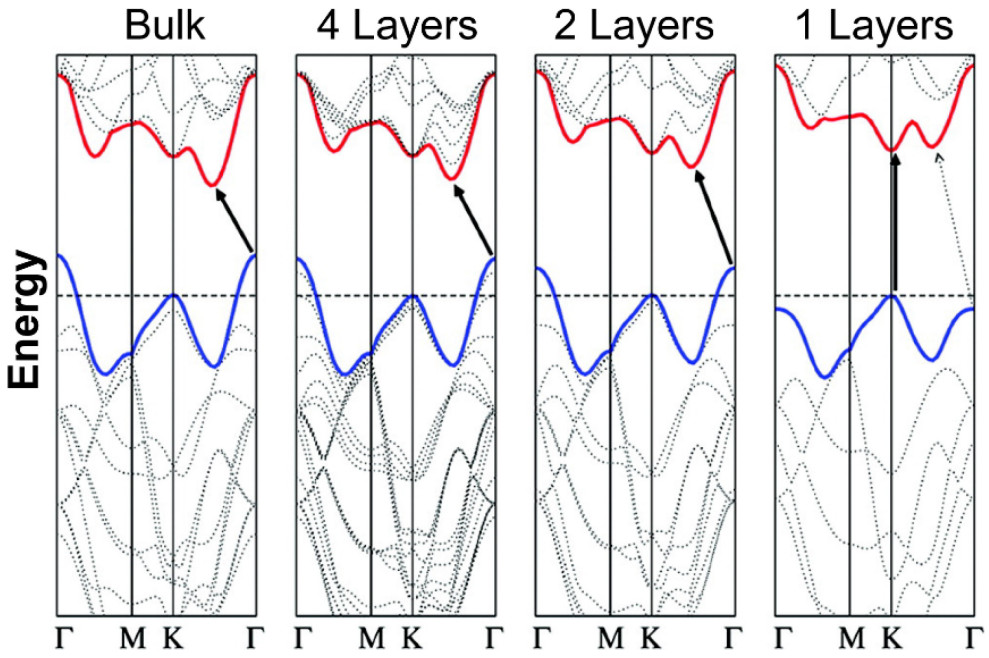

Figure 1.2. Calculated band structures of bulk to single-layer MoS_2. Adapted with permission from Ref. 99. Copyright 2010 American Chemical Society.

As has been briefly described above, one of the intriguing properties of 2H MoS_2 nanosheets is the thickness-dependent band gap that changes from a semiconducting indirect (~1.2 eV)[79,98] when in the bulk form to a direct band gap (~1.9 eV) when reducing the thickness towards single layer (Figure 1.2).[87,99] This discovery is significant because such an intriguing electronic property cannot be obtained from graphene, a native semimetal 2D nanomaterial. Thus, this completes the range of choice of 2D materials from conductor (such as graphene), insulator (such as hexagonal boron nitride (h-BN)), and now semiconductor (such as single-layer MoS_2). Consequently, the emergence of an intrinsic band gap in single-layer MoS_2 has triggered tremendous interest in utilizing it for 2D-based electronic devices.

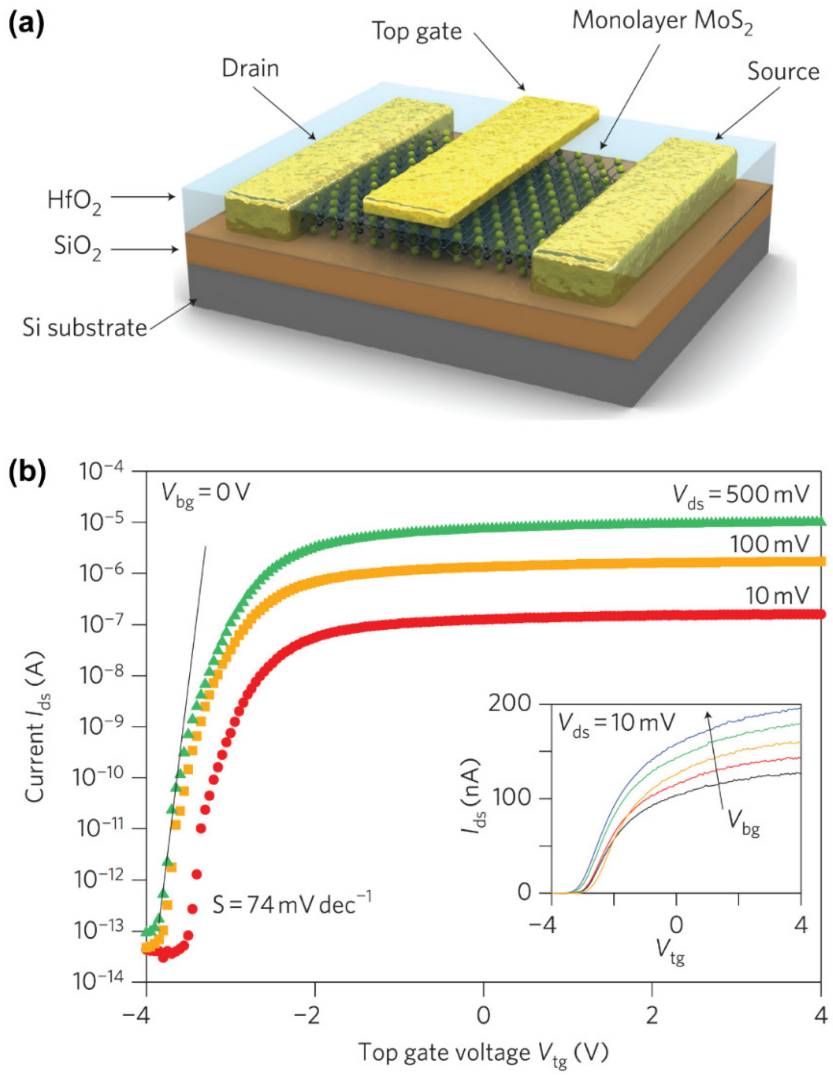

Figure 1.3. (a) Device configuration and (b) electrical characteristics of a single-layer MoS_2 FET device. Adapted with permission from Ref. 88. Copyright 2011 Nature Publishing Group.

For instance, the first report on the utilization of single-layer MoS_2 in an electronic device dates back to 2005 and was introduced by Novoselov *et al.*, where single-layer MoS_2 was mechanically cleaved upon

a Si substrate (300-nm-thick SiO_2 layer) and used as a channel in a field-effect transistor (FET) device.[17] The electrical properties of the fabricated FET device were measured using SiO_2 as the dielectric layer for the back gate, resulting in a relatively low mobility of 3 cm^2 V^{-1} s^{-1}. In 2010, a major breakthrough was introduced by Kis *et al.* by fabricating a top-gated MoS_2 transistor with HfO_2 as the dielectric layer (Figure 1.3a).[88] As a result, this configuration achieved a very high mobility of ~200 cm^2 V^{-1} s^{-1}, high ON/OFF ratios of $>10^8$, and high ON currents of ~2.5 μA $μm^{-1}$ at a drain source voltage of 500 mV (Figure 1.3b). In addition, a sharp turn-on characteristic was achieved as observed from a sub-threshold of 74 mV dec^{-1}, which is better than the theoretical limit for classical transistors (60 mV dec^{-1}). Such efficient device performance with low power dissipation is promising for future electronics, which requires a low stand-by power.

The other polytype, metallic 1T MoS_2, has also been a research interest. For instance, 1T MoS_2 has been used as a host material in intercalation chemistry, which can accept intercalates from small ions such as Li and Na to macromolecules.[100–102] To this aspect, 1T MoS_2 has been widely studied as an anode in Li-ion batteries and supercapacitors.[89,90,103–106] MoS_2 has been demonstrated to show a high specific capacity of 907 mA h g^{-1} at 10 C after 50 cycles (higher than graphite, ~300 mA h g^{-1}), an excellent rate capability of ~550 mA h g^{-1} at a rate of 50 C for 20 cycles, and a good capacity retention.[107] 1T MoS_2 has also demonstrated a promising performance for use in supercapacitors. This aspect has been driven by the superior electrical conductivity of the 1T phase and its excellent behavior as an intercalation host. Recently, restacked 1T MoS_2 nanosheets were reported to show exceptionally high value of volumetric capacitance ranging from 400 to 650 F cm^{-3} at a scan rate of 20 mV s^{-1}, depending on the electrolyte used.[104] The excellent metallic conductivity of 1T MoS_2 is also beneficial for catalysis of hydrogen evolution reaction (HER), being superior to that of the 2H counterpart.[108,109] The utilization of metallic 1T MoS_2 resulted in efficient HER activity, showing a Tafel slope of 40 to 43 mV per decade. In addition, 1T MoS_2 has been shown to be catalytically active on both basal surfaces and at its edges, which brings particular advantages for catalytic HER applications.

1.1.3. MoS_2-based 2D Heterostructures

The development of functional nanostructured materials based on 2D nanomaterials has become a fascinating research direction.[23,110–113] The utilization of nanosheets as building blocks is of particular interest due to their unique 2D structure, and the hetero-assembly of two types of 2D nanomaterials has come up as fascinating strategy to design/control of unprecedented functionality, originating from the intimate interfacial interactions in such novel artificial materials and systems.[21,114–119] As a result, strong coupling effects at the location of intimate interaction would greatly tune the physical properties of the individual components, leading to new or enhanced functionalities that cannot be achieved with a single component. This strategy opens up the feasibility to organize artificial materials of sophisticated tailoring with a high freedom of material design, which are distinct from traditional growth methods.

For instance, a vertical heterostructure of single-layer graphene on h-BN has been demonstrated to show a Hofstadter's butterfly effect that had been predicted more than 40 years ago.[120,121] In another system, the coexistence of superconductivity and magnetism has been demonstrated by a superlattice structure composed of superconducting-TaS_2 and magnetic-double-hydroxide layers.[122] In our previous studies, our group has demonstrated the evolution of novel functionalities from the superlattice assembly of various oxide nanosheets, such as significant enhancements in the magneto-optical response of Co/Fe-substituted titania nanosheets ($Ti_{0.8}Co_{0.2}O_2^{0.4-}$/$Ti_{0.6}Fe_{0.4}O_2^{0.4-}$),[123] ferroelectricity of two-different dielectric nanosheets ($LaNb_2O_7^-$/$Ca_2Nb_3O_{10}^-$),[124] and photochemical modulation and photoinduced charge accumulation of $Ti_{1-\delta}O_2^{4\delta-}$ nanosheets with $MnO_2^{0.4-}$ nanosheets[125] and r-GO,[126] as well as the development of new artificial multiferroic materials with a $Ti_{0.8}Co_{0.2}O_2^{0.4-}$/$Ca_2Nb_3O_{10}^-$ superlattice.[127]

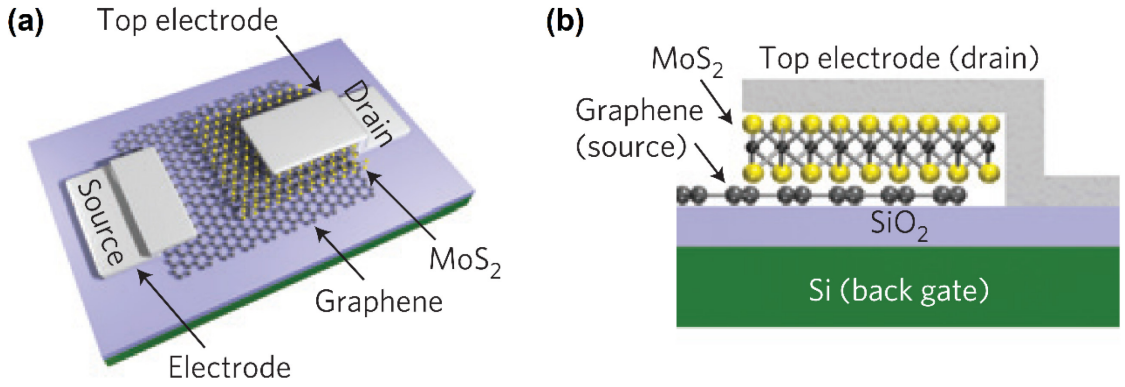

Figure 1.4. Schematic illustration of (a) the three-dimensional view and (b) the side view of the device layout. The graphene and top metal thin-film (Ti/Au: 50/50 nm) act as the source and drain electrodes, respectively. The MoS_2 layer act as the semiconducting channel. Reproduced with permission from Ref. 128. Copyright 2013 Nature Publishing Group.

To date, the most studied MoS_2-based 2D-heterostructures have typically been limited to those with graphene, with the following being representative examples. Duan *et al*. reported a vertically stacked graphene/MoS_2 heterostructure for FET device applications (Figure 1.4).[128] First, graphene was grown by chemical vapor deposition and then transferred onto a Si/SiO_2 substrate. The MoS_2 flakes were exfoliated onto the graphene using a micromechanical cleavage method. The top metal electrode, composed of Ti/Au (50/50 nm), was deposited on the MoS_2 by electron-beam deposition. The fabricated heterostructure exhibited an excellent performance for a FET device, showing a high current density of up to 5000 A cm^{-2} and a high on/off ratio of $>10^3$. The output characteristic of the vertically stacked graphene/MoS_2 heterostructure was approximately 20 times larger than that of planar MoS_2 alone. The same group also reported a sandwich heterostructure of a few layers of MoS_2 with graphene for a photodetector application (Figure 1.5a).[129] The vertical graphene/MoS_2/graphene device was fabricated on an Si/SiO_2 substrate (300 nm SiO_2) by the scotch tape transferring process. As shown in Figure 1.5b, the fabricated device exhibited

a clear photoresponse with an open-circuit voltage and short-circuit current of approximately 0.3 V and ~2 mA, respectively. In addition, the photoresponse could be modulated by an external back-gate voltage, opening up possibilities to manipulate the generation of photocarriers, charge separation, and the transport process in the vertically stacked device. For example, the external quantum efficiency of such a device was increased from ~6% to ~15% by changing the back-gate voltage form 60 V to –60 V. Such unique features offer the intriguing possibility for designing future photodetection and photovoltaic devices.

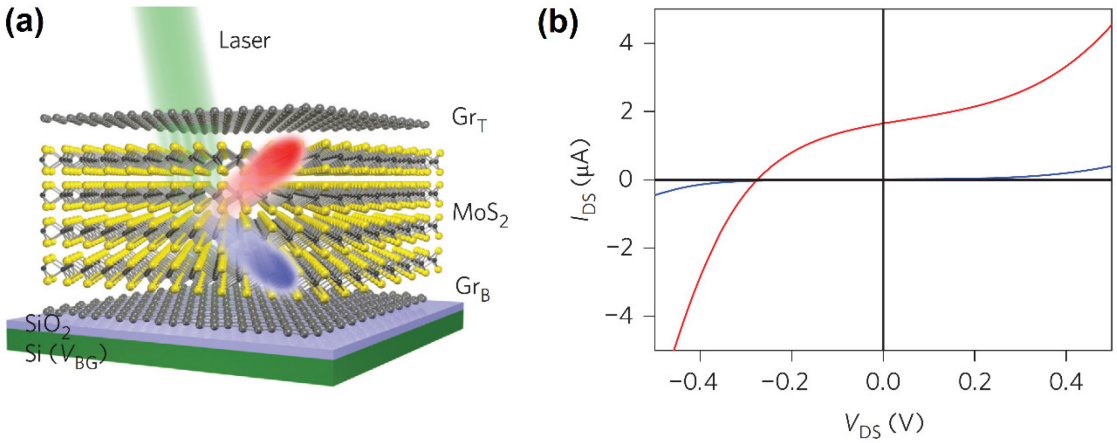

Figure 1.5. (a) Schematic illustration of vertical graphene–MoS_2–graphene devices. Red and blue colors indicate electrons and holes, respectively. (b) *I-V* characteristic in the dark (blue) and under illumination (red) (by a focused laser beam; λ = 514 nm; intensity: 80mW). Adapted with permission from Ref. 129. Copyright 2013 Nature Publishing Group.

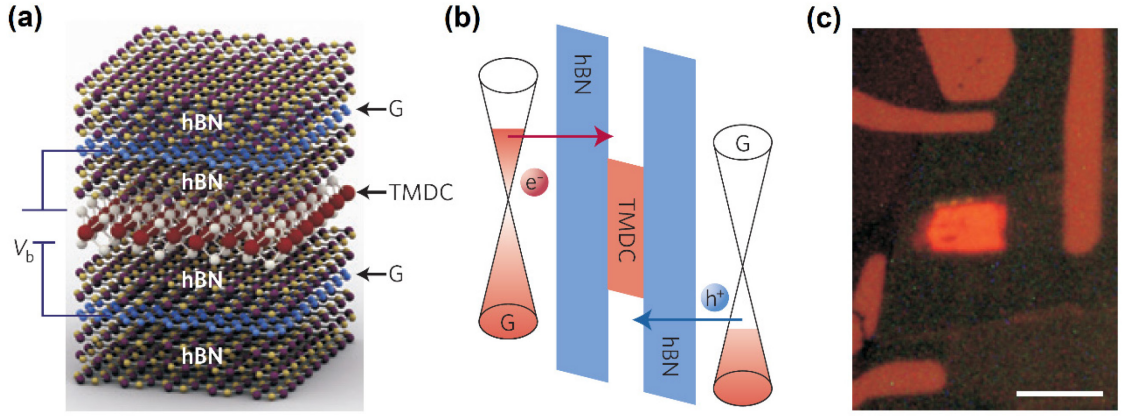

Figure 1.6. Vertical heterostructure of three different 2D nanomaterials (graphene, h-BN, and MoS_2), showing an intriguing function as a LED device. (a) Schematic of the vertical heterostructure device (G: Graphene, h-BN: hexagonal boron nitride, and TMDC: transition metal dichalcogenide crystal (MoS_2)). (b) Electronic band diagram of the LED heterostructure device under an applied bias. (c) Photograph of the

LED heterostructure device emitting red light (dimensions: approx. 5 × 10 μm). Adapted with permission from Ref. 130 and 131. Copyright 2015 Nature Publishing Group.

Another intriguing MoS_2-based heterostructure has been realized by the simultaneously hetero-assembly of graphene and h-BN for a light emitting diode (LED) device application, according to the structure depicted in Figure 1.6a.[130,131] In this case, the h-BN layers, positioned in between the graphene and monolayer MoS_2, functioned as a tunneling barrier, as well as serving to minimize the quenching of light emission. It is known that emission in monolayer MoS_2 is dominated by excitons (bound state of electron-hole pairs) due to the enhanced Coulombic interaction. The injected electrons from the graphene layers (Figure 1.6b) relax the formation of excitons in the MoS_2 layer. The recombination of the electron-hole pairs of the excitons results in light emission. MoS_2 has also been widely hetero-assembled with other TMD nanomaterials. For example, Wei *et al*. demonstrated the vertical hetero-assembly of MoS_2 and WS_2 in a FET device.[132] The fabricated device achieved high field-effect ON/OFF ratio of $>10^5$ with electron mobility of 65 $cm^2\ V^{-1}\ s^{-1}$. Duan *et al*. fabricated WSe_2/MoS_2 heterostructure *p-n* diodes, which demonstrated electroluminescence and photocurrent generation activities with an EQE of up to 12%.[133] Such a synergetic effect is remarkably superior compared to a device fabricated from planar MoS_2 alone, which typically shows an EQE <1%.

1.1.4. Prospect of the 2D Hetero-assembly of MoS_2 with Oxide Nanosheets

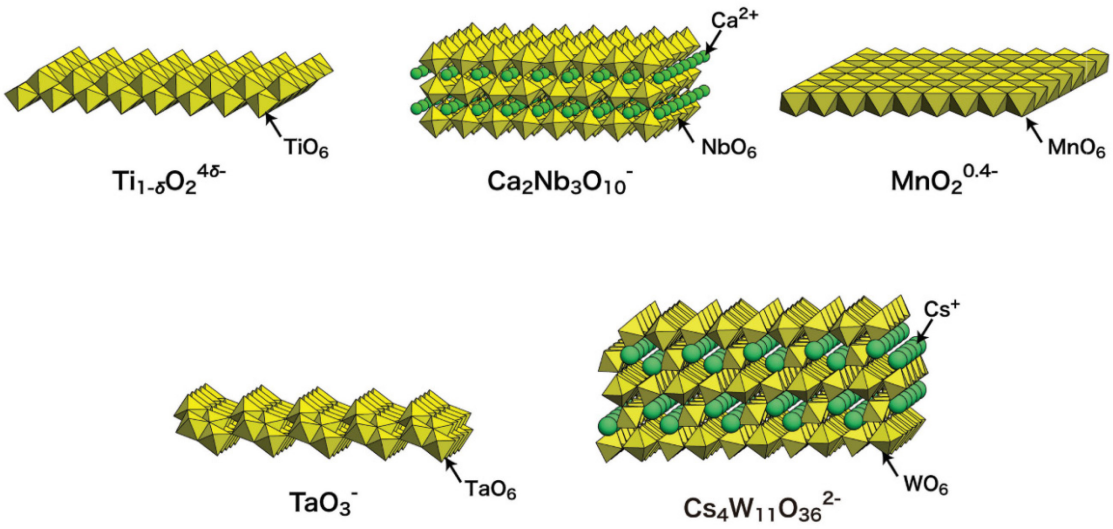

Figure 1.7. Schematic structural representation of typical oxide nanosheets. $Ti_{1-\delta}O_2^{4\delta-}$: titanium oxide, $Ca_2Nb_3O_{10}^-$: calcium niobium oxide, $MnO_2^{\delta-}$: manganese oxide, TaO_3^-: tantalum oxide, and $Cs_4W_{11}O_{36}^{2-}$: cesium tungsten oxide. Adapted with permission from Ref. 21. Copyright 2010 John Wiley and Sons.

Thus far, the 2D hetero-assembly of MoS_2 with oxide nanosheets has been underexplored. Most reports have only published on the random hybridization of MoS_2 and oxide materials without precise control of the nanostructures, with typical applications in energy storage and catalysis.[134–139] Therefore, there remains plenty room for the exploration of intriguing functions that may arise from the interfacial interaction of monolayer MoS_2 and oxide nanosheets. Our group has successfully demonstrated the preparation of various oxide nanosheets (Figure 1.7) such as $Ti_{0.91}O_2^{0.36-}$, $Ca_2Nb_3O_{10}^-$, $MnO_2^{\delta-}$, TaO_3^-, and $Cs_4W_{11}O_{36}^{2-}$ by the soft-chemical delamination of layered metal oxides (*e.g.*, $Cs_{0.7}Ti_{1.825}O_4$,[25,26] $KCa_2Nb_3O_{10}$,[29,30] $K_{0.45}MnO_2$,[33] $RbTaO_3$,[36] and $Cs_{6+x}W_{11}O_{36}$[41]). The exfoliated nanosheets exhibit distinct physicochemical properties, depending on their composition and structure. Furthermore, the molecular-level 2D confinement in nanosheets can significantly alter the electronic structure and induce novel physical phenomena that emerge due to the quantum confinement effect.[21,22,113] Table 1.2 summarizes the physical properties of some oxide nanosheets.

To date, most of the synthesized oxide nanosheets have been based on d^0 transition metal oxides (*e.g.*, Ti^{4+}, Nb^{5+}, Ta^{5+}, W^{6+}, and so on), where the empty *d* orbitals of the transition metal overlap with the filled *p* orbitals of the oxygen ligands.[22] These oxide nanosheets are typically wide band-gap semiconductors. Although they are not electronically interesting, they hold potential as semiconducting hosts, photocatalysts, or high-*k* dielectric materials.[21,22] For instance, $Ti_{1-\delta}O_2^{4\delta-}$ and $Ca_2Nb_3O_{10}^-$ nanosheets exhibit attractive photochemical and dielectric properties.[24] Reversible redox active properties are shown in $MnO_2^{\delta-}$, $RuO_{2.1}^{\delta-}$, and $Cs_4W_{11}O_{36}^{2-}$ nanosheets.[21,113] Among them, $RuO_{2.1}^{\delta-}$ nanosheets show a distinguished semimetallic property, and $Cs_4W_{11}O_{36}^{2-}$ nanosheets are photochromic.[41,43] Thus, we have plenty of choices to design artificial heterostructure materials based on MoS_2 and oxide nanosheets, which can be expected to lead to exciting functions.

Table 1.2. Physical properties of oxide nanosheets.[21,22]

Material	Properties
$Ti_{1-\delta}O_2^{4\delta-}$, *e.g.,* $Ti_{0.91}O_2^{0.36-}$, $Ti_{0.87}O_2^{0.52-}$	Photocatalytic, Dielectric
Doped $Ti_{1-\delta}O_2^{4\delta-}$, *e.g.,* $Ti_{0.8}Co_{0.2}O_2^{0.4-}$, $Ti_{0.6}Fe_{0.4}O_2^{0.4-}$, $Ti_{(5.2-2\delta)/6}Mn_{\delta/2}O_2^{(3.2-\delta)/6-}$ $(0 \leq \delta \leq 0.4)$ $Ti_{0.8-\delta/4}Fe_{\delta/2}Co_{0.2-\delta/4}O_2^{0.4-}$ $(0 \leq \delta \leq 0.8)$	Ferromagnetic
$Ca_2Nb_3O_{10}^-$	Photocatalytic, Dielectric
TaO_3^-	Photocatalytic
$MnO_2^{\delta-}$	Redoxable
$Cs_4W_{11}O_{36}^{2-}$	Redoxable, Photochromic
$RuO_{2.1}^{\delta-}$	Conductive, Redoxable

Following the direction described above, we may consider titanium oxide nanosheets as a particular example. Wang and Sasaki recently reviewed titanium oxide nanosheets, elaborating various properties and potential applications in photoinduced (*e.g.,* photocatalytic, photovoltaic, and photoluminescence) and electrochemical applications, dielectric nanodevices, and biomedical applications.[24] Similar to those of bulk TiO_2, titanium oxide nanosheets possess semiconducting properties. However, the band gap of titanium oxide nanosheets is larger (3.8 eV)[140] than that of bulk TiO_2 (3.2 eV), due to the size quantization effect. Consequently, titanium oxide nanosheets exhibit a sharp absorption with the peak top at ~265 nm, which is significantly shifted to the blue region from the absorption edge of typical TiO_2 nanoparticles (Figure 1.8). This feature makes the absorption at the boundary between the visible light and near UV region negligible.

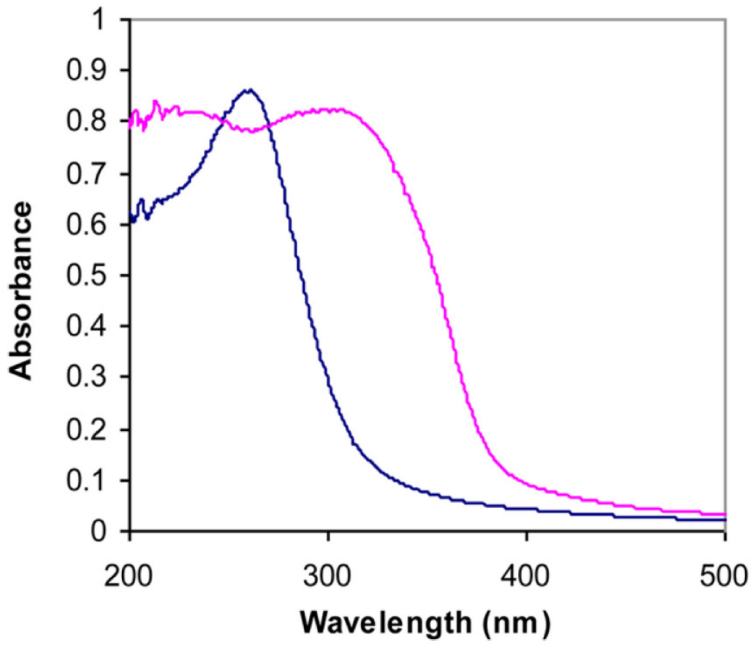

Figure 1.8. UV−vis absorption spectra of $Ti_{0.91}O_2^{0.36-}$ nanosheets and TiO_2 nanoparticles (anatase). Adapted with permission from Ref. 24. Copyright 2014 American Chemical Society.

The optical absorption of titanium oxide nanosheets below 300 nm is very strong, which is attributed to the unique 2D structure that enables the exposure of light to the majority atoms in the unilamellar sheets and minimizes the light scattering. Such a unique feature led to a >90% absorption of the incident light with only 20 layers of the titanium oxide nanosheets in a multilayer film (Figure 1.9a).[141] Titanium oxide nanosheets also exhibit a distinguished photocatalytic activity. For example, a monolayer film of titanium oxide nanosheets demonstrated drastic changes in its water contact angle under UV irradiation (Figure 1.9b), yielding a highly hydrophilic state.[142] Considering the strong optical absorption in the UV region and the excellent photocatalytic property of titanium oxide nanosheets, its hybridization with MoS_2 nanosheets may lead to an exciting opportunity to develop a new class of photocatalyst materials for the hydrogen evolution reaction. Proper design of the hetero-assembly of MoS_2 and titanium oxide nanosheets can be expected to

significantly enhance the photocatalytic activity and contribute to resolve the bottleneck restricting the practical applications of photocatalyst materials.

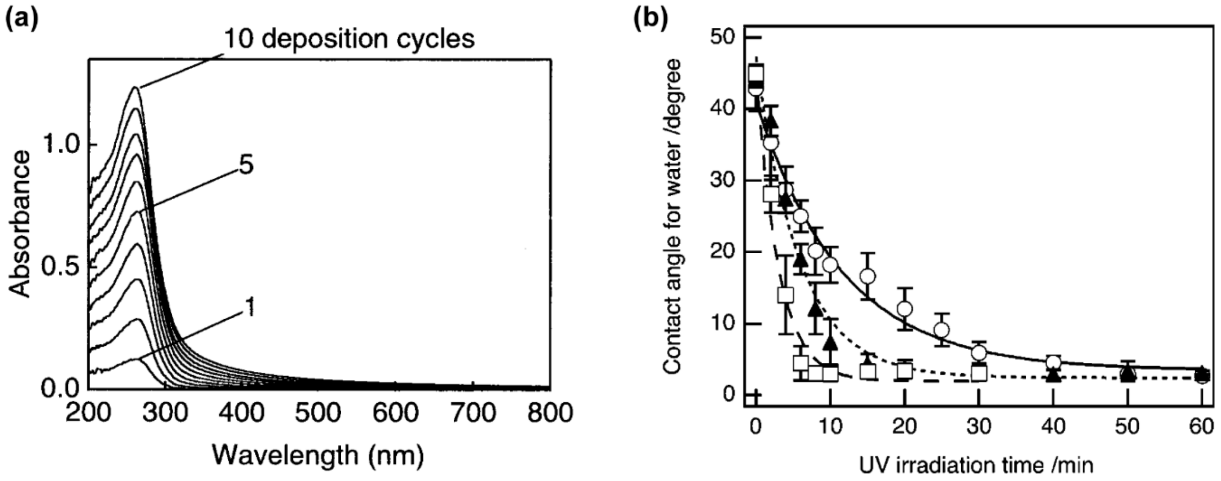

Figure 1.9. (a) The UV-visible absorption spectra of multilayer titanium oxide nanosheets. Adapted with permission from Ref. 141. Copyright 2001 American Chemical Society. (b) Photocatalytic activity of titanium oxide nanosheets as measured from contact angle (θ) changes of monolayer film surface of titanium oxide nanosheets under different intensities of UV light: circles, triangles, and squares are the data with light intensities of 19.8, 42.3, and 124 mW cm^{-2}, respectively. Adapted with permission from Ref. 142. Copyright 2006 American Chemical Society.

1.1.5. Preparation of MoS_2 Nanosheets

In general, the preparation of MoS_2 nanosheets can be classified into two groups, *i.e.,* top-down and bottom-up approaches. However, in this thesis, the author only focuses on the top-down approach. The top-down approach is divided into three categories, *i.e.,* mechanical cleavage, solvent-based exfoliation (sonication method), and chemical exfoliation methods.

Mechanical cleavage. Layered bulk-MoS_2 crystals can be readily delaminated through mechanical cleavage. This method is widely known as the "scotch tape method". This method is simple and straightforward. As illustrated in Figure 1.10, few-layered flakes can be obtained by mechanically peeling-off bulk 2D crystals using scotch tape or a similar adhesive tape.[143] Eventually, the peeled layered crystals are transferred to a substrate by applying pressure. The exfoliated sheets typically retain their high quality. Therefore, this method is ideal for the fundamental research study of intrinsic nanosheets. However, this method has limitations for practical applications due to its very low yield and low reproducibility of perfect monolayer nanosheets, and it remains difficult to control the number of layers. Therefore, an alternative must be considered for practical applications in large-scale production.

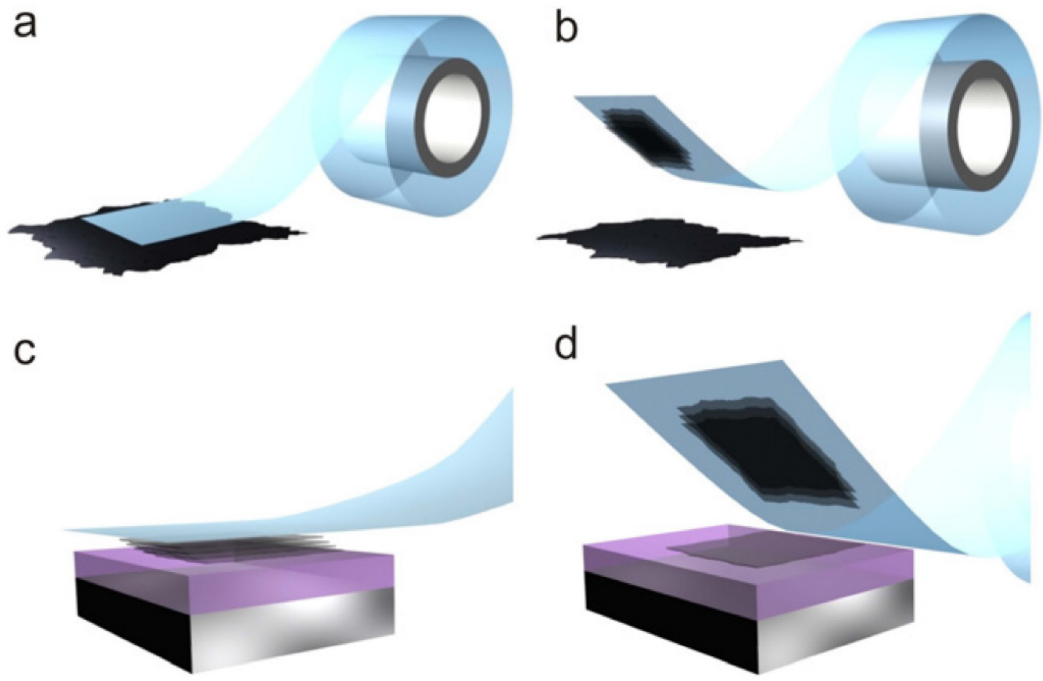

Figure 1.10. Schematic illustration of the mechanical cleavage method to exfoliate layered crystals. (a) Adhesive tape is pressed against a layered 2D crystal. (b) The top few layers of the crystal are adhered to the tape. (c) The tape with a few 2D-crystal layers is pressed against a substrate surface. (d) The bottom layers remain on the substrate upon peeling off. Reproduced with permission from Ref. 143. Copyright 2012 IOP Publishing.

Solvent-based exfoliation. This method applies sonication for the dispersion of layered crystals, typically in organic solvents.[144–148] This method can be considered as one of the most direct routes to exfoliate layered materials based on the solution process. This method was developed by Coleman's group for the exfoliation of layered graphite into graphene.[146,147] The choice of solvents plays a key role in achieving a high exfoliation yield. The solvent criterion that must be met is the matching of surface tension between the layered crystals and the liquid medium, to reduce the energetic cost during the sonication process. In addition, this guarantees the formation of a stable dispersion of nanosheets and prevents nanosheet restacking and aggregation. In 2011, Coleman's group reported the exfoliation of MoS_2 crystals into single- to few-layer MoS_2 nanosheets in organic solvents under ultrasonication.[145] The experimental results suggested that the solvent should achieve a surface tension of ~40 mJ m^{-2}. Among various organic solvents that they used, 1-methyl-2-pyrrolidone (MNP) was identified as the most effective. Although this method provides a high yield as compared to mechanical cleavage, the yield of monolayer nanosheets is still relatively low. In addition, the size of the nanosheets is very small in the range of tens to few hundreds of nanometers, due to the strong energy employed in the ultrasonication. Consequently, this method is still far from practical applications.

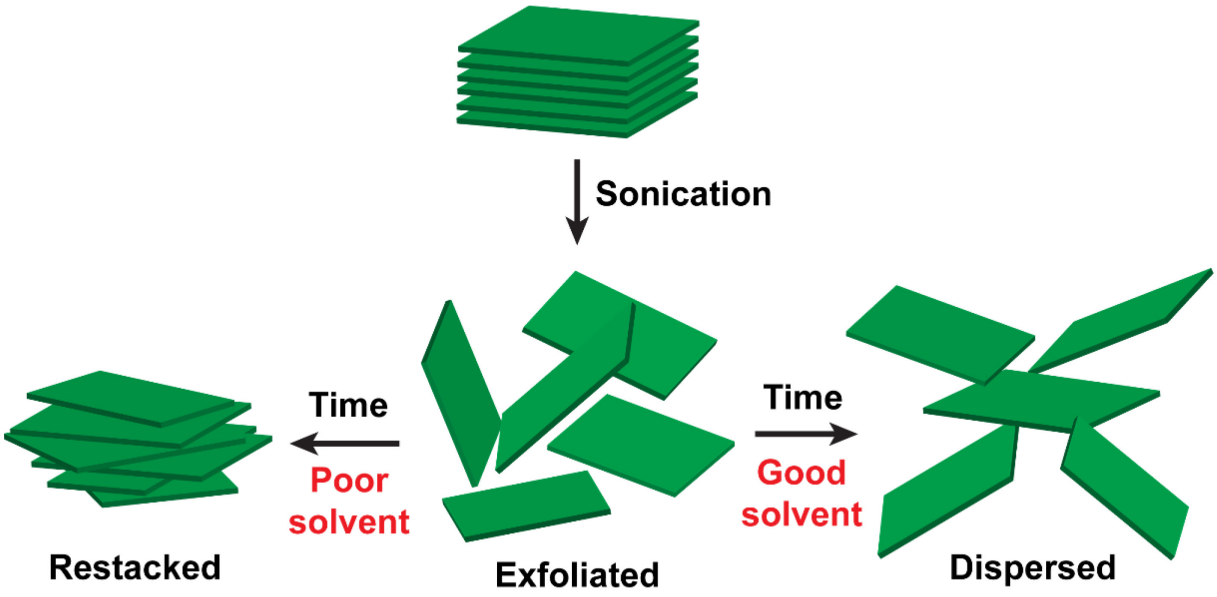

Figure 1.11. Schematic diagram for solvent-based exfoliation.[144]

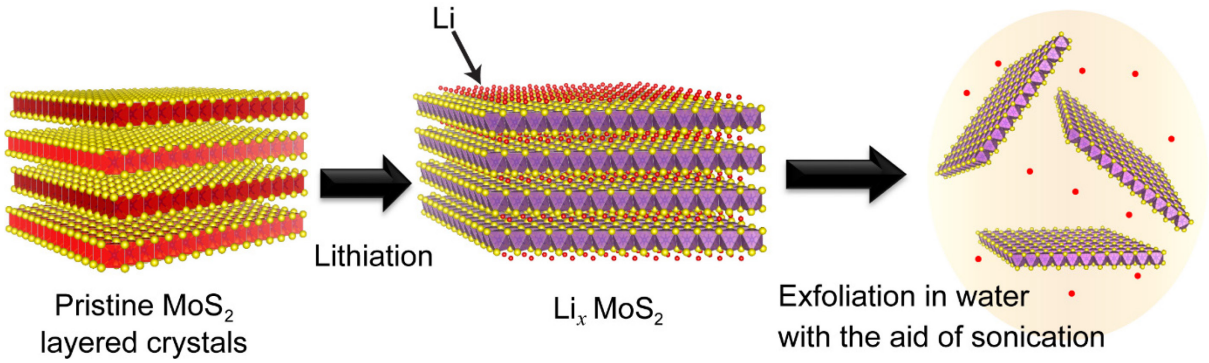

Figure 1.12. Schematic diagram for the chemical exfoliation of MoS_2 nanosheets.

Chemical exfoliation. To overcome the limitations of mechanical cleavage and solvent-based sonication methods, chemical exfoliation can be considered a solution (Figure 1.12). In principle, chemical exfoliation applies a reductive intercalation process of alkali metals into MoS_2 layers, since the MoS_2 layers are neutral. Interestingly, this process has been extensively studied since the 1970's by intercalating MoS_2 crystals with lithium.[100,149–152] Even, monolayer MoS_2 nanosheets were successfully delaminated from Li-intercalated MoS_2 by Joensen *et al*. in 1986.[153] The Li intercalation into pristine MoS_2 layered crystals can be achieved by reacting with *n*-lithium in hexane, to yield lithiated MoS_2 crystals (Li_xMoS_2). The Li_xMoS_2 is readily delaminated in water with the aid of sonication. In this process, the Li_xMoS_2 crystals react with water and generate hydrogen gas.[154] Since the MoS_2 layers are weakly bound together by van der Waals forces, the resulting hydrogen gas easily separates the layers, yielding monolayer MoS_2 nanosheets

dispersed in water. Through this process, more than 70% of well-dispersed unilamellar MoS_2 nanosheets can be produced.

Chemical exfoliation is a facile method to prepare monolayer MoS_2 nanosheets in a large quantity, which is of advantageous for practical applications in large-scale production processes. However, it is should be noted that the Li intercalation of MoS_2 leads to the structural transformation from the hexagonal 2H phase to the octahedral 1T.[68,154–157] The restoration of the 2H phase of the exfoliated nanosheets can be achieved by applying a heating process.[154,158] Thus, this method may offer a high versatility in obtaining end products.

1.1.6. An Issue on Chemically Exfoliated MoS_2

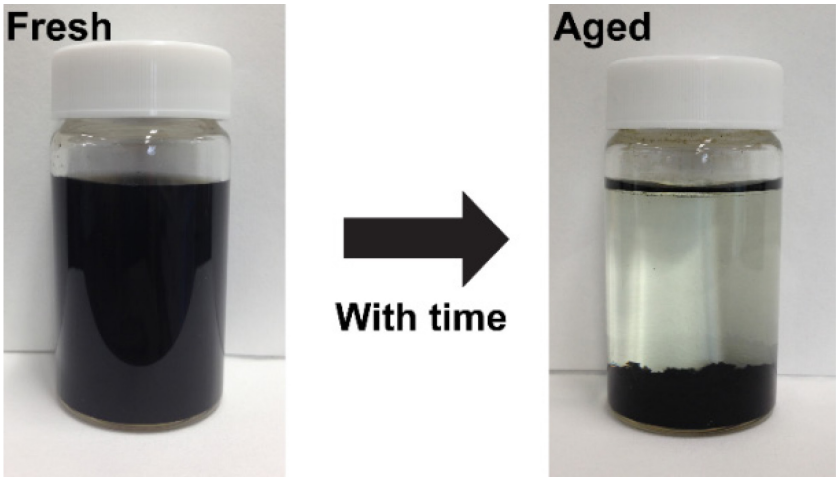

Figure 1.13. Aggregation of chemically exfoliated MoS_2 nanosheets is typically observed with aging in ambient air (in this figure, it was after 4 months of aging process).

Although the chemical exfoliation of MoS_2 has been demonstrated as a facile and versatile method to prepare monolayer MoS_2 nanosheets in a large quantity, it possesses a long standing drawback that can limit the utilization of the exfoliated nanosheets. It seems that the drawback has been overlooked for more than 30 years. It is found that the resultant colloidal suspension of the exfoliated nanosheets is unstable and tends to aggregate with aging in ambient air (Figure 1.13). Such aggregation definitely impedes the applicability of the exfoliated nanosheets and degrades their performance. Figure 1.14 displays the XRD patterns of an as-collected aggregate of MoS_2 nanosheets and that after annealing, as the reference. The annealed sample can be considered as 2H MoS_2.[154,158] Nearly no change was observed except at the in-plane diffractions of the MoS_2 nanosheets ($2\theta \cong 33$ and 58°), which may suggest that the aggregated MoS_2 contained the 1T phase. However, this information is not enough to derive a conclusion on the nature of chemically exfoliated MoS_2. Therefore, an in-depth study in this regard is of critical importance to reveal their intrinsic characteristics and behaviors.

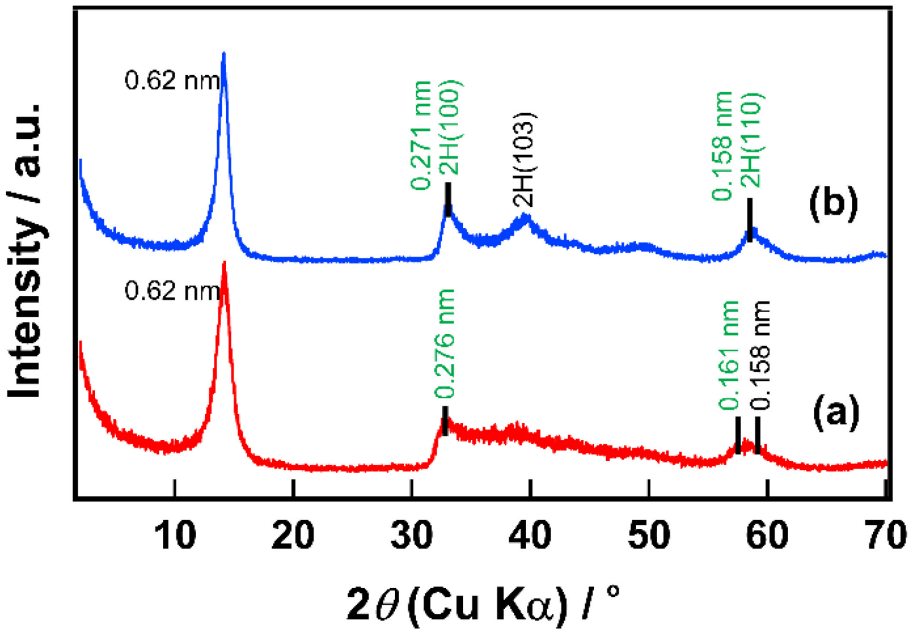

Figure 1.14. XRD patterns of (a) as-collected aggregates of MoS_2 nanosheets after aging of the suspension in ambient air for 4 months and (b) after annealing at 300 °C in an Ar atmosphere. The pattern of sample (b) can be indexed based on the 1 × 1 of the 2D hexagonal structure of 2H-MoS_2.[154]

1.2. Objectives

In light of the above discussion, this thesis work was designed to systematically investigate the nature and behavior of chemically exfoliated MoS_2. The stability and nature of the nanosheets were examined in terms of their suspension stability, morphology, chemical and electronic nature, and phase and 2D structure. This study is of critical importance to provide a deeper understanding of the chemical nature and 2D structure of chemically exfoliated MoS_2 as well as to identify and elaborate the factors influencing the stability and quality of the nanosheets in an aqueous suspension. This work provides guidance to designing a direct strategy for the controllable preparation of high-quality and stable of MoS_2 nanosheets.

In the second step, a new class of photocatalyst materials was designed from the hetero-assembly of $Ti_{1-\delta}O_2^{4\delta-}$ and MoS_2 nanosheets, where the $Ti_{1-\delta}O_2^{4\delta-}$ and MoS_2 act as the photoactive material and co-catalyst, respectively. In general, co-catalysts are impregnated on particle-based photocatalysts as a thick and dense body. This approach reduces the penetration of light into the photocatalysts. In addition, the particle-based heterointerfaces usually fail to achieve sufficient interfacial contact at a molecular level, hindering the migration of photogenerated electrons from the photocatalyst to the co-catalyst surface. Therefore, the utilization of 2D nanomaterials, both for the photocatalyst and co-catalyst, can be a promising strategy to overcome this issue by taking advantage of their high ability to tailoring desired nanostructures, where 2D nanomaterials can readily achieve “face-to-face” interfacial contact.

1.3. Thesis Organization

The thesis work includes four chapters.

Chapter 1 describes the research background and motivation of this study. It starts with the introduction of two-dimensional nanomaterials with a particular emphasis on MoS_2 nanosheets as one of important classes of 2D nanomaterials. This is followed by research advances in 2D nanomaterials focusing on the hetero-assembly of two types of nanosheets, then the utilization of MoS_2 as a building block to construct unique artificial structures with other nanosheets as well as its prospect with oxide-based nanosheets, and the potential of discovering unprecedented functions. However, the MoS_2 nanosheets, prepared *via* chemical exfoliation procedure, conceal a long standing drawback that can hamper the utilization of the exfoliated nanosheets. This issue drives the motivation to study in-depth the nature of chemically exfoliated MoS_2. With a view on the previous study, the objectives are proposed.

Chapter 2 is devoted to the study of the nature of chemically exfoliated MoS_2 nanosheets in an aqueous suspension. The study is focused on the stability and quality, the electronic nature, and the structure of the exfoliated nanosheets. It is confirmed that the stability and nature of the exfoliated nanosheets are strongly associated with the reoxidation process. Suppressing the reoxidation process is a key to preserving the quality of the exfoliated nanosheets.

Chapter 3 addresses the design and fabrication of the two-dimensional heterointerface structure of restacked-$Ti_{0.87}O_2^{0.52-}$/1T-Phase MoS_2 and its application in photocatalysis for hydrogen generation. Such a unique structure is attained from the monolayer modification of restacked $Ti_{0.87}O_2^{0.52-}$ nanosheets with 1T-phase MoS_2. Thus, this structure is beneficial for photocatalytic applications due to the largely exposed MoS_2 surface as the electron collector and the catalytically active site. As a result, the designed structure shows a highly efficient photocatalytic activity for hydrogen generation.

Finally, Chapter 4 summarizes the works reported in this thesis and describes the future prospects.

1.4. Experimental Conditions for Sample Characterization

The following are the experimental conditions.

1.4.1. Powder X-ray Diffraction

The structure and phase purity of the samples were examined using powder X-ray diffraction (XRD) analysis with a Rigaku Rint ULTIMA IV diffractometer. The measurement parameters were as follows:

Wavelength: graphite monocromatized Cu Kα radiation (λ = 0.15405 nm)
Voltage: 40 kV
Current: 40 mA

Scan speed: 1 deg/min
Sampling width: 0.020 deg

1.4.2. In-plane X-ray Diffraction

In-plane XRD measurements for the structural determination of nanosheets were carried out using synchrotron X-ray radiation at room temperature at the Photon Factory BL-6C of the High-energy Accelerator Research Organization (KEK-PF), Institute of Materials Structure Science. The X-ray beam (λ = 0.12007 nm) was irradiated at a constant incident angle of 14°. The X-ray diffraction patterns were recorded in the 2θ-range of 15-70°

1.4.3. Atomic Force Microscopy

The morphology, lateral size, and thickness of the nanosheets were examined using a Hitachi SPA 400 atomic force microscope (AFM) in tapping mode using a Si-tip cantilever (a force constant of ~20 N m^{-1}). The typical scan area was $(2\text{-}5)^2$ μm^2.

1.4.4. Electron Microscopy

The morphology of bulk samples was examined with a JEOL JSM-6010LA scanning electron microscope (SEM) at an acceleration voltage of 10 kV. The specimens were coated with Pt to minimize the charging effect. Transmission electron microscope (TEM) images and selected area electron diffraction (SAED) patterns of the samples were obtained using a JEOL JEM-3000F at an acceleration voltage of 200 kV. An aliquot of the sample suspension was pipetted and dispersed in ethanol under mild sonication for 5 min. A few drops of the dispersion was placed onto the TEM grid and dried for observation.

1.4.5. X-ray Photoelectron Spectroscopy

The chemical and electronic nature of the samples were examined with a Thermo Scientific Theta Probe Thermo Electron (Al Kα radiation). The spectra were calibrated relative to the C1s binding energy at 284.8 eV. The measurements were performed within 2 days from the specimen preparation to minimize the aging effect.

1.4.6. Elemental Analysis

The elemental analysis of the exfoliated MoS_2 samples was carried out by ICP-OES using a Hitachi High-tech SPS3520UV-DD. The samples were dissolved in a mixture of sodium hydroxide and bromine solution. The subsequent addition of nitric acid under continuous heating was applied to remove the bromine. Then, the solution was diluted with water before the measurement.

1.4.7. UV-visible Absorption Spectroscopy

The UV-visible absorption spectra of the sample suspensions were recorded using a Hitachi U-4100 spectrophotometer. The absorption spectra were measured in a wavelength a range of 200-800 nm.

1.4.8. UV-visible Diffuse Reflectance Spectroscopy

The UV-visible Diffuse Reflectance Spectra of powder samples were recorded using a Shimadzu SolidSpec-3700 DUV, equipped with an integrating sphere. The diffuse reflectance spectra were measured in a wavelength range of 200-800 nm.

1.4.9. Absorption/Desorption Isotherms and BET Surface Area

A Quantachrome Autosorb-1 was used to record the adsorption/desorption isotherm data using N_2. Prior to each measurement, a sample was outgassed under vacuum conditions for 2 h at 150 °C to remove adsorbed water vapor. The Brunauer–Emmett–Teller (BET) surface area of the samples was calculated from a relative pressure range of $0.05 < P/P_0 < 0.3$.

1.4.10. Zeta Potential

The zeta potential values of the sample suspensions were measured using an ELS-Z zeta potential analyzer.

1.5. Chemicals

The following chemicals were used in the study:

Bulk molybdenum disulfide; MoS_2 (Furuuchi Kagaku, Japan)
Lithium hydroxide; $LiOH{\cdot}H_2O$ (Wako Chemicals, 98%)
n-butyllithium in *n*-hexane (1.6 M); $CH_3(CH_2)_3Li$ (Wako Chemicals, 14.5-17.0%)
Super dehydrated *n*-hexane; (Wako Chemicals, 96%)
Lithium carbonate; Li_2CO_3 (Rare Metallic, 99.99%)
Potassium carbonate; K_2CO_3 (Rare Metallic, 99.99%)
Titanium dioxide; TiO_2 (Rare Metallic, 99.99%)
Tetrabutylammonium hydroxide; $(CH_3(CH_2)_3)_4NOH$ (Wako Chemicals, 10.0-11.0%)
Ethanol; C_2H_5OH ((Wako Chemicals, 99.5%)
Milli-Q filtered water

1.6. References

[1] G. A. Ozin, A. Arsenault, L. Cademartiri, *Nanochemistry: A Chemical Approach to Nanomaterials*, The Royal Society Of Chemistry, **2008**.

[2] R. Mas-Ballesté, C. Gómez-Navarro, J. Gómez-Herrero, F. Zamora, *Nanoscale* **2011**, *3*, 20–30.

[3] S. Eustis, M. A. El-Sayed, *Chem. Soc. Rev.* **2006**, *35*, 209–217.

[4] P. K. Jain, X. Huang, I. H. El-Sayed, M. A. El-Sayed, *Plasmonics* **2007**, *2*, 107–118.

[5] J. A. Scholl, A. L. Koh, J. A. Dionne, *Nature* **2012**, *483*, 421–427.

[6] W. L. Wilson, P. F. Szajowski, L. E. Brus, *Science* **1993**, *262*, 1242–1244.

[7] E. G. Barbagiovanni, D. J. Lockwood, P. J. Simpson, L. V. Goncharova, *Appl. Phys. Rev.* **2014**, *1*, 11302.

[8] Y. Gu, I. L. Kuskovsky, M. Yin, S. O'Brien, G. F. Neumark, *Appl. Phys. Lett.* **2004**, *85*, 3833–3835.

[9] Y. M. Niquet, G. Allan, C. Delerue, M. Lannoo, *Appl. Phys. Lett.* **2000**, *77*, 1182–1184.

[10] M. A. G. Soler, L. G. Paterno, in *Nanostructures*, Elsevier, **2017**, pp. 147–186.

[11] F. Wiekhorst, E. Shevchenko, H. Weller, J. Kötzler, *Phys. Rev. B* **2003**, *67*, 224416.

[12] S. R. Shinde, S. B. Ogale, J. S. Higgins, H. Zheng, A. J. Millis, V. N. Kulkarni, R. Ramesh, R. L. Greene, T. Venkatesan, *Phys. Rev. Lett.* **2004**, *92*, 166601.

[13] K. Ueno, S. Nakamura, H. Shimotani, H. T. Yuan, N. Kimura, T. Nojima, H. Aoki, Y. Iwasa, M. Kawasaki, *Nat. Nanotechnol.* **2011**, *6*, 408–412.

[14] K. S. Novoselov, A. K. Geim, S. V. Morozov, D. Jiang, Y. Zhang, S. V. Dubonos, I. V. Grigorieva, A. A. Firsov, *Science* **2004**, *306*, 666–669.

[15] K. S. Novoselov, V. I. Fal'Ko, L. Colombo, P. R. Gellert, M. G. Schwab, K. Kim, *Nature* **2012**, *490*, 192–200.

[16] X. Huang, X. Qi, F. Boey, H. Zhang, *Chem. Soc. Rev.* **2012**, *41*, 666–686.

[17] K. S. Novoselov, D. Jiang, F. Schedin, T. J. Booth, V. V Khotkevich, S. V Morozov, A. K. Geim, *Proc. Natl. Acad. Sci.* **2005**, *102*, 10451–10453.

[18] A. K. Geim, I. V Grigorieva, *Nature* **2013**, *499*, 419–425.

[19] S. Z. Butler, S. M. Hollen, L. Cao, Y. Cui, J. a. Gupta, H. R. Gutiérrez, T. F. Heinz, S. S. Hong, J. Huang, A. F. Ismach, et al., *ACS Nano* **2013**, *7*, 2898–2926.

[20] M. Xu, T. Liang, M. Shi, H. Chen, *Chem. Rev.* **2013**, *113*, 3766–3798.

[21] R. Ma, T. Sasaki, *Adv. Mater.* **2010**, *22*, 5082–5104.

[22] M. Osada, T. Sasaki, *J. Mater. Chem.* **2009**, *19*, 2503–2511.

[23] M. Osada, T. Sasaki, *Adv. Mater.* **2012**, *24*, 210–228.

[24] L. Wang, T. Sasaki, *Chem. Rev.* **2014**, *114*, 9455–9486.

[25] T. Sasaki, M. Watanabe, H. Hashizume, H. Yamada, H. Nakazawa, *J. Am. Chem. Soc.* **1996**, *118*, 8329–8335.

[26] T. Sasaki, M. Watanabe, *J. Am. Chem. Soc.* **1998**, *120*, 4682–4689.

[27] M. M. J. Treacy, S. B. Rice, A. J. Jacobson, J. T. Lewandowski, *Chem. Mater.* **1990**, *2*, 279–286.

[28] M. Fang, C. H. Kim, G. B. Saupe, H.-N. Kim, C. C. Waraksa, T. Miwa, A. Fujishima, T. E. Mallouk, *Chem. Mater.* **1999**, *11*, 1526–1532.

[29] Y. Ebina, T. Sasaki, M. Watanabe, *Solid State Ionics* **2002**, *151*, 177–182.

[30] Y. Song, N. Iyi, T. Hoshide, T. C. Ozawa, Y. Ebina, R. Ma, N. Miyamoto, T. Sasaki, *Chem. Commun.* **2015**, *51*, 17068–17071.

[31] D. S. Kim, T. C. Ozawa, K. Fukuda, S. Ohshima, I. Nakai, T. Sasaki, *Chem. Mater.* **2011**, *23*, 2700–2702.

[32] Z. Liu, K. Ooi, H. Kanoh, W. Tang, T. Tomida, *Langmuir* **2000**, *16*, 4154–4164.

[33] Y. Omomo, T. Sasaki, L. Z. Wang, M. Watanabe, *J. Am. Chem. Soc.* **2003**, *125*, 3568–3575.

[34] Z. Liu, R. Ma, Y. Ebina, K. Takada, T. Sasaki, *Chem. Mater.* **2007**, *19*, 6504–6512.

[35] G. B. Saupe, C. C. Waraksa, H.-N. Kim, Y. J. Han, D. M. Kaschak, D. M. Skinner, T. E. Mallouk, *Chem. Mater.* **2000**, *12*, 1556–1562.

[36] K. Fukuda, I. Nakai, Y. Ebina, R. Ma, T. Sasaki, *Inorg. Chem.* **2007**, *46*, 4787–4789.

[37] H. Rebbah, M. M. Borel, B. Raveau, *Mater. Res. Bull.* **1980**, *15*, 317–321.

[38] H. Rebbah, J. Pannetier, B. Raveau, *J. Solid State Chem.* **1982**, *41*, 57–62.

[39] M. Fang, C. H. Kim, T. E. Mallouk, *Chem. Mater.* **1999**, *11*, 1519–1525.

[40] A. Takagaki, M. Sugisawa, D. Lu, J. N. Kondo, M. Hara, K. Domen, S. Hayashi, *J. Am. Chem. Soc.* **2003**, *125*, 5479–5485.

[41] K. Fukuda, K. Akatsuka, Y. Ebina, R. Ma, K. Takada, I. Nakai, T. Sasaki, *ACS Nano* **2008**, *2*, 1689–1695.

[42] N. Sakai, Y. Ebina, K. Takada, T. Sasaki, *J. Phys. Chem. B* **2005**, *109*, 9651–9655.

[43] K. Fukuda, K. Akatsuka, Y. Ebina, M. Osada, W. Sugimoto, M. Kimura, T. Sasaki, *Inorg. Chem.* **2012**, *51*, 1540–1543.

[44] P. Xiong, R. Ma, N. Sakai, X. Bai, S. Li, T. Sasaki, *ACS Appl. Mater. Interfaces* **2017**, *9*, 6282–6291.

[45] P. Xiong, R. Ma, N. Sakai, T. Sasaki, *ACS Nano* **2018**, *12*, 1768–1777.

[46] M. Osada, Y. Ebina, K. Fukuda, K. Ono, K. Takada, K. Yamaura, E. Takayama-Muromachi, T. Sasaki, *Phys. Rev. B* **2006**, *73*, 2–5.

[47] M. Osada, M. Itose, Y. Ebina, K. Ono, S. Ueda, K. Kobayashi, T. Sasaki, *Appl. Phys. Lett.* **2008**, *92*, 2006–2009.

[48] M. Osada, S. Yoguchi, M. Itose, B.-W. Li, Y. Ebina, K. Fukuda, Y. Kotani, K. Ono, S. Ueda, T. Sasaki, *Nanoscale* **2014**, *6*, 14227–14236.

[49] R. Ma, Z. Liu, L. Li, N. Iyi, T. Sasaki, *J. Mater. Chem.* **2006**, *16*, 3809.

[50] F. Geng, R. Ma, T. Sasaki, *Acc. Chem. Res.* **2010**, *43*, 1177–1185.

[51] Q. Wang, D. O'Hare, *Chem. Rev.* **2012**, *112*, 4124–4155.

[52] S. Nakagaki, M. Halma, A. Bail, G. G. C. Arízaga, F. Wypych, *J. Colloid Interface Sci.* **2005**, *281*, 417–423.

[53] S. Liu, X. Jiang, G. Zhuo, *J. Mol. Catal. A Chem.* **2008**, *290*, 72–78.

[54] J. Wang, L. Zhao, H. Shi, J. He, *Angew. Chem. Int. Ed.* **2011**, *50*, 9171–9176.

[55] Y. Wang, W. Yang, J. Yang, *Electrochem. Solid-State Lett.* **2007**, *10*, A233.

[56] N. Ohta, K. Takada, L. Zhang, R. Ma, M. Osada, T. Sasaki, *Adv. Mater.* **2006**, *18*, 2226–2229.

[57] M. A. Woo, M.-S. Song, T. W. Kim, I. Y. Kim, J.-Y. Ju, Y. S. Lee, S. J. Kim, J.-H. Choy, S.-J. Hwang, *J. Mater. Chem.* **2011**, *21*, 4286.

[58] X. Liu, R. Ma, Y. Bando, T. Sasaki, *Adv. Mater.* **2012**, *24*, 2148–2153.

[59] F. Geng, H. Xin, Y. Matsushita, R. Ma, M. Tanaka, F. Izumi, N. Iyi, T. Sasaki, *Chem. A Eur. J.* **2008**, *14*, 9255–9260.

[60] F. Geng, Y. Matsushita, R. Ma, H. Xin, M. Tanaka, F. Izumi, N. Iyi, T. Sasaki, *J. Am. Chem. Soc.* **2008**, *130*, 16344–16350.

[61] F. Geng, Y. Matsushita, M. Renzhi, H. Xin, M. Tanaka, N. Lyi, T. Sasaki, *Inorg. Chem.* **2009**, *48*, 6724–6730.

[62] L. J. McIntyre, L. K. Jackson, A. M. Fogg, *J. Phys. Chem. Solids* **2008**, *69*, 1070–1074.

[63] L. Poudret, T. J. Prior, L. J. McIntyre, A. M. Fogg, *Chem. Mater.* **2008**, *20*, 7447–7453.

[64] S. A. Hindocha, L. J. McIntyre, A. M. Fogg, *J. Solid State Chem.* **2009**, *182*, 1070–1074.

[65] R. Ma, X. Liu, J. Liang, Y. Bando, T. Sasaki, *Adv. Mater.* **2014**, *26*, 4173–4178.

[66] W. Ma, R. Ma, C. Wang, J. Liang, X. Liu, K. Zhou, T. Sasaki, *ACS Nano* **2015**, *9*, 1977–1984.

[67] Q. H. Wang, K. Kalantar-Zadeh, A. Kis, J. N. Coleman, M. S. Strano, *Nat. Nanotechnol.* **2012**, *7*, 699–712.

[68] M. Chhowalla, H. S. Shin, G. Eda, L.-J. Li, K. P. Loh, H. Zhang, *Nat. Chem.* **2013**, *5*, 263–75.

[69] X. Huang, Z. Zeng, H. Zhang, *Chem. Soc. Rev.* **2013**, *42*, 1934–46.

[70] R. Lv, J. a Robinson, R. E. Schaak, D. Sun, Y. Sun, T. E. Mallouk, M. Terrones, *Acc. Chem. Res.* **2015**, *48*, 56–64.

[71] H. Li, J. Wu, Z. Yin, H. Zhang, *Acc. Chem. Res.* **2014**, *47*, 1067–75.

[72] R. F. Sebenik, A. R. Burkin, R. R. Dorfler, J. M. Laferty, G. Leichtfried, H. Meyer-Grünow, P. C. H. Mitchell, M. S. Vukasovich, D. A. Church, G. G. Van Riper, et al., in *Ullmann's Encycl. Ind. Chem.*, **2000**.

[73] R. Ganatra, Q. Zhang, *ACS Nano* **2014**, *8*, 4074–4099.

[74] E. Lhuillier, S. Pedetti, S. Ithurria, B. Nadal, H. Heuclin, B. Dubertret, *Acc. Chem. Res.* **2015**, *48*, 22–30.

[75] T. Le Mogne, C. Donnet, J. M. Martin, A. Tonck, N. Millard-Pinard, S. Fayeulle, N. Moncoffre, *J. Vac. Sci. Technol. A Vacuum, Surfaces, Film.* **1994**, *12*, 1998–2004.

[76] W. Hai-dou, X. Bin-shi, L. Jia-jun, Z. Da-ming, *Sci. Technol. Adv. Mater.* **2005**, *6*, 535–539.

[77] M. H. Cho, J. Ju, S. J. Kim, H. Jang, *Wear* **2006**, *260*, 855–860.

[78] E. Fortin, W. M. Sears, *J. Phys. Chem. Solids* **1982**, *43*, 881–884.

[79] E. Gourmelon, O. Lignier, H. Hadouda, G. Couturier, J. C. Bernède, J. Tedd, J. Pouzet, J. Salardenne, *Sol. Energy Mater. Sol. Cells* **1997**, *46*, 115–121.

[80] L. Gomez De Arco, Y. Zhang, C. W. Schlenker, K. Ryu, M. E. Thompson, C. Zhou, *ACS Nano* **2010**, *4*, 2865–2873.

[81] P. Raybaud, J. Hafner, G. Kresse, S. Kasztelan, H. Toulhoat, *J. Catal.* **2000**, *189*, 129–146.

[82] H. Schweiger, P. Raybaud, G. Kresse, H. Toulhoat, *J. Catal.* **2002**, *207*, 76–87.

[83] G. Chatzitheodorou, S. Fiechter, M. Kunst, J. Luck, H. Tributsch, *Mater. Res. Bull.* **1988**, *23*, 1261–1271.

[84] D. Lembke, S. Bertolazzi, A. Kis, *Acc. Chem. Res.* **2015**, *48*, 100–110.

[85] Y. P. V Subbaiah, K. J. Saji, A. Tiwari, *Adv. Funct. Mater.* **2016**, *26*, 2046–2069.

[86] Y. Yoon, K. Ganapathi, S. Salahuddin, *Nano Lett.* **2011**, *11*, 3768–73.

[87] K. F. Mak, C. Lee, J. Hone, J. Shan, T. F. Heinz, *Phys. Rev. Lett.* **2010**, *105*, 136805.

[88] B. Radisavljevic, A. Radenovic, J. Brivio, V. Giacometti, A. Kis, *Nat. Nanotechnol.* **2011**, *6*, 147–150.

[89] T. Stephenson, Z. Li, B. Olsen, D. Mitlin, *Energy Environ. Sci.* **2014**, *7*, 209–231.

[90] T. Wang, S. Chen, H. Pang, H. Xue, Y. Yu, *Adv. Sci.* **2017**, *4*, 1600289.

[91] Q. Lu, Y. Yu, Q. Ma, B. Chen, H. Zhang, *Adv. Mater.* **2016**, *28*, 1917–1933.

[92] D. Voiry, J. Yang, M. Chhowalla, *Adv. Mater.* **2016**, *28*, 6197–6206.

[93] F. E. Wickman, D. K. Smith, *Am. Mineral.* **1970**, *55*, 1843–1856.

[94] R. G. Dickinson, L. Pauling, *J. Am. Chem. Soc.* **1923**, *45*, 1466–1471.

[95] F. Jellinek, G. Brauer, H. Müller, *Nature* **1960**, *185*, 376–377.

[96] F. Wypych, R. Schöllhorn, *J. Chem. Soc., Chem. Commun.* **1992**, 1386–1388.

[97] F. Wypych, K. Sollmann, R. Schöllhorn, *Mater. Res. Bull.* **1992**, *27*, 545–553.

[98] K. K. Kam, B. A. Parkinson, *J. Phys. Chem.* **1982**, *86*, 463–467.

[99] A. Splendiani, L. Sun, Y. Zhang, T. Li, J. Kim, C.-Y. Chim, G. Galli, F. Wang, *Nano Lett.* **2010**, *10*, 1271–1275.

[100] P. J. Mulhern, *Can. J. Phys.* **1989**, *67*, 1049–1052.

[101] E. Benavente, M. A. S. Ana, F. Mendizabal, G. Gonzalez, *Coord. Chem. Rev.* **2002**, *224*, 87–109.

[102] I. Song, C. Park, H. C. Choi, *RSC Adv.* **2015**, *5*, 7495–7514.

[103] J. Xiao, D. Choi, L. Cosimbescu, P. Koech, J. Liu, J. P. Lemmon, *Chem. Mater.* **2010**, *22*, 4522–4524.

[104] M. Acerce, D. Voiry, M. Chhowalla, *Nat. Nanotechnol.* **2015**, *10*, 313–318.

[105] L. Wang, Y. Ma, M. Yang, Y. Qi, *Electrochim. Acta* **2015**, *186*, 391–396.

[106] N. Savjani, E. A. Lewis, M. A. Bissett, J. R. Brent, R. A. W. Dryfe, S. J. Haigh, P. O'Brien, *Chem. Mater.* **2016**, *28*, 657–664.

[107] H. Hwang, H. Kim, J. Cho, *Nano Lett.* **2011**, *11*, 4826–4830.

[108] D. Voiry, M. Salehi, R. Silva, T. Fujita, M. Chen, T. Asefa, V. B. Shenoy, G. Eda, M. Chhowalla, *Nano Lett.* **2013**, *13*, 6222–6227.

[109] M. A. Lukowski, A. S. Daniel, F. Meng, A. Forticaux, L. Li, S. Jin, *J. Am. Chem. Soc.* **2013**, *135*, 10274–10277.

[110] J. L. Gunjakar, I. Y. Kim, J. M. Lee, Y. K. Jo, S.-J. Hwang, *J. Phys. Chem. C* **2014**, *118*, 3847–3863.

[111] H. Zhang, *ACS Nano* **2015**, *9*, 9451–9469.

[112] C. Tan, X. Cao, X.-J. Wu, Q. He, J. Yang, X. Zhang, J. Chen, W. Zhao, S. Han, G.-H. Nam, et al., *Chem. Rev.* **2017**, *117*, 6225–6331.

[113] R. Ma, T. Sasaki, *Acc. Chem. Res.* **2015**, *48*, 136–143.
[114] D. Jena, K. Banerjee, G. H. Xing, *Nat. Mater.* **2014**, *13*, 1076–1078.
[115] I. Y. Kim, Y. K. Jo, J. M. Lee, L. Wang, S.-J. Hwang, *J. Phys. Chem. Lett.* **2014**, *5*, 4149–4161.
[116] H. Wang, F. Liu, W. Fu, Z. Fang, W. Zhou, Z. Liu, *Nanoscale* **2014**, *6*, 12250–12272.
[117] R. Ma, T. Sasaki, *Annu. Rev. Mater. Res.* **2015**, *45*, 111–127.
[118] B. V. Lotsch, *Annu. Rev. Mater. Res.* **2015**, *45*, 85–109.
[119] K. S. Novoselov, A. Mishchenko, A. Carvalho, A. H. Castro Neto, *Science* **2016**, *353*, aac9439.
[120] C. R. Dean, L. Wang, P. Maher, C. Forsythe, F. Ghahari, Y. Gao, J. Katoch, M. Ishigami, P. Moon, M. Koshino, et al., *Nature* **2013**, *497*, 598–602.
[121] B. Hunt, J. D. Sanchez-Yamagishi, A. F. Young, M. Yankowitz, B. J. LeRoy, K. Watanabe, T. Taniguchi, P. Moon, M. Koshino, P. Jarillo-Herrero, et al., *Science* **2013**, *340*, 1427–1430.
[122] E. Coronado, C. Martí-Gastaldo, E. Navarro-Moratalla, A. Ribera, S. J. Blundell, P. J. Baker, *Nat. Chem.* **2010**, *2*, 1031–1036.
[123] M. Osada, Y. Ebina, K. Takada, T. Sasaki, *Adv. Mater.* **2006**, *18*, 295–299.
[124] B.-W. Li, M. Osada, T. C. Ozawa, Y. Ebina, K. Akatsuka, R. Ma, H. Funakubo, T. Sasaki, *ACS Nano* **2010**, *4*, 6673–6680.
[125] N. Sakai, K. Fukuda, Y. Omomo, Y. Ebina, K. Takada, T. Sasaki, *J. Phys. Chem. C* **2008**, *112*, 5197–5202.
[126] X. Cai, N. Sakai, T. C. Ozawa, A. Funatsu, R. Ma, Y. Ebina, T. Sasaki, *ACS Appl. Mater. Interfaces* **2015**, *7*, 11436–11443.
[127] B.-W. Li, M. Osada, Y. Ebina, S. Ueda, T. Sasaki, *J. Am. Chem. Soc.* **2016**, *138*, 7621–7625.
[128] W. J. Yu, Z. Li, H. Zhou, Y. Chen, Y. Wang, Y. Huang, X. Duan, *Nat. Mater.* **2013**, *12*, 246–252.
[129] W. J. Yu, Y. Liu, H. Zhou, A. Yin, Z. Li, Y. Huang, X. Duan, *Nat. Nanotechnol.* **2013**, *8*, 952–8.
[130] X. Wang, F. Xia, *Nat. Mater.* **2015**, *14*, 264–265.
[131] F. Withers, O. Del Pozo-Zamudio, A. Mishchenko, A. P. Rooney, A. Gholinia, K. Watanabe, T. Taniguchi, S. J. Haigh, A. K. Geim, A. I. Tartakovskii, et al., *Nat. Mater.* **2015**, *14*, 301–306.
[132] N. Huo, J. Kang, Z. Wei, S.-S. Li, J. Li, S.-H. Wei, *Adv. Funct. Mater.* **2014**, *24*, 7025–7031.
[133] R. Cheng, D. Li, H. Zhou, C. Wang, A. Yin, S. Jiang, Y. Liu, Y. Chen, Y. Huang, X. Duan, *Nano Lett.* **2014**, *14*, 5590–5597.
[134] B. Chen, N. Zhao, L. Guo, F. He, C. Shi, C. He, J. Li, E. Liu, *Nanoscale* **2015**, *7*, 12895–12905.
[135] D. Pham-Cong, J. H. Choi, J. Yun, A. S. Bandarenka, J. Kim, P. V. Braun, S.-Y. Jeong, C.-R. Cho, *ACS Nano* **2017**, 11, 1026–1033.
[136] H. Liu, X. Chen, L. Deng, M. Ding, J. Li, X. He, *J. Mater. Chem. A* **2016**, *4*, 17764–17772.
[137] Y.-J. Yuan, Z.-J. Ye, H.-W. Lu, B. Hu, Y.-H. Li, D.-Q. Chen, J.-S. Zhong, Z.-T. Yu, Z.-G. Zou, *ACS Catal.* **2016**, *6*, 532–541.
[138] P. Zhang, T. Tachikawa, M. Fujitsuka, T. Majima, *Chem. Commun.* **2015**, *51*, 7187–7190.
[139] W. Zhou, Z. Yin, Y. Du, X. Huang, Z. Zeng, Z. Fan, H. Liu, J. Wang, H. Zhang, *Small* **2013**, *9*, 140–147.
[140] N. Sakai, Y. Ebina, K. Takada, T. Sasaki, *J. Am. Chem. Soc.* **2004**, *126*, 5851–5858.

[141] T. Sasaki, Y. Ebina, T. Tanaka, M. Harada, M. Watanabe, G. Decher, *Chem. Mater.* **2001**, *13*, 4661–4667.

[142] N. Sakai, K. Fukuda, T. Shibata, Y. Ebina, K. Takada, T. Sasaki, *J. Phys. Chem. B* **2006**, *110*, 6198–6203.

[143] K. S. Novoselov, A. H. Castro Neto, *Phys. Scr.* **2012**, *T146*, 14006.

[144] V. Nicolosi, M. Chhowalla, M. G. Kanatzidis, M. S. Strano, J. N. Coleman, *Science* **2013**, *340*, 1226419.

[145] J. N. Coleman, M. Lotya, A. O'Neill, S. D. Bergin, P. J. King, U. Khan, K. Young, A. Gaucher, S. De, R. J. Smith, et al., *Science* **2011**, *331*, 568–571.

[146] A. Ciesielski, P. Samorì, *Chem. Soc. Rev.* **2014**, *43*, 381–398.

[147] Y. Hernandez, V. Nicolosi, M. Lotya, F. M. Blighe, Z. Sun, S. De, I. T. McGovern, B. Holland, M. Byrne, Y. K. Gun'Ko, et al., *Nat. Nanotechnol.* **2008**, *3*, 563–568.

[148] G. Cunningham, M. Lotya, C. S. Cucinotta, S. Sanvito, S. D. Bergin, R. Menzel, M. S. P. Shaffer, J. N. Coleman, *ACS Nano* **2012**, *6*, 3468–3480.

[149] M. B. Dines, *Mater. Res. Bull.* **1975**, *10*, 287–291.

[150] B. G. Silbernagel, *Solid State Commun.* **1975**, *17*, 361–365.

[151] M. S. Whittingham, F. R. Gamble, *Mater. Res. Bull.* **1975**, *10*, 363–371.

[152] M. A. Py, R. R. Haering, *Can. J. Phys.* **1983**, *61*, 76–84.

[153] P. Joensen, R. F. Frindt, S. R. Morrison, *Mater. Res. Bull.* **1986**, *21*, 457–461.

[154] G. Eda, H. Yamaguchi, D. Voiry, T. Fujita, M. Chen, M. Chhowalla, *Nano Lett.* **2011**, *11*, 5111–5116.

[155] Z. Zeng, Z. Yin, X. Huang, H. Li, Q. He, G. Lu, F. Boey, H. Zhang, *Angew. Chem. Int. Ed.* **2011**, *50*, 11093–11097.

[156] X. Huang, Z. Zeng, S. Bao, M. Wang, X. Qi, Z. Fan, H. Zhang, *Nat. Commun.* **2013**, *4*, 1444.

[157] G. Eda, T. Fujita, H. Yamaguchi, D. Voiry, M. Chen, M. Chhowalla, *ACS Nano* **2012**, *6*, 7311–7317.

[158] J. Heising, M. G. Kanatzidis, *J. Am. Chem. Soc.* **1999**, *121*, 11720–11732.

Chapter 2.
Insight into the Nature of Chemically Exfoliated MoS_2 in Aqueous Suspension

2.1. Introduction

Over the last few years, the study of atomically thin sheets of layered inorganic compounds, analogous to graphene, has emerged as an important area of nanoscience.[1–6] This includes layered transition metal oxides, such as $Ti_{1-\delta}O_2^{4\delta-}$, $Ca_2Nb_3O_{10}^-$, $MnO_2^{0.4-}$, and so on,[6–11] and chalcogenides, such as MoS_2, $MoSe_2$, WS_2, and so on.[1,4,12] Particularly, the intriguing properties of LTMD crystals have been studied for decades.[13] These materials have diverse properties to include metals, semiconductors, insulators, and superconductors.[4,13] Because of the weak van der Waals forces between the layers, LTMD crystals can be easily cleaved using adhesive tape.[14] The unique 2D structure of the exfoliated sheets is of beneficial for the fundamental study of ideal quantum systems.[15,16] In addition, the preparation of monolayer sheets of high quality is a pivotal step in providing the primary building blocks necessary to tailor a wide range of functional nanoarchitectures.[11,17–22]

Among the emerging 2D nanomaterials, MoS_2 nanosheets are of particular importance due to the unique physical and chemical properties related to their two dimensionality.[23–25] In addition, the electronic properties of MoS_2 can be altered from semiconducting to metallic and vice versa.[26–28] Therefore, MoS_2 has tremendous potential for a wide range of applications from electronics/optoelectronics to energy storage and catalysis.[29–34] Although MoS_2 nanosheets can be easily prepared *via* micromechanical cleavage, high quantities of monolayer single sheets is difficult to achieve, limiting its practical applicability for large-scale production. One solution to overcome such a limitation is preparing MoS_2 nanosheets *via* a chemical exfoliation method.[35] In this process, MoS_2 crystals are reductively intercalated by reacting with Li metals or organolithium compounds to produce lithiated crystals (Li_xMoS_2). Spontaneous exfoliation can be achieved by treating the lithiated crystals with water *via* ultrasonication, which yields of nearly 80-90% of well dispersed unilamellar nanosheets.

The high stability and quality of 2D nanomaterials are indeed of critically importance to guarantee their excellent properties and performance as well as their reproducibility. One challenge of chemically exfoliated MoS_2 is poor suspension stability and rapid quality degradation. Although the preparation of MoS_2 nanosheets *via* chemical exfoliation has been established since 30 years ago, insights into the mechanism, production of high-quality nanosheets, and their long-term stability have been limited. Therefore, in this chapter, the author intends to describe the detailed study of the nature and behavior of chemically exfoliated MoS_2, particularly in terms of their suspension stability, morphology, chemical and electronic nature, and phase and 2D structure.

2.2. Experimental Section

2.2.1. Chemical Exfoliation of MoS_2

Note that in this sub-section the author does not describe the detailed procedure for the preparation of MoS_2 nanosheets *via* chemical exfoliation. Instead, the author will only describe the key processes of the chemical exfoliation. The detailed procedure is provided in Appendix 1.

Following the procedure from Joensen *et al*.,[35] an amount of MoS_2 crystals was reacted with an *n*-butyllithium solution in an Ar-filled dry box. The lithiated MoS_2 was retrieved by filtration and washed with *n*-hexane. The lithiated MoS_2 was then exfoliated immediately in water with the aid of ultrasonication. The mixture was then centrifuged for several cycles to remove impurities and unexfoliated crystals.

2.2.2. Stability of MoS_2 Suspensions

We examined the suspension stability of the exfoliated MoS_2 nanosheets under two different atmospheric conditions, *i.e.*, an inert N_2 gas and ambient air. The UV-visible absorption spectra of the suspensions were measured periodically every five days. Stock suspensions (0.08 g dm^{-3}) were prepared and stored in glass vials equipped with a rubber-seal cap to avoid contamination from ambient air. The suspensions designated to be stored under an inert atmosphere were bubbled with N_2 gas for 1 h to remove oxygen gas. In contrast, the suspensions designated to be stored in ambient air were left without any treatment. Prior to the measurement, the suspensions were pipetted and diluted with degassed water until reaching a concentration of 0.008 g dm^{-3}. The UV-visible absorption spectra were measured immediately after the dilution.

2.2.3. Film Fabrication for Characterization

Concurrently, the quality of the exfoliated MoS_2 nanosheets was determined *via* AFM observations. The nanosheets were deposited on a Si substrate from their colloidal suspensions *via* electrostatic the layer-by-layer (LbL) self-assembly method.[36–38] First, the Si substrates were cleaned by being immersed in a 1:1 mixture solution of HCl/CH_3OH and concentrated H_2SO_4 for 30 min each. The substrates were primed with a 20 g dm^{-3} PDDA solution for 20 min to introduce a positive charge onto the surface. In the second step, for the morphological observation by AFM, the PDDA-modified substrate was dipped in a 0.02 g dm^{-3} MoS_2 suspension for 10 min to obtain sparsely distributed nanosheets on the substrate. For in-plane XRD and XPS measurements, the PDDA-modified substrate was immersed in a 0.08 g dm^{-3} MoS_2 suspension for 30 min to obtain a fully covered film.

2.2.4. Nanosheet Recovery and Restacking from the Suspensions

For the restacking experiment, the nanosheets were recovered from the colloidal MoS_2 suspension (0.5 g dm^{-3}) by centrifugation at 30,000 rpm. The resulting sediment was collected and deposited on a quartz-glass substrate (Figure 2.1) and dried overnight under a continuous flow of N_2 gas (~5% RH, RT). Drying in N_2

gas was essential to avoid any change during the process. The XRD measurements were performed on the specimens of restacked nanosheets shortly after drying.

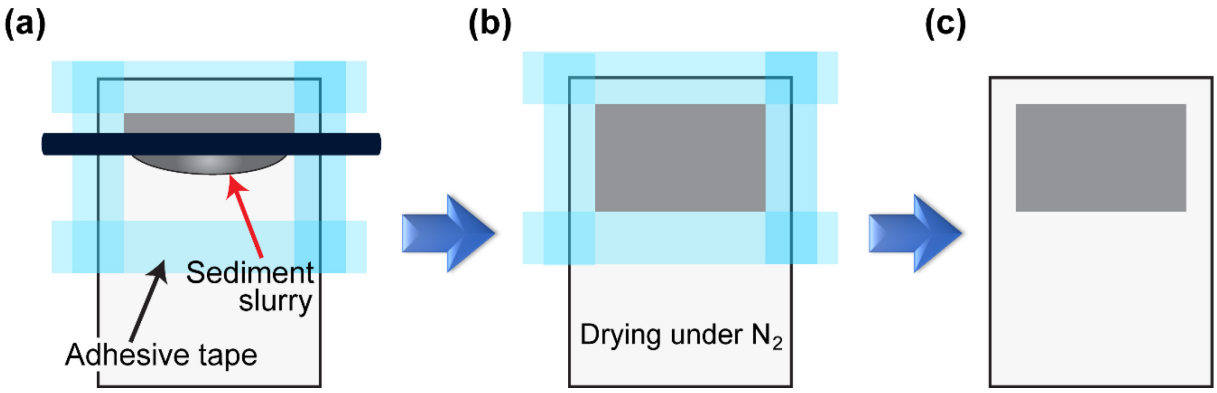

Figure 2.1. Sample preparation for nanosheet restacking experiments. (a) The sediment of nanosheets was spread on a quartz glass substrate by the doctor blading method. (b) Drying under a N_2 atmosphere. (c) The resulting specimen subjected to XRD analysis immediately after drying.

2.2.5. Characterization

The UV-visible spectra of the suspensions were measured with a Hitachi U-4100 spectrophotometer. The morphology, lateral size, and the thickness of the MoS_2 nanosheets were examined using a Hitachi SPA 400 AFM. In-plane XRD measurements were carried out using synchrotron X-ray radiation. XPS measurements were performed with a Thermo Scientific Theta Probe Thermo Electron (Al Kα radiation). TEM and SAED analyses were carried out using a JEOL JEM-3000F. Powder XRD measurements were performed with a Rigaku Rint ULTIMA IV diffractometer. The zeta potential values of the suspensions were measured using an ELS-Z zeta potential analyzer.

2.3. Results and Discussion

2.3.1. Nanosheet Stability and Quality

The behaviors of chemically exfoliated MoS_2 were examined upon storage of the suspensions in inert N_2 gas and in ambient air. UV-visible absorption spectroscopy was utilized to examine the stability of the suspended nanosheets at various Li contents. The Li content in the suspensions was adjusted with the addition of an appropriate amount of a LiOH solution with respect to the MoS_2. In this case, the Li ions served as the counter ions to maintain the suspension dispersibility, as indicated from the zeta potential value of the suspensions (see the details in Appendix 1). The suspensions that stored in an inert N_2 gas exhibited insignificant change in the UV-visible absorption spectra regardless of the Li content (Figure 2.2a-

c), indicating a high stable suspension. This feature was in accordance with the constant appearance of the suspensions (Figure 2.3a), even after two months of storage. In contrast, the sample stored in ambient air exhibited a gradual reduction in absorbance intensity over the entire spectral range (Figure 2.2d-f), indicating the instability of the nanosheets in the suspension. The reduction in absorbance intensity quickened with the increase in the Li content. Eventually, the suspension became transparent after storing in ambient air for more than two months (Figure 2.3b). A new peak was observed at 208 nm and became prominent with aging time; the peak could possibly attributed to the dissolved species in the suspension. The emergence of the new peak indicated the dissolution of the nanosheets upon storing in ambient air. Note that observation of the spectral range of 400-700 nm did not detect the intrinsic signatures of 2H MoS_2, which should show strong absorptions from interband transitions at approximately 430, 470, 610, and 660 nm,[23,28] suggesting that the nanosheets were predominantly exhibited the 1T character even after storing of up to 30 days.

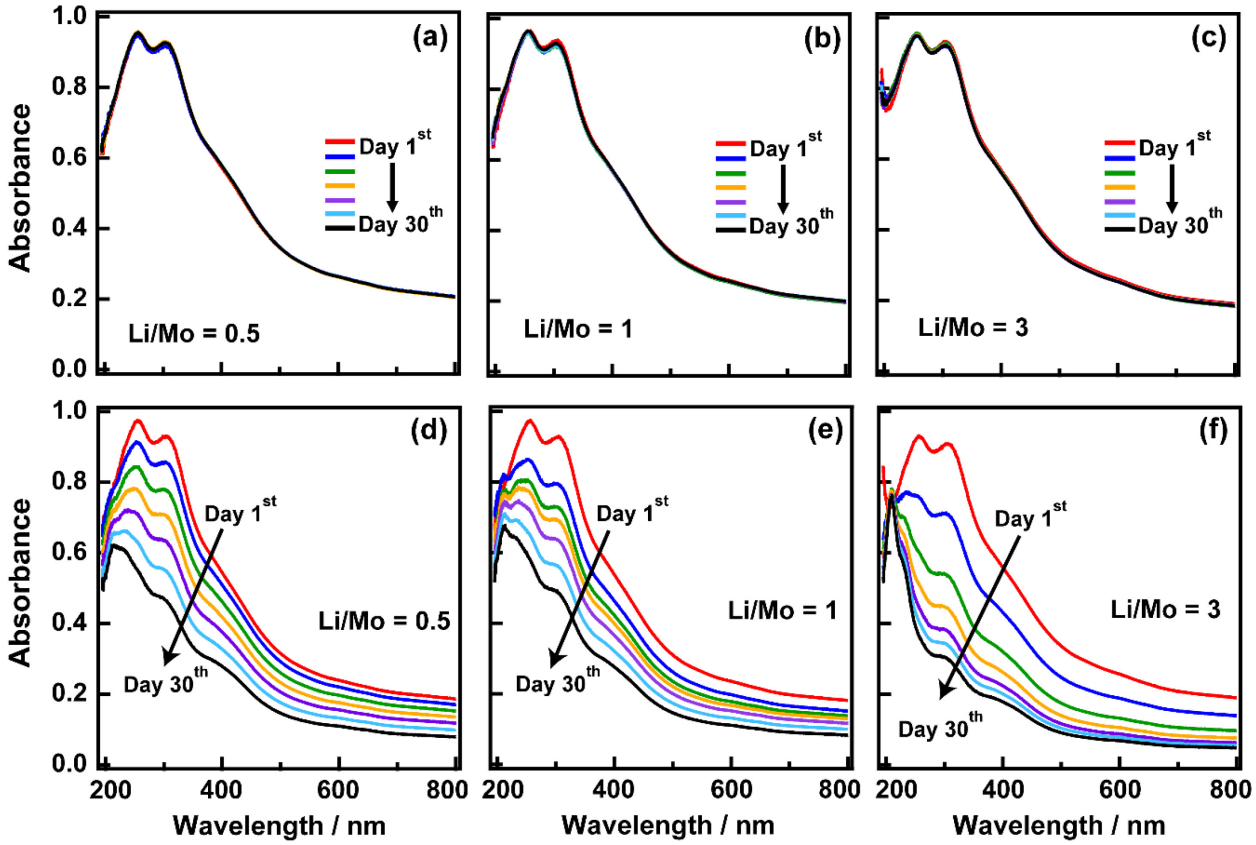

Figure 2.2. UV-visible absorption spectra of suspensions of chemically exfoliated MoS_2 with different Li contents (a-c) stored in inert N_2 and (d-f) stored in ambient air. The spectra were recorded every 5 days.

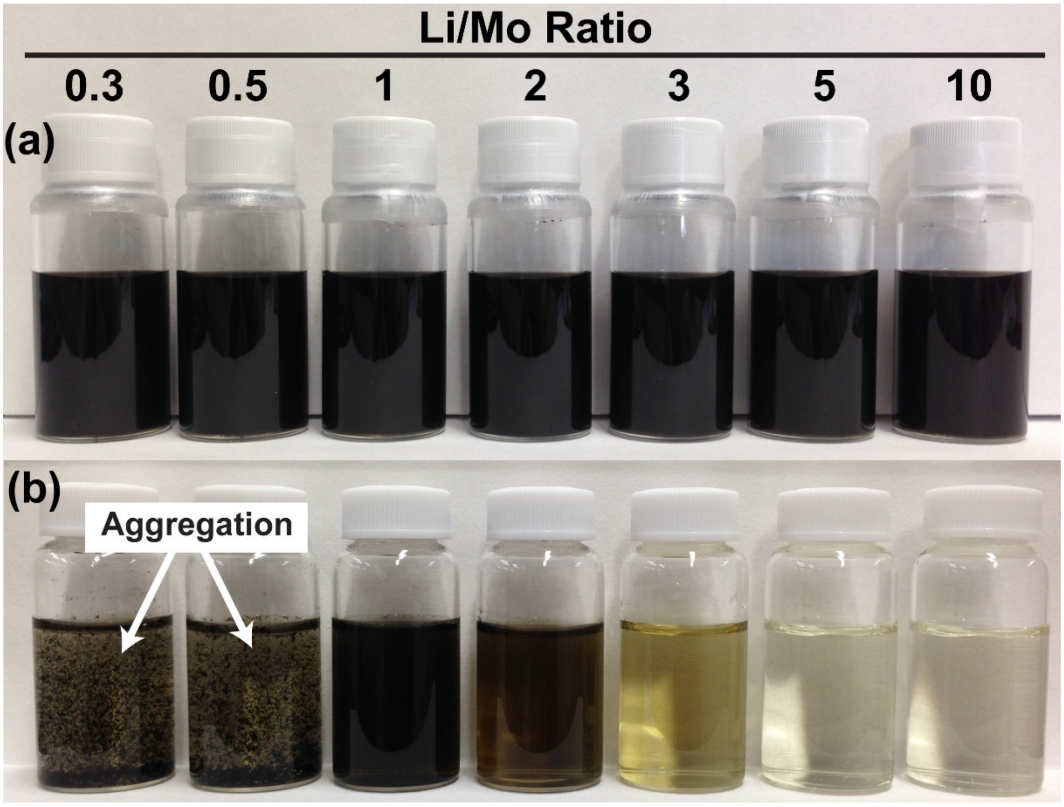

Figure 2.3. Photographs of MoS_2 suspensions stored for more than two months in (a) inert N_2 gas and (b) ambient air, with different Li contents in the suspensions

The morphology of the nanosheets were examined by AFM to determine the nanosheet quality. The nanosheet samples were sparsely deposited on a Si substrate. The freshly as-prepared MoS_2 nanosheets exhibited comparable well-defined 2D shapes and edges regardless of the Li content in the solution (Figure 2.4a-d). The lateral dimensions of the exfoliated nanosheets were found to be 0.3-1 μm with a unique thickness of ~1.2 nm, suggesting the unilamellar nature of the exfoliated nanosheets. Upon storing the suspension in the inert N_2 gas, the nanosheets retained their 2D morphologies (Figure 2.4e-h), indicating the maintained quality. In contrast, lateral fracture of the nanosheets into smaller fragments was resulted when the suspensions were exposed to ambient air. The fragments had a substantially smaller lateral dimension of <50 nm with a comparable thickness to those of the exfoliated MoS_2 nanosheets (~1.2 nm). The lateral fracture became more prominent with the Li content in the suspension. Clearly, the suspensions stored in air exhibited the stability and quality degradation over the entire Li content range and aging time. In fact, the complete dissolution of the nanosheets was produced from a high Li content, as indicated in Figure 2.3b.

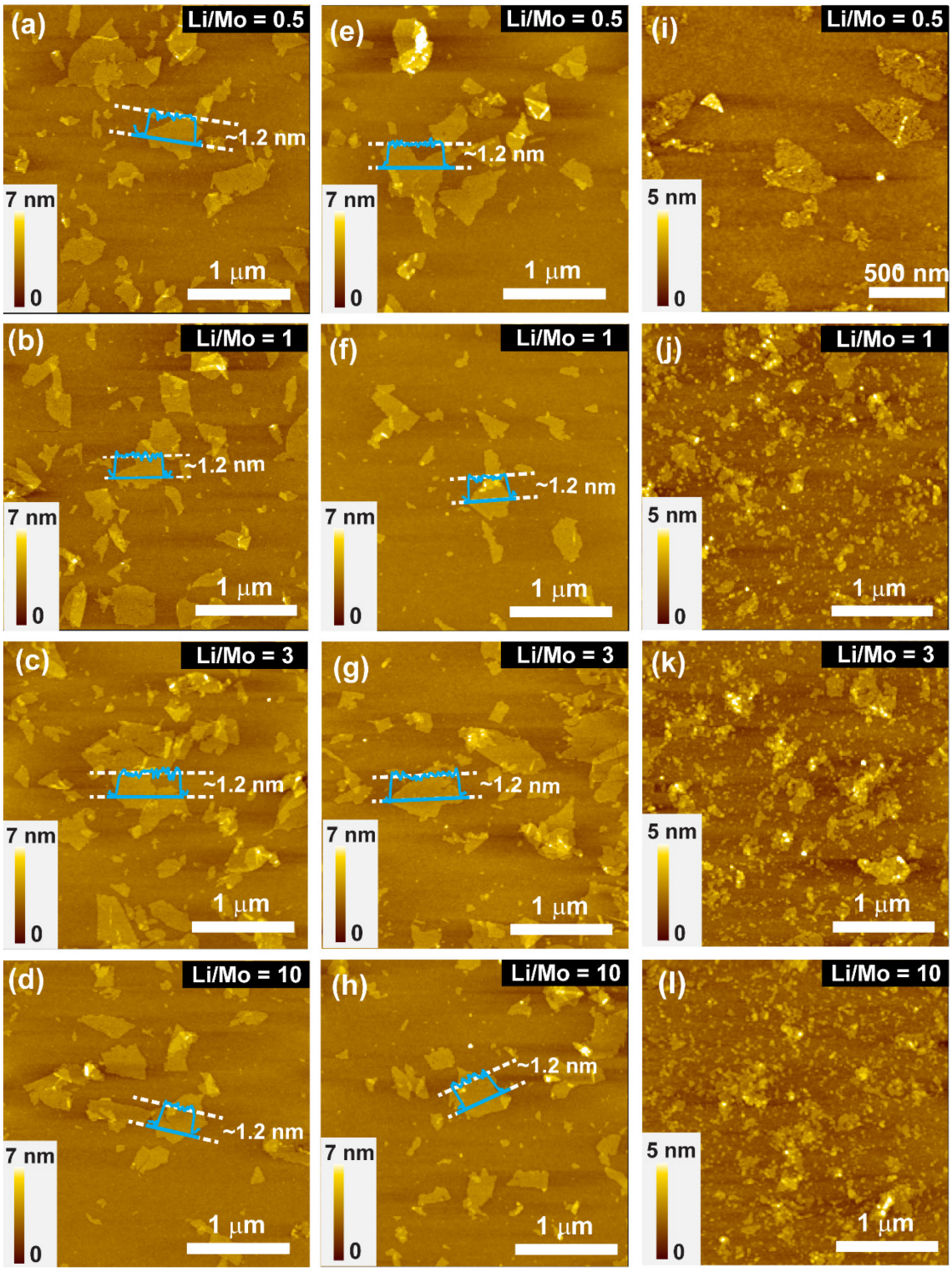

Figure 2.4. Taping mode AFM images of chemically exfoliated MoS_2 from (a-d) freshly prepared suspensions, (e-f) those stored in inert N_2 for 20 days, and suspensions stored in ambient air for (i,j) 10 days and (k,l) 5 days.

2.3.2. Electronic and Chemical Nature of the Nanosheets

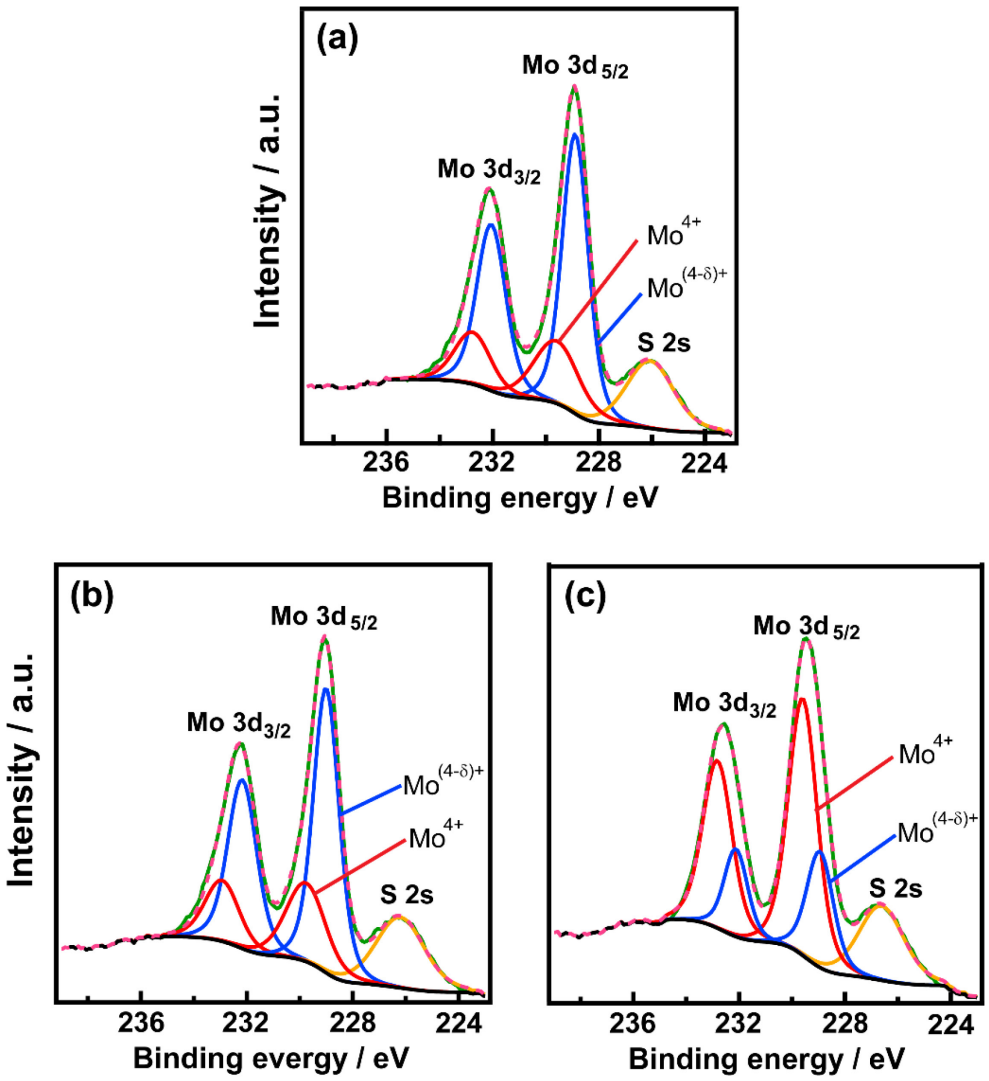

Figure 2.5. XPS spectra of the Mo 3d core levels of (a) freshly as-prepared MoS_2 nanosheets, and those from suspensions stored in (b) inert an N_2 gas and (c) ambient air for two months.

Clearly, the AFM observations of the MoS_2 nanosheets and the UV-visible absorption spectra of their suspensions showed different behaviors between the nanosheet suspensions stored in different atmospheric environments. The preparation of MoS_2 nanosheets *via* the chemical exfoliation method is initiated by the intercalation of an alkali metal, typically Li, into pristine MoS_2 layers and is followed by exfoliation in water with the aid of ultrasonication.[35] Considering that the Li intercalation of pristine MoS_2 is a reduction process,[39–42] it is assumed that the redox reaction that occurs in the nanosheets should be responsible for the stability and quality degradation of chemically exfoliated MoS_2. To gain insight into this aspect, we performed an XPS analysis to determine the oxidation states of the Mo 3d core levels of the nanosheets. Since the suspensions at high Li content (Li/Mo > 1) underwent severe dissolution at prolonged aging time

in ambient air, we only compared the chemical and electronic nature of the nanosheets from the suspensions at low Li content.

Figure 2.5 shows the XPS spectra of the Mo 3d core levels of the nanosheets from the freshly as-prepared suspension and those stored under different atmospheric environments. Two strong peaks were observed at binding energies of approximately 229 and 232 eV, which were ascribed to the Mo^{4+} $3d_{5/2}$ and $3d_{3/2}$ components, respectively. Upon chemical exfoliation, two additional peaks could be carefully discriminated after performing deconvolution of the Mo 3d peaks, which were shifted to lower binding energies relative to the energy bands of Mo^{4+} with a separation of ~0.8 eV.[28,43] The peak shifts to lower binding energies can be understood due to transfer of electrons from the valence *s* orbital of Li to the *d* orbital of Mo, which induces a reduction of the oxidation states of Mo from Mo^{4+} to $Mo^{(4-\delta)+}$.[44,45]

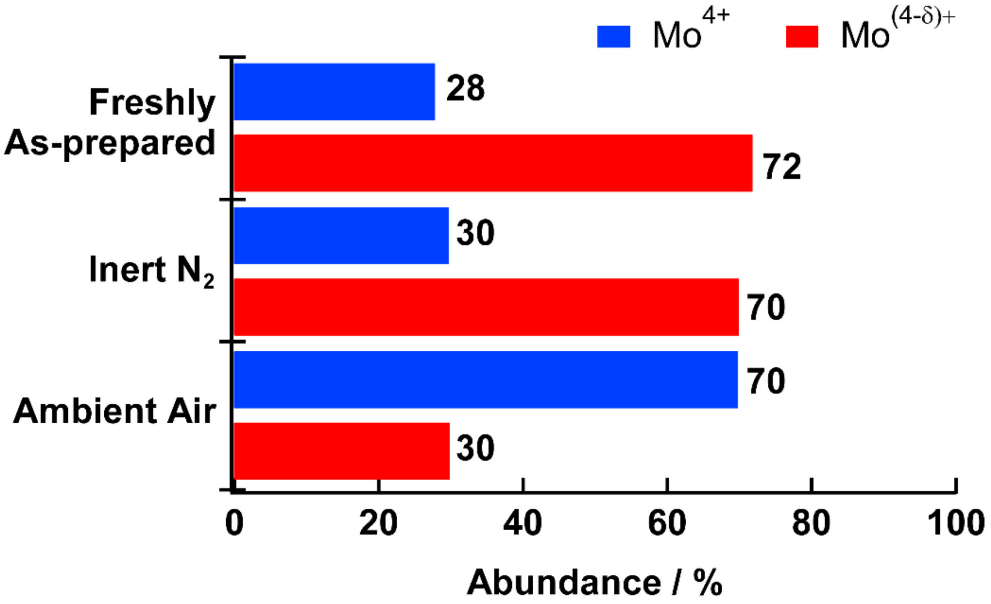

Figure 2.6. Abundancy of Mo^{4+} and $Mo^{(4-\delta)+}$ oxidation states, as deduced from XPS analysis of the Mo 3d spectra.

The abundance of the Mo^{4+} and $Mo^{(4-\delta)+}$ components were analyzed *via* peak fitting, the results of which are summarized in Figure 2.6. Clearly, the proportions of Mo^{4+} and $Mo^{(4-\delta)+}$ of the nanosheets from the freshly as-prepared suspension and that stored in the inert N_2 gas were nearly constant. This result indicated that, in theory, we could keep the nanosheets stably for more than two months. The abundancy of the samples from the suspensions with high Li contents (Li/Mo: 3 and 10) was also examined; this showed a comparable proportion of Mo^{4+} and $Mo^{(4-\delta)+}$ components, indicating that the Li content negligibly affected the chemical nature and bonding states of the nanosheets. In contrast, the sample from the suspension exposed to ambient air showed an increased proportion to approximately 70% for the Mo^{4+} component, suggesting that the nanosheets underwent a reoxidation process.

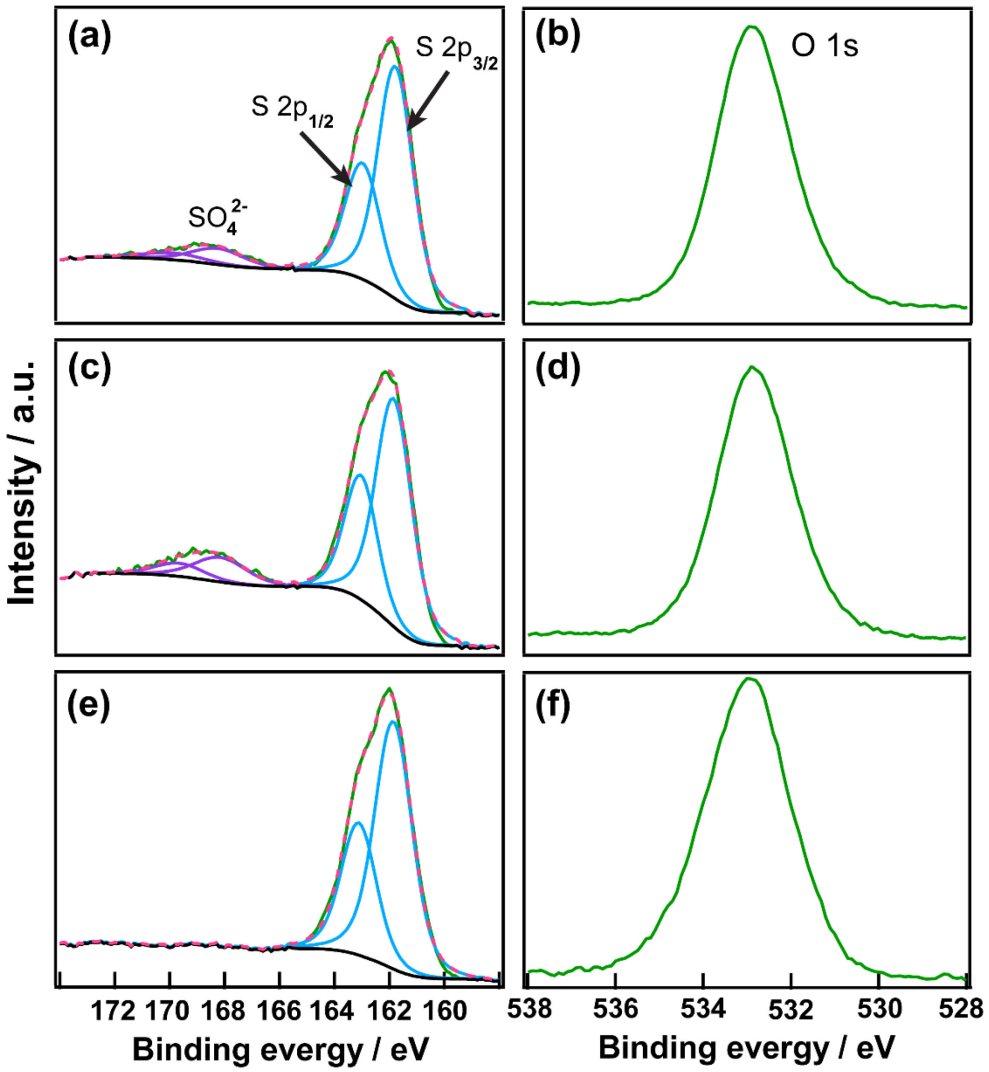

Figure 2.7. XPS spectra of S 2p and O 1s core levels of (a,b) freshly as-prepared MoS_2 nanosheets, and those from suspensions stored in (c,d) an inert N_2 atmosphere and (e,f) ambient air for two months.

To gain further insight into the reoxidation process of the nanosheets, the corresponding S 2p and O 1s spectra were examined (Figure 2.7). The S 2p peaks were identified at binding energies of approximately 161-164 eV, indicating the S^{2-} oxidation state. The analysis of the $S2p_{3/2}$ and $2p_{1/2}$ revealed that the spectra profiles were nearly comparable, suggesting that the change in the chemical nature and bonding states of the S atoms was negligible. A trace amount of sulfate species (~169 eV) was observed on the freshly as-prepared nanosheets and those stored in the inert, suggesting the partial oxidation of S atoms during the sample preparation. The spectra of O 1s located at binding energies of 531–535 eV only indicate the presence of oxygen from adventitious carbon (C–O–C: ~532 eV and C=O: ~533 eV) and the SiO_2 substrate (~533 eV), which were not related to the MoS_2 nanosheets. The presence of Mo-oxide species was hardly detected at ~530 eV, indicating that the oxidation of Mo to form Mo-oxide compounds was negligible. This assumption was further supported by the absence of Mo^{6+} $3d_{3/2}$ peaks at approximately 236 eV. From this

analysis, we may consider that the reoxidation apparently proceeds by discharging the residual negative charge of the nanosheets to the environment, which can be accounted for the destabilization of the suspension and the aggregation of the nanosheets. Thus, we can conclude that the suspension stability and nanosheet quality of chemically exfoliated MoS_2 is strongly influenced by the reoxidation process.

2.3.3. Behaviors of the Nanosheet Reoxidation Studied from the Structural Evolution of the Nanosheet Restacking

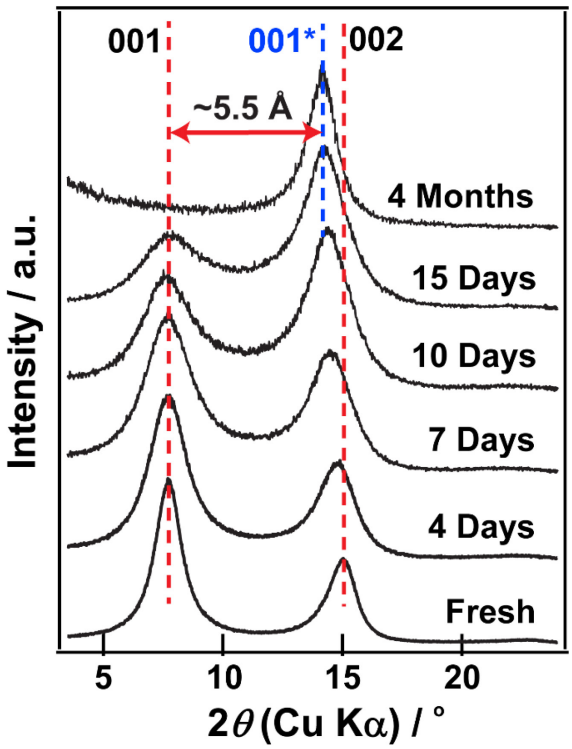

Figure 2.8. XRD patterns of restacked MoS_2 nanosheets with different periods of the suspension aging in ambient air.

The change in the chemical nature of chemically exfoliated MoS_2 upon the reoxidation process can be studied from the structural evolution of the restacked nanosheets recovered from the air-aged suspensions. Figure 2.8 displays the evolution of XRD patterns of the restacked nanosheets. The sample from the freshly as-prepared nanosheet suspension exhibited two pronounced diffraction peaks at 2θ values of approximately 7.7 and 15°, which were assigned as the 001 and 002 of the basal planes with an interlayer spacing of 1.18 nm. The intensities of the peaks gradually decreased with the aging process and were accompanied by the emergence of a new peak at a 2θ of approximately 14.2°. Finally, the peaks at $2\theta \cong$ 7.7 and 15° completely disappeared, leaving only the peak at $2\theta \cong$ 14.2° with a reduced interlayer spacing of 0.62 nm, which is

comparable to the spacing of 2H MoS_2. This suggests that the final products totally consisted of the reoxidized phase without the incorporation of guest species in the interlayer galleries. The interlayer shrinkage from the fresh sample to the final aged product was approximately 5.5 Å, which corresponds to the size of a water bilayer. Thus, the formation of the 1.18 nm phase could be ascribed to the expanded structure of the restacked MoS_2 sheets due to the intercalation of bilayer hydrates accommodating the Li ions.[46] A similar structural expansion based on intercalated bilayer hydrates has also been reported in NMR and XRD studies.[47,48] The interaction between the solvated Li ions and MoS_2 sheets can be understood based on an ionic model, where the $MoS_2^{\delta-}$ layers can be considered as quasi-two-dimensional macroanions having delocalized electrons, while the solvated Li ions serve as the counterions residing in the interlayer space.[49] During the reoxidation, the nanosheets discharged their residual electrons and eventually yielded in neutral sheets. Consequently, the expanded bilayer-hydrate phase collapsed into the deintercalated one.

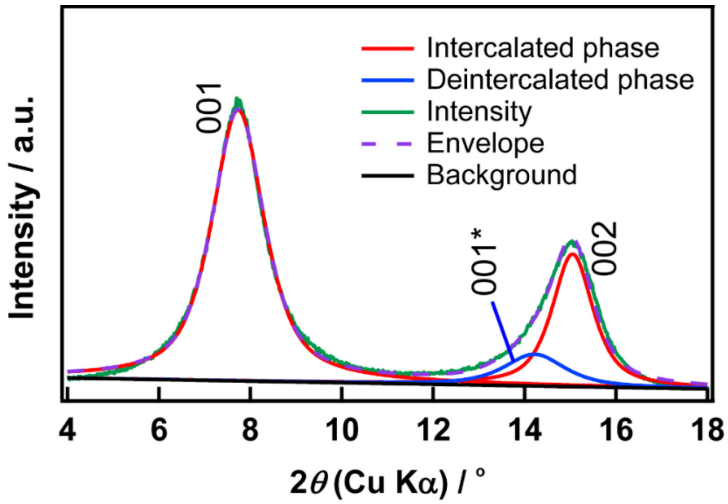

Figure 2.9. Typical deconvolution procedure of the XRD data of the restacked nanosheets.

Table 2.1. Area proportions of the intercalated bilayer-hydrate and deintercalated phases derived from deconvolution of the XRD data.

Suspension age	Area proportion	
	Intercalated bilayer hydrates	Deintercalated
Fresh (day 0)	0.90	0.10
Aged day 4	0.78	0.22
Aged day 7	0.66	0.34
Aged day 10	0.51	0.49
Aged day 15	0.30	0.70

The abundance of the intercalated bilayer-hydrate and the deintercalated phases was then estimated by correcting the proportional area of each phase, deduced from the deconvolution of the XRD data, by considering the intrinsic relative intensity. The deconvolution was performed on the basis of pseudo-Voigt function by assuming the peak positions of each phase (Figure 2.9). Table 2.1 tabulates the area proportions deduced from the integrated relative intensities of the 001 and 001* peaks for the intercalated bilayer-hydrate and the deintercalated phases, respectively. The intensities (I) of the basal diffraction series of the two phases were independently calculated using the following formulas, based on the structural models shown in Figure 2.10. The atomic positional parameters and site occupancies are given in Table 2.2.

$$I(\theta) = \frac{1 + \cos^2 2\theta}{\cos\theta \sin^2\theta} \cdot FF^* \tag{2.1}$$

$$F_{00l}(\theta) = \sum_j m_j f_j e^{2\pi i Z_j (2\sin\theta/\lambda)} \tag{2.2}$$

The first term of equation (2.1) represents the Lorentz-polarization factor and the second one is the structure factor. The variables m_j, f_j, and Z_j, are the site occupancy, atomic scattering factor, and atomic position along the z direction for the j^{th} atom, respectively. Meanwhile, θ and λ are the diffraction angle and X-ray wavelength (0.15405 nm), respectively.

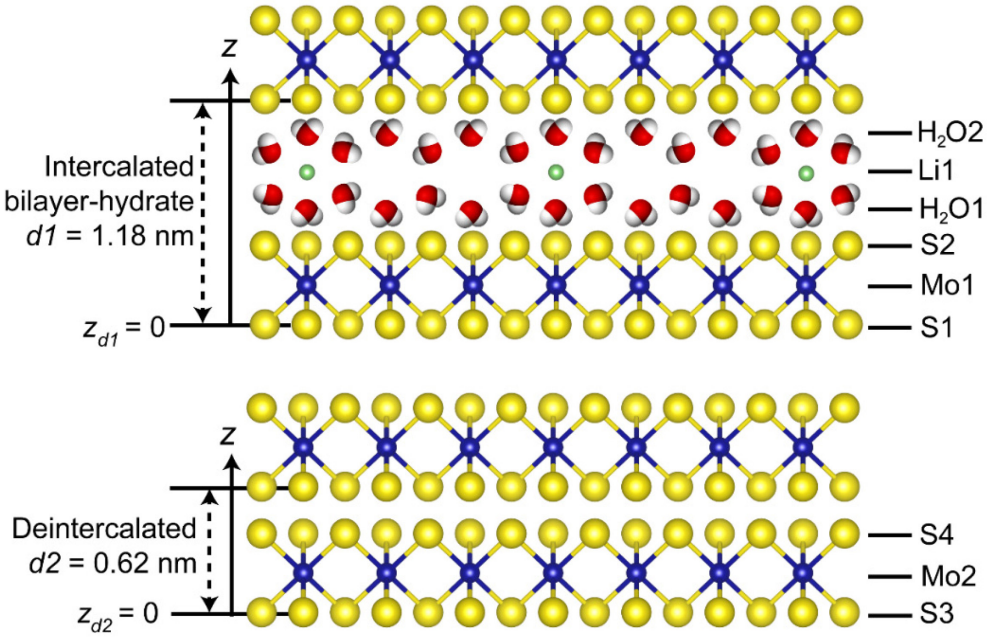

Figure 2.10. Diagram of the bilayer-hydrate and deintercalated structures of the restacked MoS_2 nanosheets.

Table 2.2. Atomic positional parameters (Z) and site occupancies (m) of each atom in the stacking direction.

Atom	m_j	Z_j (nm)
S1	1	0
Mo1	1	0.154
S2	1	0.308
H_2O1	1	0.627
Li1	0.33	0.748
H_2O2	1	0.870
S3	1	0
Mo2	1	0.154
S4	1	0.308

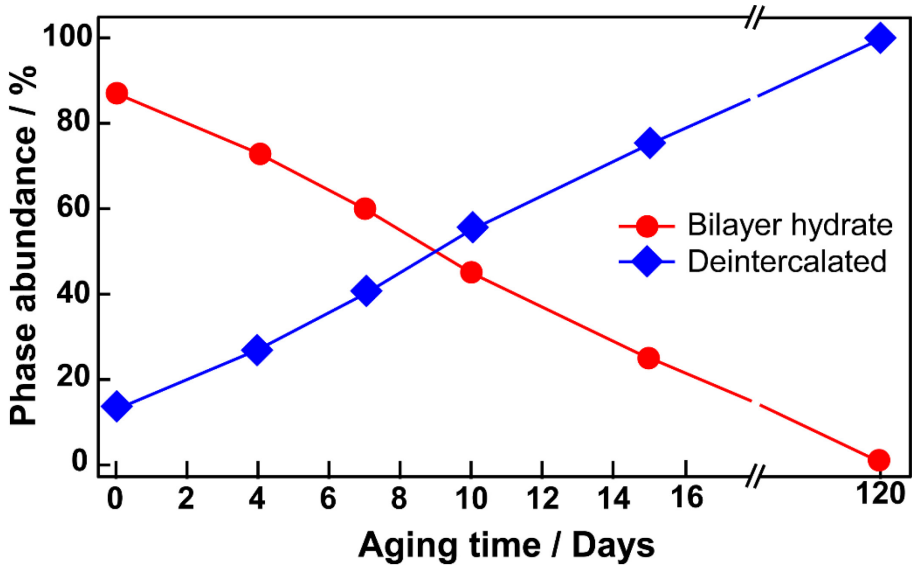

Figure 2.11. Estimated abundance values of the bilayer-hydrate and deintercalated phases *vs*. aging time of the suspension in ambient air.

Figure 2.11 and Table 2.3 summarize the estimated abundance values of the both phases. Upon the aging process up to 15 days, the decrease in abundance from 87% to 25% was observed in the expanded bilayer-hydrate phase. On the other hand, the deintercalated phase increased and eventually became predominant following the collapse of the bilayer hydrates due to the reoxidation process. Clearly, the changes in the abundance of both phases were inversely proportional from one to another. Thus, this structural change suggests that the reoxidation occurs sheet by sheet, implying the direct restoration of the oxidation states of the sheets to Mo^{4+}. Consequently, complete neutral sheets were resulted without involving the existence of intermediate states. To this point, a continuous change of the oxidation states should be unfavorable. Thus, the oxidation states of the sheets should be discrete only at two values of 4+

and (4−δ)+. The neutral sheets finally becomes predominant upon the continuous aging of the suspension, and can be considered as the completely reoxidized sheets. As a result, the sheets are completely restacked to the deintercalated MoS_2 layers. This evolution is in accordance with the XPS analysis, which shows the separation of two oxidation states of the Mo atoms.

Table 2.3. Corrected phase abundance values of the intercalated bilayer-hydrate and deintercalated phases.

Suspension age	Corrected phase abundance	
	Intercalated bilayer-hydrate	Deintercalated
Fresh (day 0)	0.87	0.13
Aged day 4	0.73	0.27
Aged day 7	0.60	0.40
Aged day 10	0.45	0.55
Aged day 15	0.25	0.75

2.3.4. Phase and Structure of the Exfoliated Nanosheets upon Aging Process

Preparation of MoS_2 nanosheets *via* the chemical exfoliation process is initiated by the reductive intercalation of Li into MoS_2 layers and accompanied by the phase transformation from trigonal prismatic 2H to octahedral 1T.[40,41,50] Unilamellar MoS_2 nanosheets are achieved by reacting the lithiated MoS_2 with water under ultrasonication, through which the resultant nanosheets obtain their 1T character and negatively charged nature.[27,51] It has been reported that the 1T-phase products of chemically exfoliated MoS_2 nanosheets are unstable and have a tendency to restore into the 2H phase after being aged or annealed in an inert atmosphere.[27,28,52] Note that, the nanosheet charge becomes neutral upon annealing, since the oxidation state of the MoS_2 is restored to the original Mo^{4+}.[28] However, the phase retransformation behavior of nanosheets undergoing reoxidation upon storing the suspension in ambient air has not been studied. There have been some confusion in the 2D-structural identification of chemically exfoliated MoS_2 and their phase restoration into the 2H.[53,54] Recent studies assumed that 1T/2H structures might coexist in chemically exfoliated MoS_2.[54,55] A new trend of a simplified analysis on the abundance quantification of the coexisting 1T/2H phases has been developed from the XPS spectra of the Mo 3d core levels. In practice, the abundance of 1T and 2H phases are associated with the doublet peak shifts deduced by the peak deconvolution.[28,56–59] However, this approach is seemingly not in accordance with the principle of XPS in which the kinetic energy of an ejected electron from the core level is measured to determine the change in the chemical bonding state of an atom, instead of to probe the structural arrangement. Consequently, this approach is under debate, as it provides a somewhat inconsistent estimation compared to a scanning tunneling electron microscope (STEM) observation, particularly for the reoxidized nanosheets.[54] The inconsistency may suggest that some

factors that contribute to the change in the chemical bonding state are ignored. Thus, we tried to examine the phase and 2D structure of the reoxidized nanosheets using in-plane XRD for the first time. Unlike other structural characterization tools (such as STEM, electron diffraction, *etc.*), in-plane XRD is reliable because it directly examines the 2D structure of the nanosheets and provides bulk and average structural information.

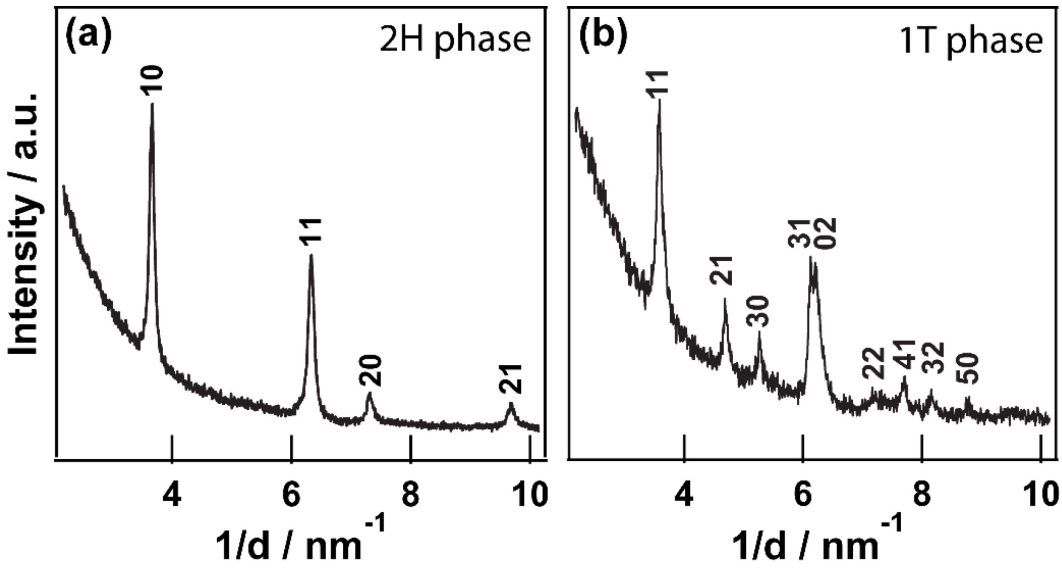

Figure 2.12. In-plane XRD patterns of typical (a) pristine 2H and (b) 1T phases of MoS_2 nanosheets. The pristine 2H MoS_2 was obtained after annealing in an Ar atmosphere at 300 °C.

Before examining the phase and structure of the reoxidized MoS_2 nanosheets, herein, we introduce the in-plane XRD patterns of the 2H and 1T phases of exfoliated MoS_2 nanosheets (Figure 2.12). Typically, the measurements for the in-plane XRD were performed using a monolayer film of nanosheets, deposited using electrostatic LbL self-assembly from freshly as-prepared nanosheets (1T phase), expecting that the nanosheets were in parallel with the substrate. The 2H phase of the MoS_2 was achieved by annealing the as-fabricated monolayer film of the 1T phase at 300 °C under an Ar atmosphere. Regardless of the phase, the MoS_2 nanosheets showed prominent peaks at 1/d = ~3.6 and ~6.2 nm^{-1}, which arose from the fundamental hexagonal lattice and confirmed the 2D hexagonal cell. The refined lattice constant was a = 0.3156(1) nm, which is in agreement with the unit cell parameter of 2H MoS_2.[39,55] In contrast, the exfoliated 1T phase exhibited a doublet peak at 1/d = ~6.2 nm^{-1}, with a difference in the d-spacing of 0.002-0.003 nm, suggesting a distortion from the hexagonal symmetry. Six weak diffraction peaks were identified at 1/d = 4.7, 5.3, 7.2, 7.7, 8.2, and 8.7 nm^{-1} and should arise from the superlattice structure, confirming the existence of the 1T phase MoS_2.

So far, the intrinsic 2D structure of chemically exfoliated 1T MoS_2 has not been comprehensively understood. Several superlattices, e.g., 2×2, √3×1, or √3×√3, have been reported from STEM observations and electron diffraction pattern analyses.[55,60–62] Since the observed in-plane XRD pattern suggested a

structural distortion from the hexagonal symmetry, we excluded the 2×2 and √3×√3 superstructures. The lattice-constant refinement (the least-squares method) was then performed only on the basis of a 2D rectangular cell of √3×1, exhibiting the lattice constants of a = 0.3202(2) and b = 0.5679(2) nm (where $b \approx \sqrt{3}a$). By neglecting the small distortion, we could approximate the average hexagonal-cell lattice-constant of the √3×1 superstructure to be 0.3244(2) nm, being comparable with those reported in previous studies.[52,60,62] This value was slightly larger than the lattice constant of the 2H phase. This suggests that there is an expansion on the 2D lattice of the 1T phase, which might have occurred upon chemical exfoliation. This behavior has been explained as a result of structural distortions based on the periodic cluster arrangement of Mo atoms.[63,64]

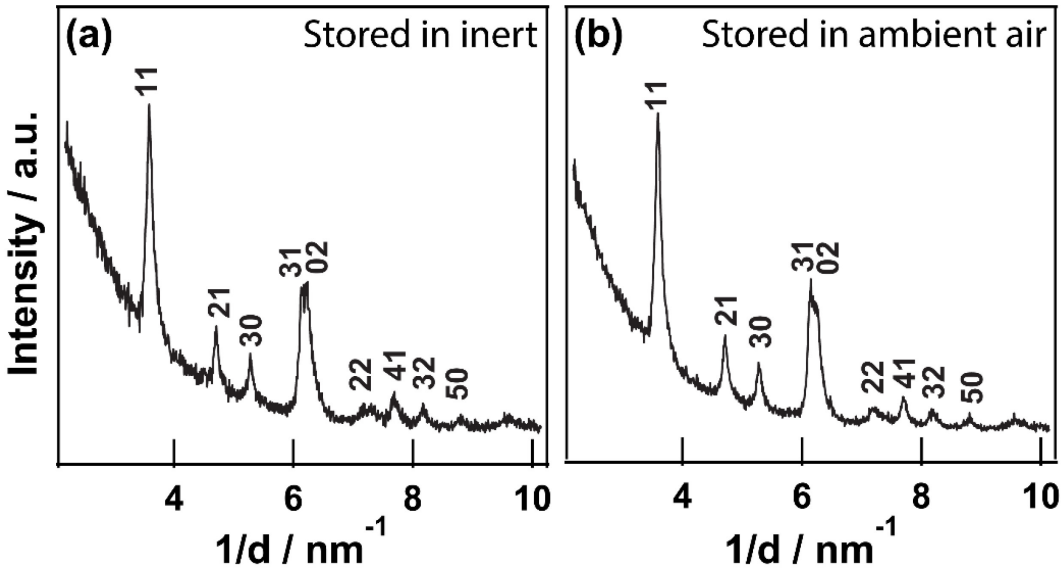

Figure 2.13. In-plane XRD patterns of chemically exfoliated MoS_2 from suspensions stored in (a) inert N_2 for two months and (b) ambient air for one month.

Table 2.4. Summary of the 2D lattice symmetry and lattice parameters of MoS_2 nanosheets from various treatments. (*)The lattice-parameter refinement was carried out on the basis of the √3×1 rectangular superstructure.

Sample treatment	2D Symmetry	Lattice parameters			
		a (nm)	*b* (nm)	*b/a*	Avg. Hex. lattice
2H phase (Annealed)	Hexagonal	0.3156(1)	-	-	-
Fresh as-prepared	Rectangular(*)	0.3205(2)	0.5687(2)	1.7744	0.3244(2)
Stored in inert N_2	Rectangular(*)	0.3207(3)	0.5684(3)	1.7724	0.3244(2)
Stored in ambient air	Rectangular(*)	0.3193(2)	0.5680(3)	1.7789	0.3236(2)

Figure 2.13 displays the in-plane XRD patterns of the nanosheets from suspensions stored in inert N_2 gas and in ambient air. Clearly, the two samples exhibited comparable 1T phase structures. Note that aging process did not significantly change the lattice constants of the nanosheets (Table 2.4), indicating that the nanosheets retained their 1T phase. To gain full insight into the structure of the reoxidized nanosheets, we prolonged the aging process of the suspension until the nanosheets completely aggregated. We then examined the structure using TEM and SAED analyses (Figure 2.14) for comparison to the sample used for the in-plane XRD characterization. Clearly, the aggregated nanosheets, which represented fully reoxidized states, also exhibited the 1T phase based on the $\sqrt{3}\times1$ superstructure, being comparable to that reported for the chemically exfoliated MoS_2 oxidized using I_2/Br_2.[27] This finding is different from the previously reported phase retransformation of chemically exfoliated MoS_2 upon annealing.[27,65] Thus, this suggests that the structural rearrangement from the octahedral (1T) to the trigonal-prismatic (2H) does not occur under such conditions, although the nanosheets were fully reoxidized, meaning that a structural reorganization by gliding of one of the S layers[66] may not proceed at room temperature. Thus, we may conclude that the reoxidized nanosheets are metastable structures of neutral 1T MoS_2.

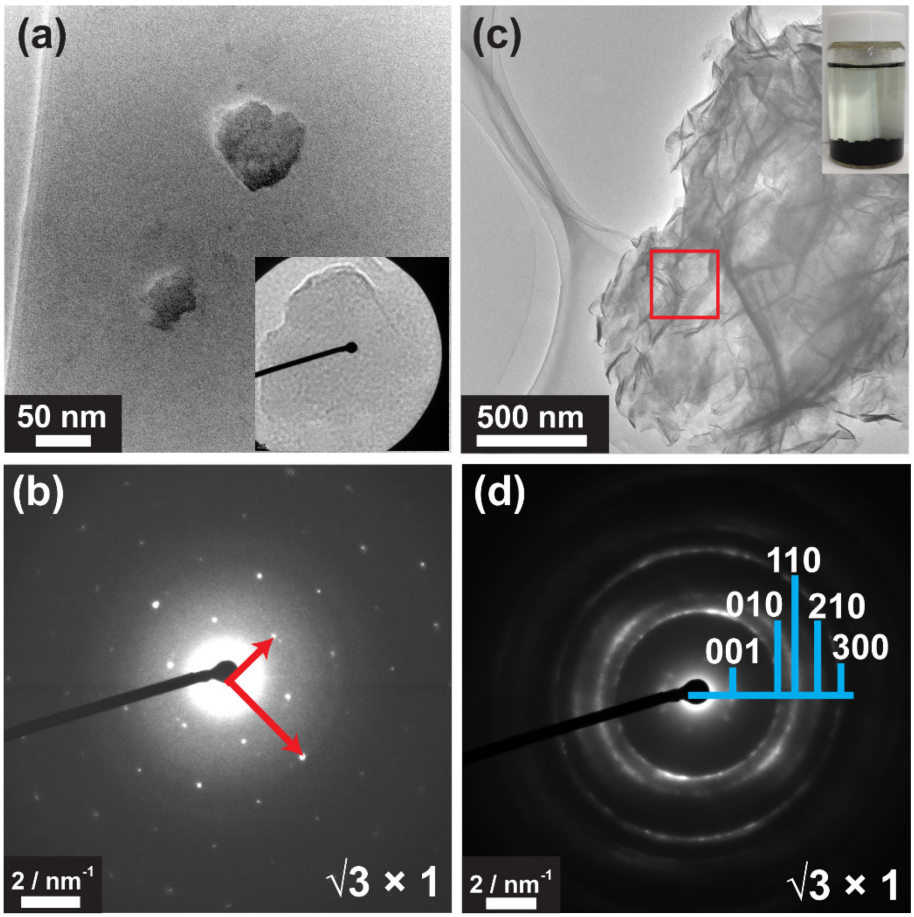

Figure 2.14. (a) TEM image of MoS_2 nanosheets recovered from the suspension exposed to ambient air for one month (similar sample to that used for the in-plane XRD). (b) Corresponding SAED pattern. (c) TEM image of aggregated nanosheets after aging of the suspension for four months. (d) Corresponding SAED pattern of aggregated nanosheets in the rectangle.

2.4. Summary

The behaviors of chemically exfoliated MoS_2 nanosheets in an aqueous suspension were examined from the viewpoint of their suspension stability, morphology, chemical and electronic nature, and phase and 2D structure. The stability and quality of the exfoliated nanosheets were confirmed to be associated with the reoxidation process. The reoxidation process brought about the loss of the residual negative charge of the nanosheets to the environment and induced lateral fractures and aggregations with the aging process. The restacking behavior of the nanosheets, studied from the XRD analysis, suggested that the chemically exfoliated MoS_2 were reoxidized sheet by sheet. In addition, the oxidation states of the sheets should be discrete only at two values of Mo^{4+} and $Mo^{(4-\delta)+}$. Upon the reoxidation, the nanosheets retained their 1T phase, although the charges of the nanosheets restored to neutral, yielding in a metastable neutral 1T MoS_2. Finally, the stability and quality of chemically exfoliated MoS_2 could be effectively maintained by storing the nanosheets in an inert atmosphere, which was critical to suppress the oxidation process.

2.5. References

[1] M. Chhowalla, H. S. Shin, G. Eda, L.-J. Li, K. P. Loh, H. Zhang, *Nat. Chem.* **2013**, *5*, 263–75.

[2] V. Nicolosi, M. Chhowalla, M. G. Kanatzidis, M. S. Strano, J. N. Coleman, *Science.* **2013**, *340*, 1226419.

[3] K. S. Novoselov, V. I. Fal'Ko, L. Colombo, P. R. Gellert, M. G. Schwab, K. Kim, *Nature* **2012**, *490*, 192–200.

[4] Q. H. Wang, K. Kalantar-Zadeh, A. Kis, J. N. Coleman, M. S. Strano, *Nat. Nanotechnol.* **2012**, *7*, 699–712.

[5] A. K. Geim, *Science.* **2009**, *324*, 1530–1534.

[6] R. Ma, T. Sasaki, *Acc. Chem. Res.* **2015**, *48*, 136–143.

[7] M. Osada, T. Sasaki, *J. Mater. Chem.* **2009**, *19*, 2503–2511.

[8] R. Ma, T. Sasaki, *Adv. Mater.* **2010**, *22*, 5082–5104.

[9] M. Osada, T. Sasaki, *Adv. Mater.* **2012**, *24*, 210–228.

[10] L. Wang, T. Sasaki, *Chem. Rev.* **2014**, *114*, 9455–9486.

[11] R. Ma, T. Sasaki, *Annu. Rev. Mater. Res.* **2015**, *45*, 111–127.

[12] X. Huang, Z. Zeng, H. Zhang, *Chem. Soc. Rev.* **2013**, *42*, 1934–46.

[13] J. A. Wilson, A. D. Yoffe, *Adv. Phys.* **1969**, *18*, 193–335.

[14] K. S. Novoselov, D. Jiang, F. Schedin, T. J. Booth, V. V Khotkevich, S. V Morozov, A. K. Geim, *Proc. Natl. Acad. Sci.* **2005**, *102*, 10451–10453.

[15] X. Du, I. Skachko, F. Duerr, A. Luican, E. Y. Andrei, *Nature* **2009**, *462*, 192–195.

[16] X. Qian, J. Liu, L. Fu, J. Li, *Science* **2014**, *346*, 1344–1347.

[17] A. K. Geim, I. V Grigorieva, *Nature* **2013**, *499*, 419–425.

[18] H. Wang, F. Liu, W. Fu, Z. Fang, W. Zhou, Z. Liu, *Nanoscale* **2014**, *6*, 12250–12272.

[19] D. Deng, K. S. Novoselov, Q. Fu, N. Zheng, Z. Tian, X. Bao, *Nat. Nanotechnol.* **2016**, *11*, 218–230.

[20] X. Wang, Q. Weng, Y. Yang, Y. Bando, D. Golberg, *Chem. Soc. Rev.* **2016**, *45*, 4042–4073.

[21] H. Lim, S. I. Yoon, G. Kim, A. Jang, H. S. Shin, *Chem. Mater.* **2014**, *26*, 4891–4903.

[22] B. V. Lotsch, *Annu. Rev. Mater. Res.* **2015**, *45*, 85–109.

[23] A. Splendiani, L. Sun, Y. Zhang, T. Li, J. Kim, C.-Y. Chim, G. Galli, F. Wang, *Nano Lett.* **2010**, *10*, 1271–1275.

[24] K. F. Mak, C. Lee, J. Hone, J. Shan, T. F. Heinz, *Phys. Rev. Lett.* **2010**, *105*, 136805.

[25] A. Ambrosi, Z. Sofer, M. Pumera, *Small* **2015**, *11*, 605–612.

[26] F. Wypych, R. Schöllhorn, *J. Chem. Soc., Chem. Commun.* **1992**, 1386–1388.

[27] J. Heising, M. G. Kanatzidis, *J. Am. Chem. Soc.* **1999**, *121*, 11720–11732.

[28] G. Eda, H. Yamaguchi, D. Voiry, T. Fujita, M. Chen, M. Chhowalla, *Nano Lett.* **2011**, *11*, 5111–5116.

[29] D. Lembke, S. Bertolazzi, A. Kis, *Acc. Chem. Res.* **2015**, *48*, 100–110.

[30] T. Wang, S. Chen, H. Pang, H. Xue, Y. Yu, *Adv. Sci.* **2017**, *4*, 1600289.

[31] M. A. Lukowski, A. S. Daniel, F. Meng, A. Forticaux, L. Li, S. Jin, *J. Am. Chem. Soc.* **2013**, *135*, 10274–10277.

[32] T. Stephenson, Z. Li, B. Olsen, D. Mitlin, *Energy Environ. Sci.* **2014**, *7*, 209–231.
[33] R. Ganatra, Q. Zhang, *ACS Nano* **2014**, *8*, 4074–4099.
[34] C. G. Morales-Guio, L.-A. Stern, X. Hu, *Chem. Soc. Rev.* **2014**, *43*, 6555–69.
[35] P. Joensen, R. F. Frindt, S. R. Morrison, *Mater. Res. Bull.* **1986**, *21*, 457–461.
[36] G. Decher, *Science.* **1997**, *277*, 1232–1237.
[37] T. Sasaki, Y. Ebina, M. Watanabe, G. Decher, *Chem. Commun.* **2000**, 2163–2164.
[38] T. Sasaki, Y. Ebina, T. Tanaka, M. Harada, M. Watanabe, G. Decher, *Chem. Mater.* **2001**, *13*, 4661–4667.
[39] M. S. Whittingham, F. R. Gamble, *Mater. Res. Bull.* **1975**, *10*, 363–371.
[40] M. A. Py, R. R. Haering, *Can. J. Phys.* **1983**, *61*, 76–84.
[41] P. J. Mulhern, *Can. J. Phys.* **1989**, *67*, 1049–1052.
[42] E. Benavente, M. A. S. Ana, F. Mendizabal, G. Gonzalez, *Coord. Chem. Rev.* **2002**, *224*, 87–109.
[43] C. a. Papageorgopoulos, W. Jaegermann, *Surf. Sci.* **1995**, *338*, 83–93.
[44] C. M. Julien, *Mater. Sci. Eng. Reports* **2003**, *40*, 47–102.
[45] H. Wang, Z. Lu, S. Xu, D. Kong, J. J. Cha, G. Zheng, P.-C. Hsu, K. Yan, D. Bradshaw, F. B. Prinz, et al., *Proc. Natl. Acad. Sci.* **2013**, *110*, 19701–19706.
[46] A. Lerf, R. Schöllhorn, *Inorg. Chem.* **1977**, *16*, 2950–2956.
[47] R. Schöllhorn, A. Weiss, *J. Less-Common Met.* **1974**, *36*, 229–236.
[48] V. Alexiev, H. Meyer zu Altenschildesche, R. Prins, T. Weber, *Chem. Mater.* **1999**, *11*, 1742–1746.
[49] R. Schöllhorn, in *Intercalation Chem.* (Ed.: M.S. Whittingham), Academic Press, **1982**, pp. 315–360.
[50] F. Wypych, K. Sollmann, R. Schöllhorn, *Mater. Res. Bull.* **1992**, *27*, 545–553.
[51] A. S. Golub', G. A. Protsenko, L. V. Gumileva, A. G. Buyanovskaya, Y. N. Novikov, *Russ. Chem. Bull.* **1993**, *42*, 632–634.
[52] D. Yang, S. J. Sandoval, W. M. R. Divigalpitiya, J. C. Irwin, R. F. Frindt, *Phys. Rev. B Condens. Matter Mater. Phys.* **1991**, *43*, 12053–12056.
[53] J. Heising, M. G. Kanatzidis, *J. Am. Chem. Soc.* **1999**, *121*, 638–643.
[54] G. Eda, T. Fujita, H. Yamaguchi, D. Voiry, M. Chen, M. Chhowalla, *ACS Nano* **2012**, *6*, 7311–7317.
[55] K. E. Dungey, M. D. Curtis, J. E. Penner-Hahn, *Chem. Mater.* **1998**, *10*, 2152–2161.
[56] X. Yang, J. Li, T. Liang, C. Ma, Y. Zhang, H. Chen, N. Hanagata, H. Su, M. Xu, *Nanoscale* **2014**, *6*, 10126–10133.
[57] X. Fan, P. Xu, D. Zhou, Y. Sun, Y. C. Li, M. A. T. Nguyen, M. Terrones, T. E. Mallouk, *Nano Lett.* **2015**, *15*, 5956–5960.
[58] Y. Wang, J. Z. Ou, S. Balendhran, A. F. Chrimes, M. Mortazavi, D. D. Yao, M. R. Field, K. Latham, V. Bansal, J. R. Friend, et al., *ACS Nano* **2013**, *7*, 10083–10093.
[59] L. Cai, J. He, Q. Liu, T. Yao, L. Chen, W. Yan, F. Hu, Y. Jiang, Y. Zhao, T. Hu, et al., *J. Am. Chem. Soc.* **2015**, *137*, 2622–2627.
[60] F. Wypych, T. Weber, R. Prins, *Chem. Mater.* **1998**, *10*, 723–727.

[61] L. Wang, Z. Xu, W. Wang, X. Bai, *J. Am. Chem. Soc.* **2014**, *136*, 6693–6697.

[62] X. R. Qin, D. Yang, R. F. Frindt, J. C. Irwin, *Phys. Rev. B Condens. Matter Mater. Phys.* **1991**, *44*, 3490–3493.

[63] M. Kan, J. Y. Wang, X. W. Li, S. H. Zhang, Y. W. Li, Y. Kawazoe, Q. Sun, P. Jena, *J. Phys. Chem. C* **2014**, *118*, 1515–1522.

[64] X. Rocquefelte, F. Boucher, P. Gressier, G. Ouvrard, P. Blaha, K. Schwarz, *Phys. Rev. B Condens. Matter Mater. Phys.* **2000**, *62*, 2397–2400.

[65] S. J. Sandoval, D. Yang, R. F. Frindt, J. C. Irwin, *Phys. Rev. B Condens. Matter Mater. Phys.* **1991**, *44*, 3955–3962.

[66] Y.-C. Lin, D. O. Dumcenco, Y.-S. Huang, K. Suenaga, *Nat. Nanotechnol.* **2014**, *9*, 391–396.

Chapter 3.

Two-Dimensional Heterointerface Structure of the Restacked-$Ti_{0.87}O_2^{0.52-}$/1T-Phase MoS_2 and its Photocatalysis for H_2 Generation

3.1. Introduction

The production of H_2 fuel by artificial photosynthesis has been considered a potential strategy for solving global energy problems due to its cleanliness, low cost, and environmental friendliness.[1,2] Starting from Fujishima's and Honda's work[3] on photoelectrochemical water splitting using a TiO_2 electrode, this photocatalytic process has attracted an abundance of research interest.[4–7] Since then, numerous attempts have been made in this field by utilizing/developing semiconductor materials with various nano-/microstructures.[8–11] However, the intrinsic characteristics of most semiconductor materials are unfavorable for the water reduction reaction. In general, the overall photocatalytic water splitting reaction involves three major steps:[12,13] (i) the absorption of light by a semiconductor to generate electron-hole pairs, (ii) charge separation and migration to the semiconductor surface, and (iii) the surface reaction for water reduction (to produce H_2) or oxidation (to produce O_2). The photogenerated electron-hole pairs in most semiconductors are unstable and easily recombine if there are no suitable active/reaction sites available on the surface.[12,13] Therefore, a medium is required to facilitate the catalytic reaction on the surface of the semiconductor.

In the photocatalytic systems, co-catalysts are generally employed to overcome this limitation, since the use of a co-catalyst is not only for effective charge separation in the photocatalyst but also for providing more active sites for the catalytic reaction.[12,14] Most of the photocatalysts studied thus far have been based on nanoparticles.[15–18] The impregnation of co-catalysts is required to realize a hetero-junction/interface with the semiconductor. However, the use of nanoparticle-based materials and the conventional impregnation method do not allow advanced control at the nanoscale regime. The particle-based hetero-junctions/interfaces that have been employed in such studies usually failed to achieve intimate and effective interfacial contact at a molecular level. Consequently, this led to an insufficient charge separation, high recombination rate, and low photocatalytic activity.

To overcome the aforementioned problem, the use of 2D nanomaterials[19–25] can be considered as a promising strategy, for both the photocatalyst such as titania ($Ti_{1-\delta}O_2^{4\delta-}$) nanosheets, and the co-catalyst such as MoS_2 nanosheets. This aspect is motivated by the capability of tailoring nanostructures of 2D nanomaterials to achieve desired "face-to-face" interfacial contact due to their excellent interfacial characteristic.[26] This unique feature brings an advantage to design/control functions originating from the molecular-level interfacial interactions of two different types of 2D crystals. In regard to this aspect, the author aims to develop a new class of photocatalyst material *via* the hetero-assembly of $Ti_{1-\delta}O_2^{4\delta-}$ nanosheets and 1T-phase MoS_2. $Ti_{1-\delta}O_2^{4\delta-}$ nanosheets are an excellent 2D-based photocatalyst material as they show intense UV light absorption due to their unique two-dimensionality.[27,28] Meanwhile, 1T-phase MoS_2 is

metallic and shows a high catalytic activity for H_2 evolution. Because of its excellent electrical conductivity[29–31] and abundant catalytically active sites on the plane surfaces and at the edges,[32–34] 1T-phase MoS_2 can be beneficial for improving the charge transfer kinetics of the hydrogen evolution reaction. To achieve highly efficient photocatalytic activity for H_2 generation from the hetero-assembly of $Ti_{1-\delta}O_2^{4\delta-}$ and MoS_2 nanosheets, the proper design of their interfacial coupling is needed.

In light of the discussion above, in this chapter, the author intends to describe the design of a 2D-heterointerface structure from the monolayer modification of restacked $Ti_{0.87}O_2^{0.52-}$ nanosheets with metallic 1T-phase MoS_2, as shown in Figure 3.1. Such a unique structure was fabricated *via* a facile two-step flocculation of the nanosheet colloidal suspensions, allowing the attachment of monolayer 1T-phase MoS_2 on restacked $Ti_{0.87}O_2^{0.52-}$ nanosheets and enabling their extensive interfacial contact. This feature is expected to facilitate the efficient separation of photogenerated electron-hole pairs in the $Ti_{0.87}O_2^{0.52-}$ nanosheets and allow for the fast injection of photogenerated electrons to the MoS_2 layers. In addition, this structure is regarded as a promising candidate for photocatalytic hydrogen generation due to the largely exposed MoS_2 surface, which acts as the electron collectors and catalytically active sites. The photocatalytic activity for hydrogen generation was examined with the restacked products dispersed in an aqueous methanol solution under UV light irradiation. The 2D-heterointerfaces of restacked-$Ti_{0.87}O_2^{0.52-}$/1T-phase MoS_2 nanosheets showed a highly efficient photocatalytic activity towards hydrogen evolution.

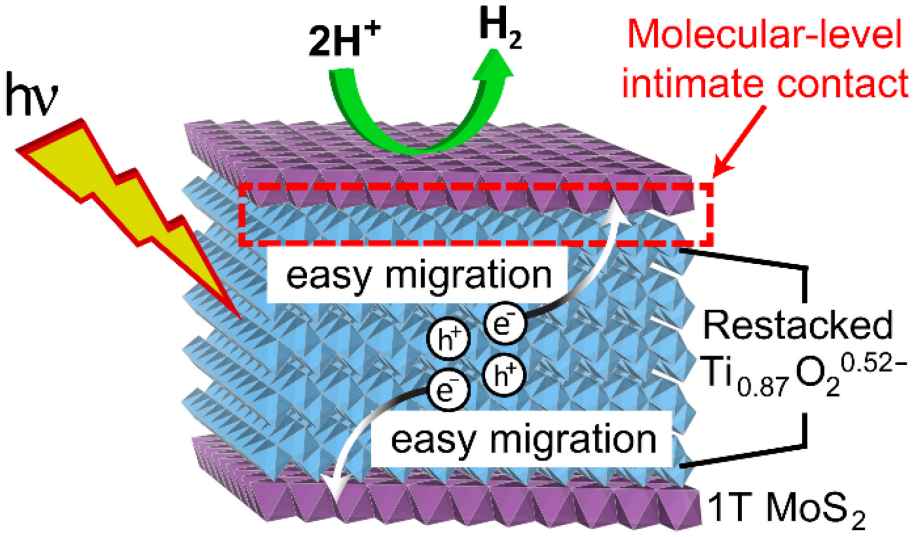

Figure 3.1. Schematic diagram of the 2D-heterointerface structure of the restacked-$Ti_{0.87}O_2^{0.52-}$/1T-phase MoS_2 nanosheets.

3.2. Experimental Section

3.2.1. Fabrication of the 2D-heterointerface Structures

A 2D-heterointerface structure of restacked-$Ti_{0.87}O_2^{0.52-}$/1T-phase MoS_2 was fabricated *via* a controlled flocculation, the so called two-step flocculation process. Colloidal suspensions of 1T-phase MoS_2 and $Ti_{0.87}O_2^{0.52-}$ nanosheets were prepared according to the procedures described in Appendix 1 and 2, respectively. First, a 200 cm^{-3} colloidal suspension (0.2 g dm^{-3}) of $Ti_{0.87}O_2^{0.52-}$ nanosheets was flocculated with the addition of 2 cm^3 of an HCl solution (0.5 mol dm^{-3}) under vigorous stirring. In the second step, a designated amount of 1T-phase MoS_2 suspension (0.6-10 wt% to the $Ti_{0.87}O_2^{0.52-}$) was added at a constant rate of 1 cm^3 min^{-1}. The resulting products were recovered by centrifugation, washed with water, and freeze dried.

3.2.2. Characterization

The structures of the restacked products were examined by a powder XRD, Rigaku Rint ULTIMA IV diffractometer. The morphology of the samples was observed with an SEM equipped with EDS (Horiba). The specimens were coated with Pt to minimize the charging effect. TEM observations and the SAED analysis were performed with a JEOL JEM-3000F. A Quantachrome Autosorb-1 was used to record the isotherm data of N_2 adsorption/desorption. The XPS analysis was performed with a Thermo Scientific Theta Probe Thermo Electron (Al Kα radiation) at the Ti 2p, Mo 3d, and S 2p core levels. The intensities of the Mo 3d and S 2p spectra were normalized to the corresponding Ti 2p. The optical properties of the samples were examined using a UV-visible spectrophotometer, Shimadzu SolidSpec 3700 DUV, in diffuse reflectance mode. The zeta potential measurement was carried out using an ELS-Z zeta potential analyzer. The acidity of the suspension/solution was measured with a Horiba LAQUAact pH meter.

3.2.3. Photocatalytic Reaction Test

Photocatalytic tests for H_2 generation from an aqueous methanol solution were carried out as follows: 1 mg of the photocatalyst powder was suspended in 2 cm^3 of an aqueous 10 vol% methanol solution in an airtight quartz reaction cell (4 cm^3 capacity). An outer jacket was employed and sealed with Polytetrafluoroethylene (PTFE) tape. Prior to each run, the reaction cell was purge with Ar gas for 30 min. The Ar gas stream was then injected into the outer jacket to prevent air contamination during the photocatalytic test. Under constant stirring, the dispersion was irradiated using a UV light source (San-Ei electric XEF-501S, λ = 300–500 nm) with an intensity of 19 mW cm^{-2}. Throughout the test, 0.05 cm^3 of a headspace gas sample was collected with an airtight syringe every hour. The evolved H_2 gas in the gas sample was analyzed using gas chromatography, Shimadzu GC-14, MS-5A column, Ar carrier, TDC.

Commercial TiO_2 nanoparticles (P25, Japan Aerosil, anatase:rutile = 70:30, with a specific surface area of 55 ± 15 m^2 g^{-1}) were used for comparative photocatalytic experiments.

3.2.4. EIS Measurement

A 2.4 mg photocatalyst powder sample was dispersed in a 1:4 mixed solution (v/v) of water and propanol (0.4 cm^{-3}), and then 0.01 cm^{-3} of a Nafion solution (10 wt%) was added. The suspension was sonicated for 30 min to prepare a homogeneous ink. The working electrode was prepared by dropping the catalyst ink onto a glassy carbon electrode with a diameter of 3 mm (catalyst loading of 0.25 mg cm^{-2}) and subsequent drying at room temperature.

The electrochemical impedance spectroscopy (EIS) measurements were conducted on a CH Instruments 760E electrochemical station using a 0.5 mol dm^{-3} aqueous H_2SO_4 solution as the electrolyte. Coiled platinum wire and an Hg/Hg_2SO_4 electrode (= +0.657 V vs NHE) were used as the counter electrode and reference electrode, respectively. The measurements were performed in the dark under an Ar atmosphere at the same current density of 10^{-2} mA cm^{-2}. A sinusoidal AC voltage was applied at a 5 mV amplitude in a frequency range of 0.1-10^5 Hz.

3.3. Results and Discussion

3.3.1. Construction of the 2D-Heterointerface Structure

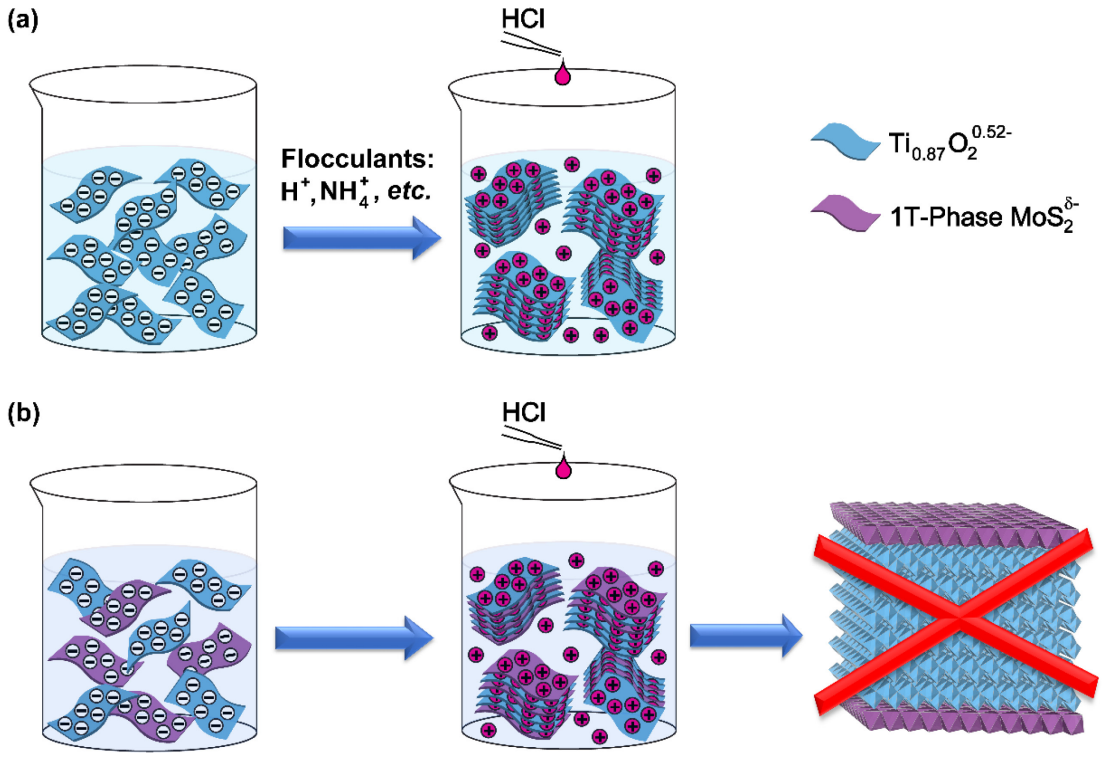

Figure 3.2. (a) Schematic diagram of the flocculation process. (b) Schematic diagram for the flocculation of a mixture colloidal system of $Ti_{0.87}O_2^{0.52-}$ and MoS_2 nanosheets. Flocculation of a mixture colloidal system fails to yield a heterointerface structure due to random restacking.

The fabrication of the 2D-heterointerface structure of restacked-$Ti_{0.87}O_2^{0.52-}$/1T-phase MoS_2 nanosheets was carried out by controlling the flocculation process. Flocculation is the slow aggregation of a colloidal system in the form of flocs or flakes, when the energy barrier among the surface of the particles is low.[35,36] The low energy barrier is attributed to a low charge density or potential on the particle surface, either spontaneously or induced by the addition of a flocculant (such as metal salts, protons (H^+), ammonium ions (NH_4^+), *etc.*). As shown in Figure 3.2a, flocculation of $Ti_{0.87}O_2^{0.52-}$ nanosheets was performed by adding HCl as the flocculant. In practice, a colloidal suspension of $Ti_{0.87}O_2^{0.52-}$ nanosheets at 0.2 g dm^{-3} was flocculated using 5 mmol dm^{-3} of HCl. Considering a mixture colloidal system of $Ti_{0.87}O_2^{0.52-}$/MoS_2 nanosheets (Figure 3.2b), the addition of HCl failed to yield a heterointerface structure due to random restacking. To this regard, control of the flocculation process was needed to construct the heterointerface structure that had been previously designed (Figure 3.1).

The flocculation process of a colloidal system can be predicted from DLVO theory. DLVO theory describes the potential energy of an interaction (W) by considering the net energy between the van der Waals attraction (*vdWs*) and electrostatic repulsion (R) of adjacent colloids. Van der Waals forces are typically always present, as they arise from the dipole-dipole interactions of atoms or molecules. Particular attention should be addressed to the electrostatic repulsions, as they result from the interactions of the charged surfaces of adjacent colloids, which depend on the surface charge density per unit area of the colloids and the ionic strength of the solution. The ionic strength is equal to the concentration of the salt or electrolyte in the solution, which is inversely proportional to the degree of the repulsive component.

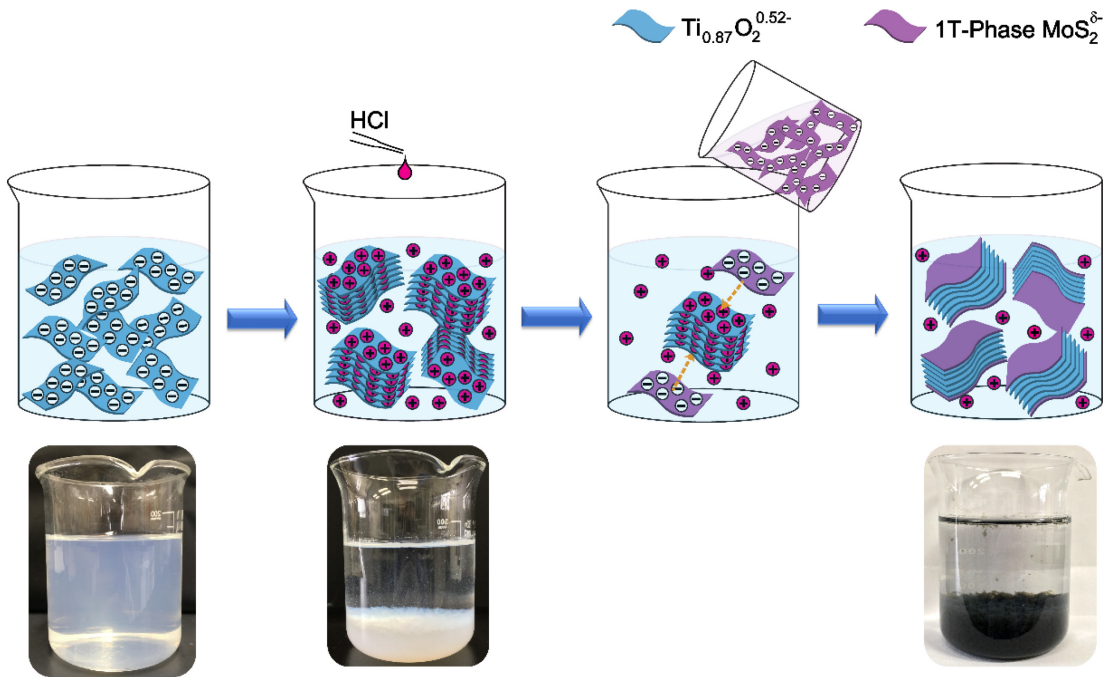

Figure 3.3. Schematic diagram of the fabrication of the 2D-heterointerface structure of restacked-$Ti_{0.87}O_2^{0.52-}$/1T-phase MoS_2 nanosheets *via* a two-step flocculation process.

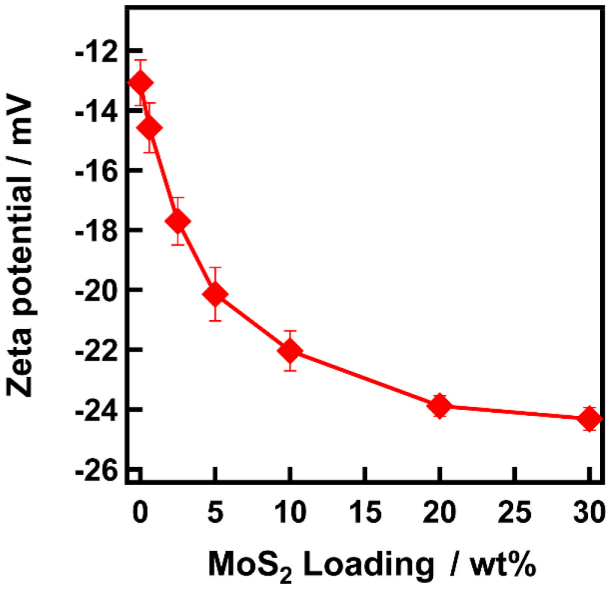

Figure 3.4. Zeta potential values of restacked $Ti_{0.87}O_2^{0.52-}$ nanosheets after the addition of a designated amount of MoS_2 nanosheets.

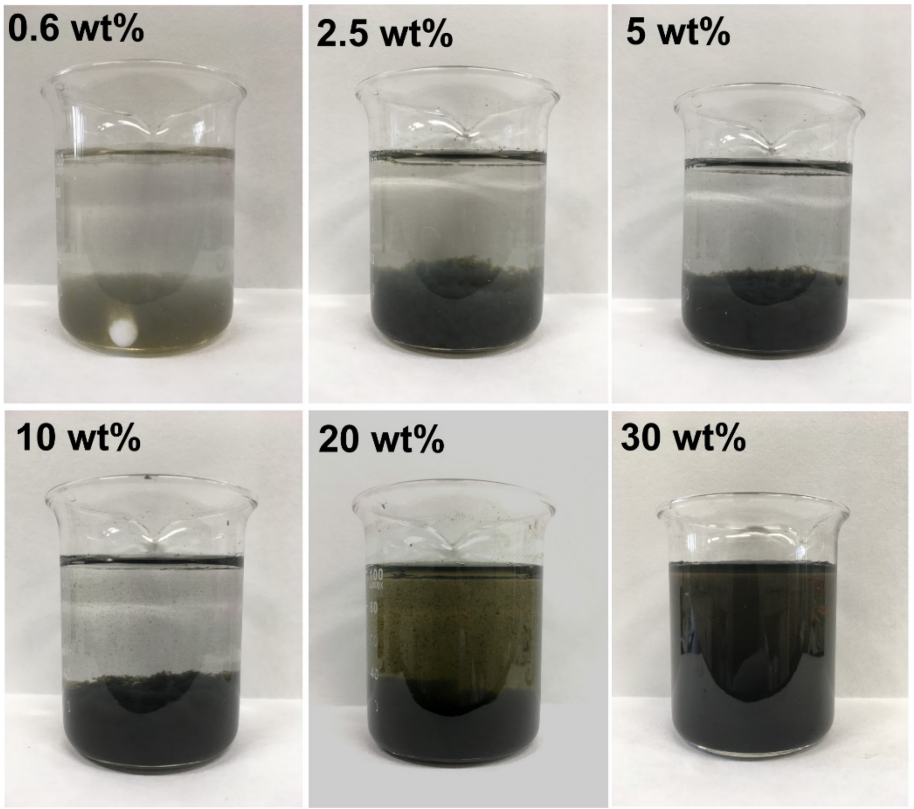

Figure 3.5. Photographs of the flocculated products for different MoS_2 loadings, after being redispersed under ultrasonication for 5 min and left to settle.

According to the brief description of the DLVO theory above, we know that each suspension system requires a specific amount of a flocculant to induce flocculation. It was found that the colloidal suspension of 1T-phase MoS_2 required a 5-fold dose higher of HCl, used to flocculate $Ti_{0.87}O_2^{0.52-}$ nanosheets, to induce flocculation. Thus, controlling the amount of HCl by utilizing the concentration differences is critical to allow the attachment of 1T-phase MoS_2 on restacked $Ti_{0.87}O_2^{0.52-}$ nanosheets and to prevent the self-flocculation of the MoS_2 nanosheets. We named this fabrication route as a two-step flocculation process. In addition to that, we could control the attachment feature and the coverage of MoS_2, which should affect the photocatalytic activity, by adjusting the loading amount of MoS_2.

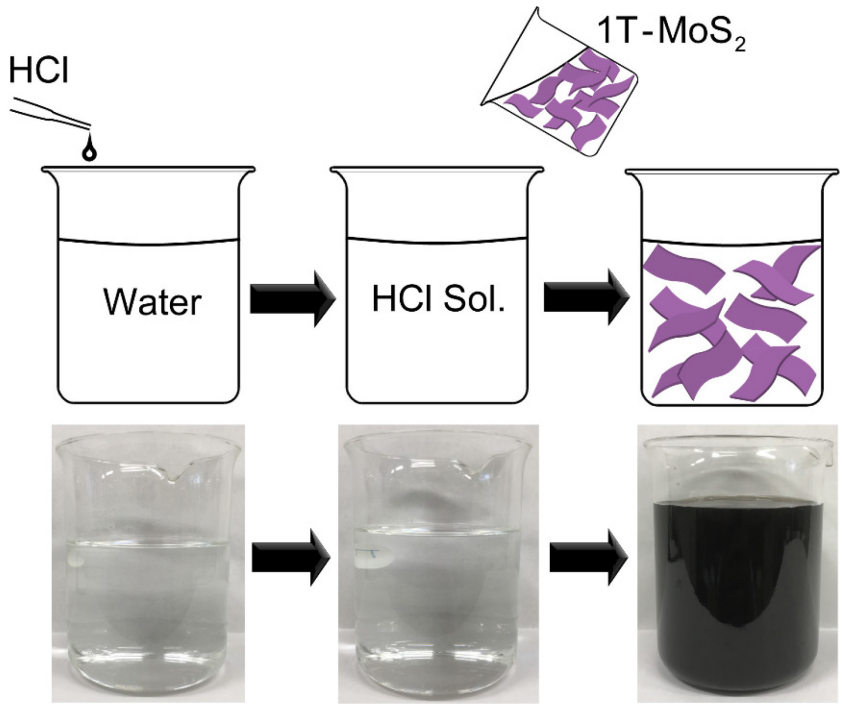

Figure 3.6. Flocculation control test of 1T-phase MoS_2 dispersion using an equal amount of HCl required to flocculate the $Ti_{0.87}O_2^{0.52-}$ nanosheets.

Figure 3.3 shows the schematic diagram of the two-step flocculation process. The colloidal suspension of $Ti_{0.87}O_2^{0.52-}$ nanosheets immediately underwent flocculation with the addition of HCl (pH = ~2.3), resulting in a voluminous white precipitate of restacked $Ti_{0.87}O_2^{0.52-}$ nanosheets. pH Measurement indicated that ~70% of H^+ ions were dispersed in the solution after the flocculation, some portions of which might be adsorbed and screen the surface of restacked $Ti_{0.87}O_2^{0.52-}$ nanosheets, as indicated from the zeta potential measurement that increased from approx. −39 to −13 mV. Upon the addition of MoS_2 nanosheets, the color of the precipitate changed to black, indicating the adsorption and attachment of the MoS_2 nanosheets on the restacked $Ti_{0.87}O_2^{0.52-}$. The adsorption and attachment of 1T-phase MoS_2 could be understood as an electrostatic-coupling interaction with $Ti_{0.87}O_2^{0.52-}$ nanosheets *via* the intervention of H^+. The attachment of the MoS_2 nanosheets were confirmed by the changes in the zeta potential to more negative values with

respect to the MoS_2 loadings (Figure 3.4). It was found that the attachment of 1T-phasse MoS_2 was robust, as suggested by the transparent supernatant even after redispersion under ultrasonication (Figure 3.5). Through this synthetic process, we believe that the MoS_2 nanosheets do not flocculate themselves. This was confirmed by a flocculation control test of a MoS_2 dispersion alone using an equivalent amount of HCl (Figure 3.6), which showed the absence of precipitate. The zeta potential value of the MoS_2 dispersion was ca. –41 mV and did not change significantly after the addition of HCl (pH was ~2.33). This suggested that the mixture formed a stable dispersion due to sufficient mutual repulsion.[37]

3.3.2. Structure and Morphology of the Restacked Flocculates

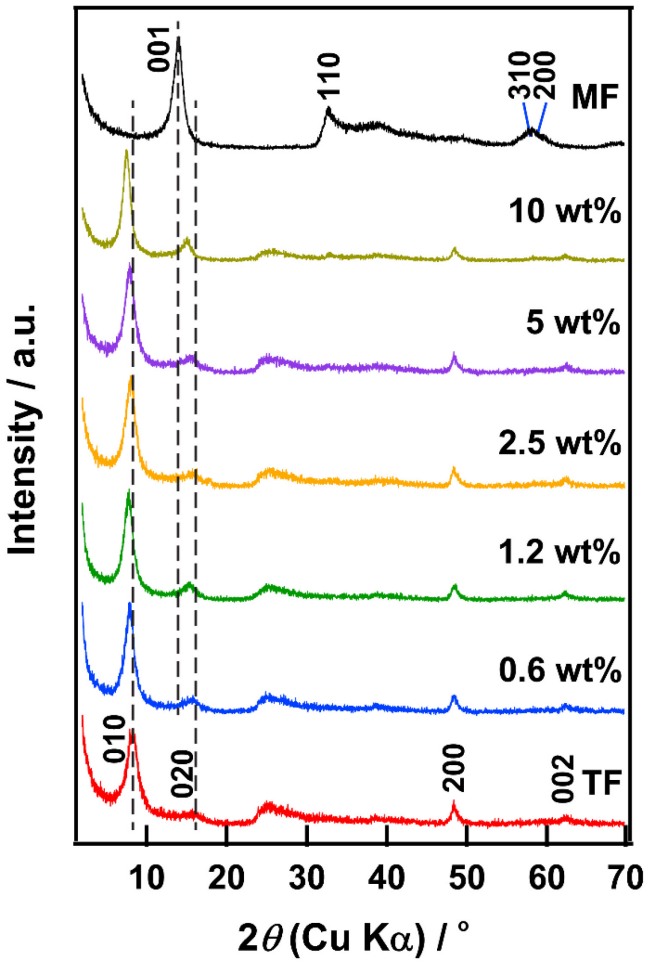

Figure 3.7. XRD patterns of the restacked flocculates at controlled MoS_2 loadings up to 10 wt%. TF and MF are restacked $Ti_{0.87}O_2^{0.52-}$ and 1T-phase MoS_2, respectively.

Figure 3.7 shows the XRD patterns of the restacked products. In general, the XRD patterns exhibited diffraction peaks at 2θ approximately 8.2, 16.5, 48.6, and 62.8° for the restacked $Ti_{0.87}O_2^{0.52-}$ alone and those

modified with MoS_2. The former two diffraction peaks were indexable as the 010 and 020 planes of the basal series of the restacked $Ti_{0.87}O_2^{0.52-}$, indicating a lamellar structure with an interlayer spacing of ~1 nm. The two latter peaks were attributed to the intrasheet reflections from the 200 and 002 diffraction bands of the $Ti_{0.87}O_2^{0.52-}$ nanosheets, indicating that the restacked products retained the 2D structure of the $Ti_{0.87}O_2^{0.52-}$ nanosheets after the flocculation and the addition of MoS_2 nanosheets. One of the interesting features here was the absence of general *hkl* reflections, which indicated the turbostratic nature of the restacked structure without three-dimensional order. After the addition of MoS_2, a slight shift of the basal peaks towards low diffraction angles was observed, which corresponded to an expansion of the interlayer spacing from 0.04 to 0.1 nm. Nevertheless, the lamellar structure of the MoS_2-modified samples remained intact, since the expansion was negligible. Note that the basal peak corresponding to the restacked MoS_2 nanosheets (2θ = ~14°) was hardly observed, thus, corroborating our presumption that the self-flocculation of MoS_2 nanosheets was negligible. To this point, the MoS_2 nanosheets might attach as a unilamellar form.

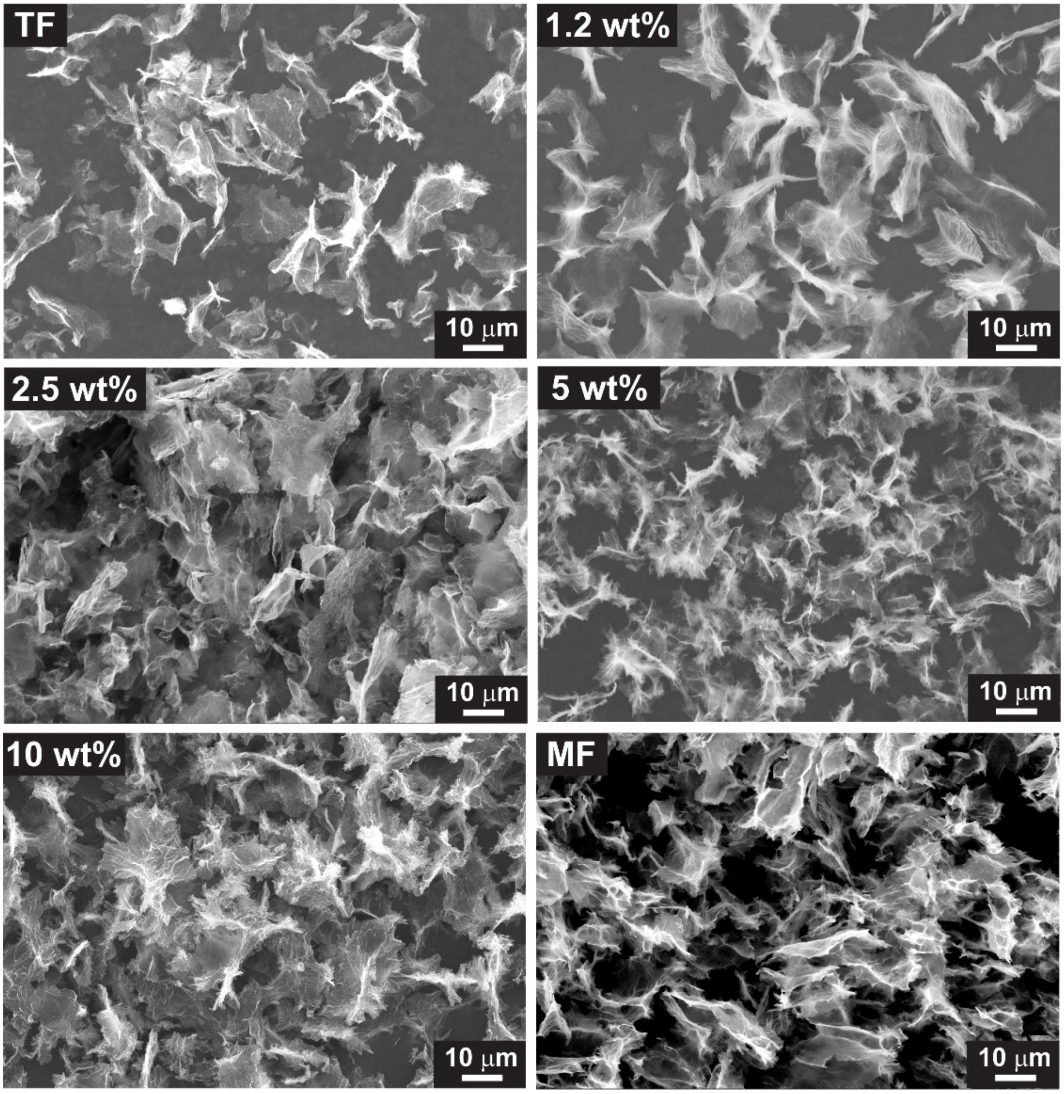

Figure 3.8. SEM images of the restacked flocculates at different MoS_2 loadings. TF and MF are restacked $Ti_{0.87}O_2^{0.52-}$ and 1T-MoS_2 nanosheets alone, respectively.

The morphology of the restacked samples exhibited a large agglomeration of irregularly flaky particles (Figure 3.8). Although the restacked products had a larger thickness than that of the original nanosheets, their two-dimensional character was essentially preserved. The individual flakes could be characterized by the high aspect ratio of their large lateral dimensions (10-20 μm) versus their ultrathin thickness (tens of nanometers). No microstructural changes were observed after the addition of MoS_2, which was due to the morphological similarity and highly flexible nature of the individual nanosheets. Thus, this feature indicated that the MoS_2 should be intimately attached on the restacked $Ti_{0.87}O_2^{0.52-}$ nanosheets.

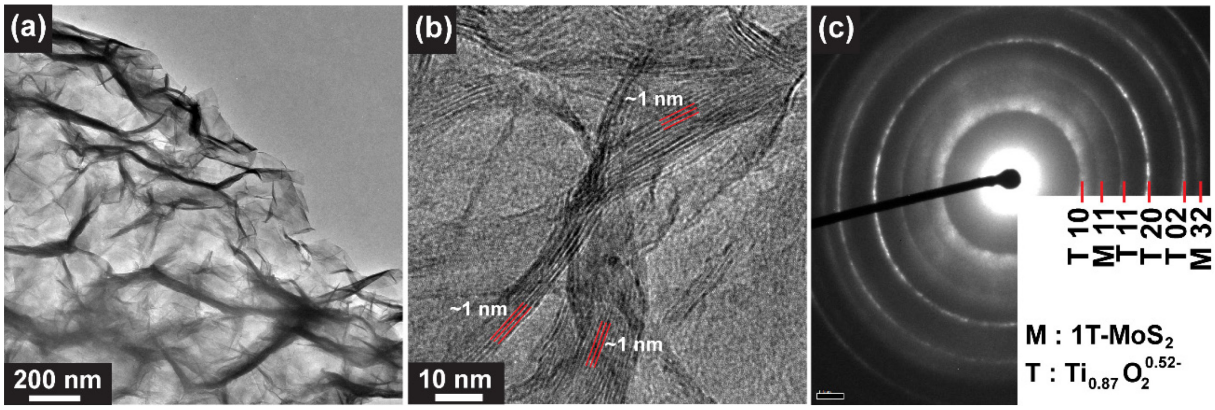

Figure 3.9. (a) TEM image of MoS_2-modified restacked-$Ti_{0.87}O_2^{0.52-}$ (10 wt% MoS_2), (b) corresponding high-resolution TEM image, and (c) SAED pattern (indexed at in-plane series).

TEM observations were used to further characterize the microstructure of the restacked flocculates. The agglomerated samples were composed of several nanosheet stacks (Figure 3.9a), as identified from the edge regions of the restacked nanosheets. The high-resolution TEM image indicated that the restacked nanosheets exhibited a lamellar lath-like texture of nanoscale thickness with an open and loose microstructures (Figure 3.9b). The apparent thickness of the lath-like morphology was 10-15 nm, which was exceptionally small and consisted of 10-15 nanosheet stacks. Thus, these features are of advantage to provide a high surface area and improve the surface contact with the catalyst materials. In addition, reducing the photocatalyst dimension is beneficial to reduce the recombination of photogenerated electrons and holes during the migration to the photocatalyst surface. Therefore, the designed material is favorable for catalytic reaction due to the largely exposed MoS_2 nanosheets as the catalytically active sites.

To confirm the presence of 1T-phase MoS_2, we performed a SAED analysis (Figure 3.9c). Clearly, 1T-phase MoS_2 existed in the restacked $T_{0.87}O_2^{0.52-}$ nanosheets, as indicated from 11 and 32 in-plane diffraction rings of the 2D $\sqrt{3}\times1$ superstructure of 1T MoS_2.[38] However, the high-resolution TEM observation only identified the restacked $T_{0.87}O_2^{0.52-}$ nanosheets, showing lattice fringes with an interlayer spacing d = ~1 nm. The restacked MoS_2 nanosheets, which should show a smaller interlayer spacing d = ~0.6 nm, was not

detected, although we performed observations over 20 different locations. The presence of MoS_2 was further confirmed by XPS and EDS elemental mapping analysis. The gradual increase in the intensities of the Mo 3d and S 2p spectra was consistent with the increase in the MoS_2 loading (Figure 3.10a). Meanwhile, the EDS elemental mapping analysis indicated that MoS_2 nanosheets were uniformly distributed on the restacked $T_{0.87}O_2^{0.52-}$ nanosheets (Figure 3.10b). According to the various characterizations that were performed, we can conclude that the presence of MoS_2 is confirmed on the restacked $T_{0.87}O_2^{0.52-}$ nanosheets. However, this is hardly identified at the nanoscale regime. Thus, this suggests that the MoS_2 nanosheets may attach only on the surface of the restacked $T_{0.87}O_2^{0.52-}$ nanosheets within the agglomerates.

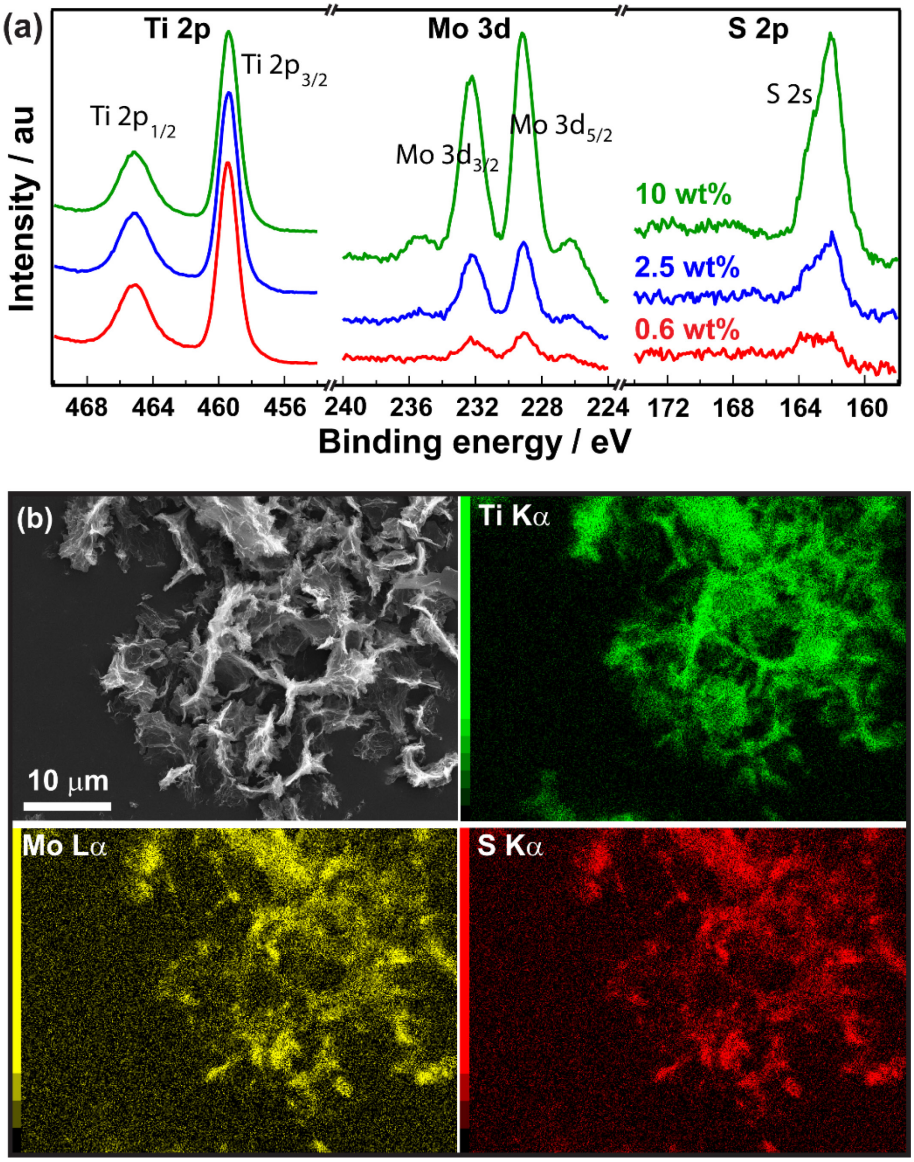

Figure 3.10. (a) XPS of the restacked flocculates for different $MoSs_2$ loadings. (b) EDS elemental map of the sample with 10 wt% MoS_2.

3.3.3. Theoretical Coverage: Stoichiometric and Structural Considerations

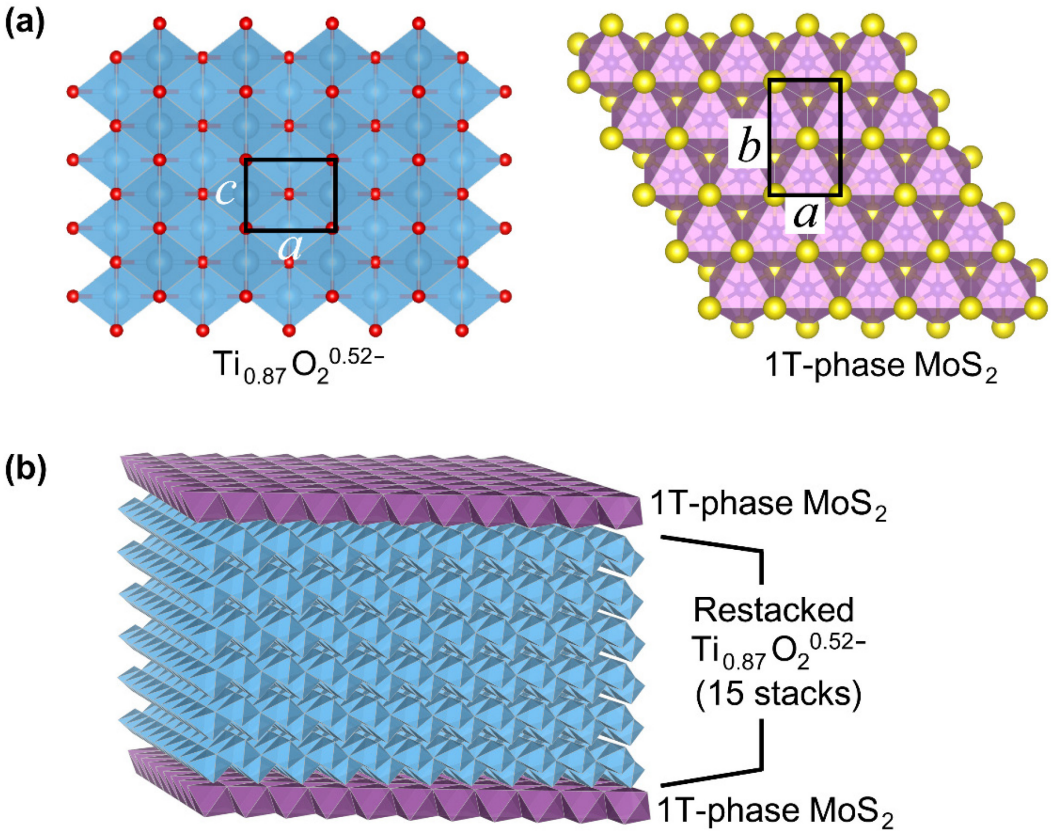

Figure 3.11. (a) In-plane structures of $Ti_{0.87}O_2^{0.52-}$ (a = 0.376 nm, c = 0.298 nm, Z = 2)[39] and 1T-phase MoS_2 (a = 0.320 nm, b = 0.569 nm, Z = 2; based on the 2D √3×1 rectangular superstructure). (b) Illustration of a 2D-heterointerface structure of restacked-$Ti_{0.87}O_2^{0.52-}$/MoS_2 consisting of 15 stacks of $Ti_{0.87}O_2^{0.52-}$ nanosheets as deduced from the TEM observation.

The ideal coverage and attachment feature of MoS_2 on restacked $Ti_{0.87}O_2^{0.52-}$ nanosheets are of importance to discuss from the stoichiometric and structural viewpoints. The information for the unit cell parameters is given in Figure 3.11a. Thus, the two-dimensional unit cell area of the $Ti_{0.87}O_2^{0.52-}$ nanosheets is 0.112 nm^2 (= 0.376 × 0.298) and that of the 1T-phase MoS_2 is 0.182 nm^2 (= 0.569 × 0.320). The 2D weight density of the nanosheets was calculated according to the following equation.

$$\rho_A = {[Z \times M_w]}/{[A_{2D} \times N_A]} \qquad (3.1)$$

where M_w, A_{2D}, N_A, and Z are the molecular weight, unit-cell area, Avogadro's number, and the number of molecules per area unit. Thus, the 2D weight densities were 2.185 × 10^{-3} and 2.922 × 10^{-3} g m^{-2} for

$Ti_{0.87}O_2^{0.52-}$ and MoS_2 nanosheets, respectively. The ideal monolayer coverage of MoS_2 at both surfaces of restacked $Ti_{0.87}O_2^{0.52-}$ nanosheets was achieved at an 18 wt% loading by assuming that the restacked nanosheets consisted of 15 nanosheet stacks (= [2 × 2.922]/[15 × 2.185]). However, careful consideration must be taken into account that the restacked flocculates further agglomerated to form secondary microstructures of restacked nanosheets. To this regard, it is possible to achieve monolayer coverage at a lower loading because the MoS_2 only attach on the surface of restacked $T_{0.87}O_2^{0.52-}$ nanosheets within the agglomerates.

3.3.4. Optical Properties

The addition of MoS_2 to a colloidal suspension of restacked flocculates of $T_{0.87}O_2^{0.52-}$ nanosheets yielded gradual color changes in the dried samples from pale yellow to dark greenish as the loading increased. Such gradual color changes provided further evidence of the attachment of MoS_2 nanosheets on restacked $T_{0.87}O_2^{0.52-}$ nanosheets and suggested the homogeneous distribution of the MoS_2 nanosheets. Such a feature could not be achieved with physical mixtures of the two independently flocculated nanosheets, where the individual aggregates were randomly distributed within the mixture (see Appendix 3, Figure A3.3). Thus, this result reveals the robust synthetic procedure of the two-step flocculation process for the fabrication of 2D-heterointerface structures of restacked-$T_{0.87}O_2^{0.52-}$/1T-phase MoS_2.

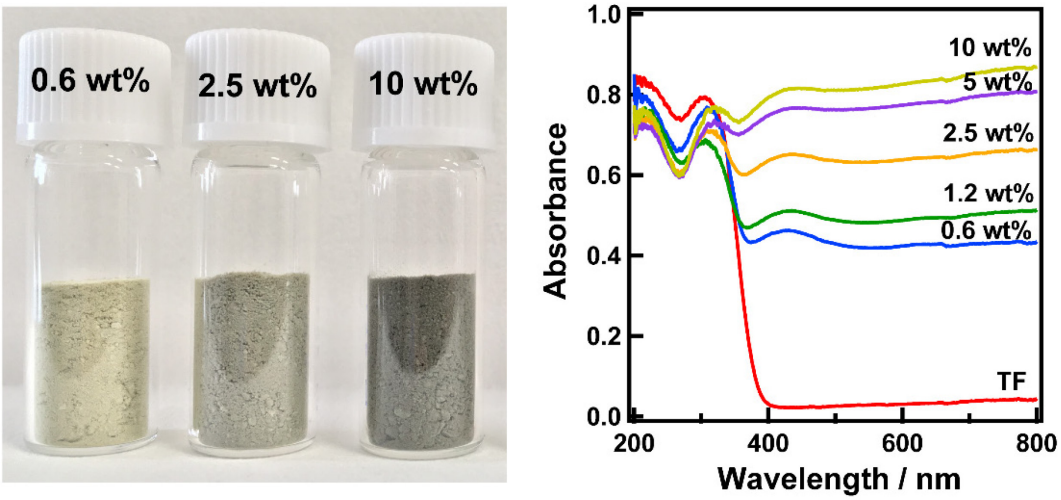

Figure 3.12. Photographs of restacked flocculates at different MoS_2 loadings (left). UV-visible diffuse reflectance of restacked flocculates (right).

The pure restacked $Ti_{0.87}O_2^{0.52-}$ nanosheets showed the most absorption in the UV region (Figure 3.12), which is a typical characteristic of a semiconducting material with an optical band gap of larger than 3 eV. The addition of MoS_2 resulted in a negligible change in the absorption features and absorbance intensities

in the UV region, which indicated that the samples absorbed similar numbers of photons in the given wavelength region. In contrast, the absorption in the visible region gradually increased with the MoS_2 loading, which was compatible with the color changes of the dried products. This feature was solely attributed to the absorption of visible light by metallic 1T MoS_2. Thus, we believe that the attachment of metallic 1T-phase MoS_2 on the surface of restacked $Ti_{0.87}O_2^{0.52-}$ does not change the electronic nature of the $Ti_{0.87}O_2^{0.52-}$ nanosheets.

3.3.5. BET Surface Area

The surface area and pore structure of a material are of particular importance in catalysis applications because they influence surface active sites and charge-carrier transport behavior. The effect of MoS_2 on the BET surface area and porosity of the restacked flocculates was examined using adsorption–desorption measurements. The samples demonstrated similar isotherm profiles regardless of the MoS_2 loadings (Figure 3.13a), which indicated that the samples shared a similar pore structure. According to the IUPAC classification,[40] the isotherm profiles were categorized as Type IV, which suggested the presence of mesopores. The shape of the hysteresis loops adopted that of type H3, indicating the characteristic of slit-shaped pores, which is consistent with the flocculation of 2D nanosheets. The addition of MoS_2 slightly reduced the BET surface area. Typically, the surface area decreased from ~40 $m^2 g^{-1}$ to ~32 $m^2 g^{-1}$ when the MoS_2 loading reached 10 wt% (Figure 3.13b). Thus, it is reasonable to assume that the introduction of MoS_2 insignificantly alters the surface area of the restacked products.

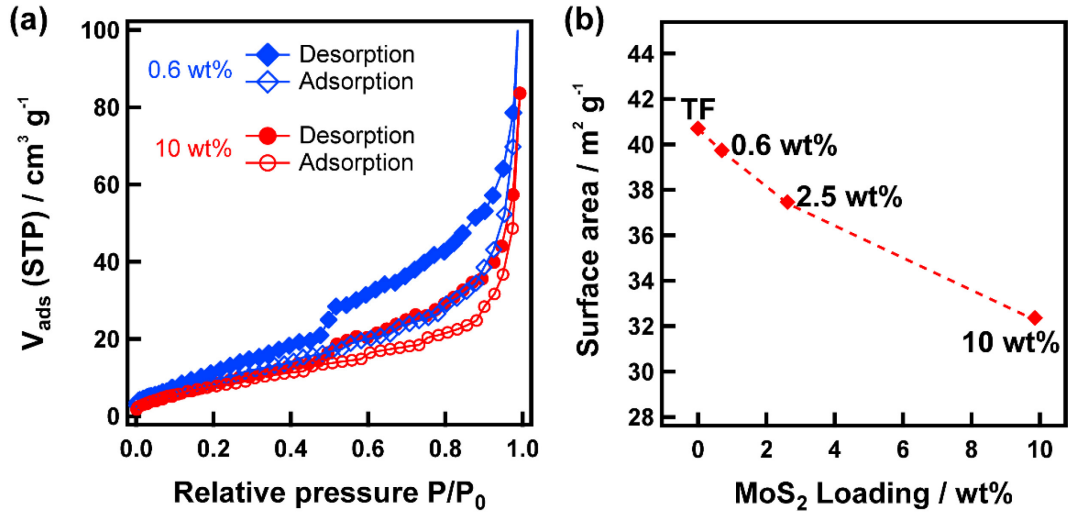

Figure 3.13. (a) Typical profiles of the adsorption-desorption isotherms of restacked flocculates. (b) BET surface area of the restacked flocculates as a function of MoS_2 loading.

3.3.6. Photocatalytic Activity

The photocatalytic activity of the 2D-heterointerface samples was examined for the H_2 evolution reaction under UV light irradiation from an aqueous methanol solution, where the methanol played the role as a sacrificial agent. The high surface area of the restacked $Ti_{0.87}O_2^{0.52-}$ modified with 1T-phase MoS_2 at the outer surface is expected to enhance the photocatalytic activity. Figure 3.14 displays the time course and rate of evolved H_2 gas as a function of irradiation time. The rate of H_2 generation for the restacked $Ti_{0.87}O_2^{0.52-}$ alone (TF sample) was ~0.15 mmol g^{-1} h^{-1}, which was larger than that of commercial P25 nanoparticles (~0.09 mmol g^{-1} h^{-1}). Upon the modification with 1T-phase MoS_2 nanosheets, the photocatalytic activity was remarkably enhanced, as expected. The highest activity of ~1.2 mmol g^{-1} h^{-1} was achieved at a MoS_2 loading of 2.5 wt%, and was approximately one order of magnitude higher than that of restacked $Ti_{0.87}O_2^{0.52-}$ alone or that of P25 nanoparticles. However, the photocatalytic activity gradually decreased upon further loading of MoS_2 (5 wt% and above). In contrast, the restacked 1T-phase MoS_2 alone (MF sample) did not show any photocatalytic activity for H_2 evolution, suggesting that the 1T-phase MoS_2 behaves only as a co-catalyst.

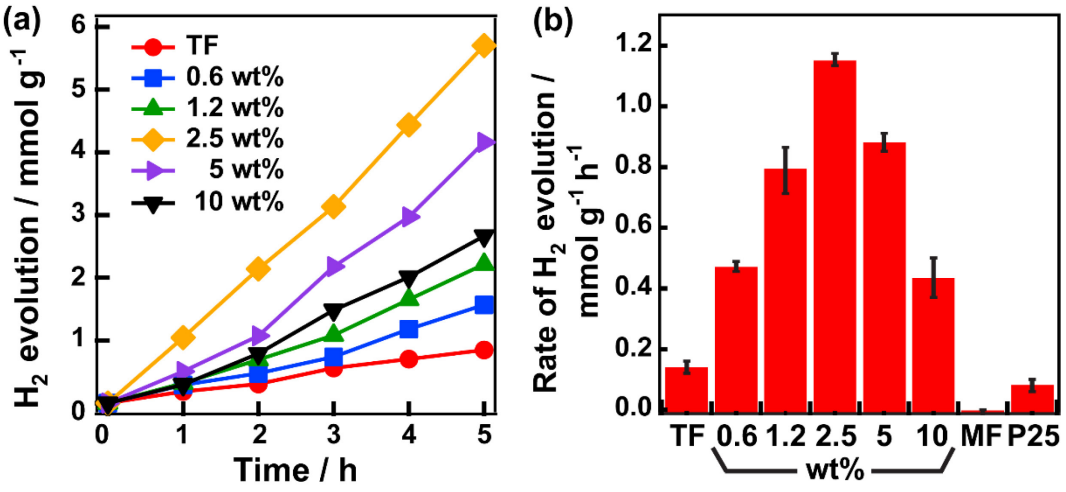

Figure 3.14. (a) Time course and (b) rate of photocatalytic H_2 evolution over samples at different MoS_2 loadings. TF and MF are flocculated $Ti_{0.87}O_2^{0.52-}$ and 1T-phase MoS_2 alone, respectively.

The enhancement of the photocatalytic activity of the 2D-heterointerface samples can be understood based on the interfacial-coupling effect of the restacked $Ti_{0.87}O_2^{0.52-}$ with 1T-phase MoS_2, where 1T-phase MoS_2 may work as an electron transfer mediator. This hypothesis is reasonable, as supported by the difference in the energy levels of each component (Figure 3.15). The work function of 1T-phase MoS_2 has been estimated as ~4.2 eV vs vacuum (–0.24 V vs NHE).[41–43] It has been shown that the position of the conduction band edge of $Ti_{0.91}O_2^{0.36-}$ nanosheets is –0.78 vs NHE,[28] which is more negative than the fermi level of 1T-phase MoS_2. Thus, photogenerated electrons in the conduction band of the $Ti_{0.87}O_2^{0.52-}$ nanosheets can be transferred to the 1T-phase MoS_2 layer, facilitating the efficient separation of

photogenerated carriers in the $Ti_{0.87}O_2^{0.52-}$ nanosheets. Eventually, the electrons injected to the 1T-phase MoS_2 can be efficiently utilized for the hydrogen evolution reaction thanks to its catalytic nature, *i.e.,* the excellent electrical conductivity and the abundant catalytically active sites.

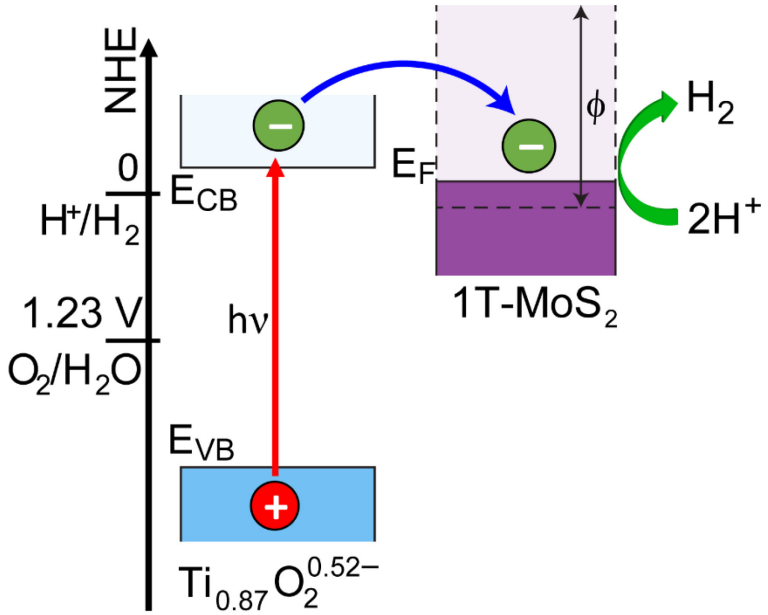

Figure 3.15. Schematic energy-level diagrams of $Ti_{0.87}O_2^{0.52-}$ and 1T-phase MoS_2 for comparison with the potentials for water reduction and oxidation.

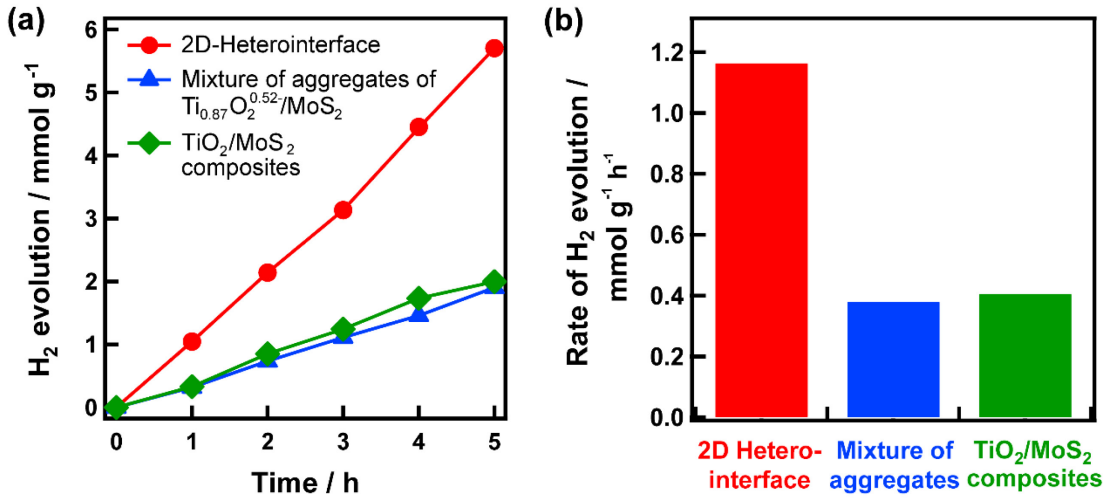

Figure 3.16. (a) Time course and (b) rate of photocatalytic H_2 evolution over control samples from physical mixture of bulk aggregates of independently flocculated $Ti_{0.87}O_2^{0.52-}/MoS_2$ nanosheets and composites of P25-nanoparticles/MoS_2, in comparison to the 2D-heterointerface sample.

Note that in the present case we may neglect the possibility of a significant contribution of the optical absorption and surface area to the enhancement of the photocatalytic activity. As discussed in sub-section 3.3.4, the samples typically showed similar absorption features in the UV region. Although there was a gradual increase in absorbance in the visible region with the MoS_2 loading, this should not affect the photocatalytic activity. This assumption was confirmed from the test performed under white light (λ = 400–800 nm), which showed negligible H_2 production. Meanwhile, the surface area of the samples only slightly decreased with the MoS_2 loading (sub-section 3.3.5), which should not contribute to the enhancement of the photocatalytic activity.

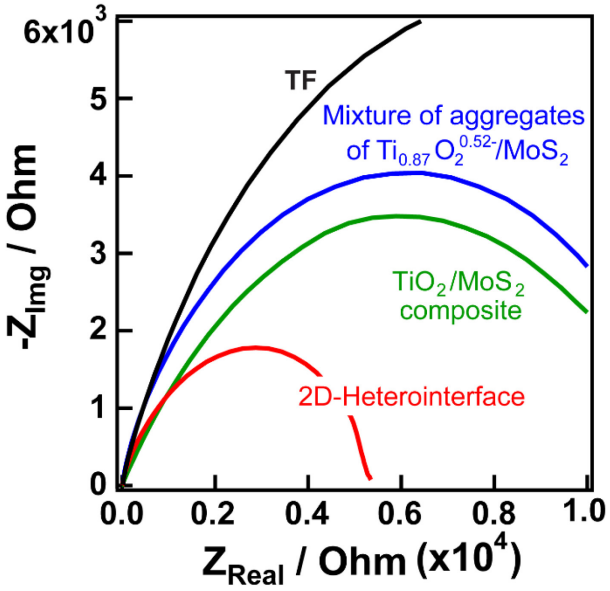

Figure 3.17. EIS Nyquist plots measured in the dark. TF is flocculated $Ti_{0.87}O_2^{0.52-}$ alone.

To further confirm the influence of the interfacial-coupling between $Ti_{0.87}O_2^{0.52-}$ and MoS_2 to the enhanced activity in the 2D-heterointerface samples, we compared the photocatalytic activity with those of control samples from physical mixtures of bulk aggregates of individually flocculated $Ti_{0.87}O_2^{0.52-}$/MoS_2 nanosheets and composites of TiO_2(P25)-nanoparticles/MoS_2 under the same experimental conditions (see the details of the sample preparation in Appendix 3). The photocatalytic activities of the former and the latter samples were ~0.38 and ~0.4 mmol h^{-1} g^{-1} (Figure 3.16), respectively. These values were approximately three times lower than that of the 2D-heterointerface samples. The lower photocatalytic activity might be attributed to a poor or insufficient interfacial interaction between the bulk aggregates of independently flocculated $Ti_{0.87}O_2^{0.52-}$ and MoS_2 nanosheets. In other words, bulk-scale morphology prevents molecular-level intimate contact between the two nanosheets. In contrast, the use of TiO_2 nanoparticles also failed to yield sufficient interfacial contact with MoS_2 co-catalyst, since only small portions of the curvature of the nanoparticles are expected to attach on the MoS_2 nanosheets. As a result, the probability of charge recombination might increase due to the rather slow injection of electrons to the

MoS_2 layers, which would eventually lead to the lower photocatalytic activity. Hence, this comparison clearly underlines the merits of the extensive interfacial coupling of 2D nanosheets for facilitating fast interfacial charge transfer from $Ti_{0.87}O_2^{0.52-}$ nanosheets to 1T-phase MoS_2, which definitely cannot be attained with their nanoparticle or bulk-scale counterparts. This conclusion is in agreement with the EIS Nyquist plots (Figure 3.17), that revealed a smaller semicircular shape for the 2D-heterointerface sample, indicating a lower charge transfer resistance from $Ti_{0.87}O_2^{0.52-}$ nanosheets to 1T-phase MoS_2.

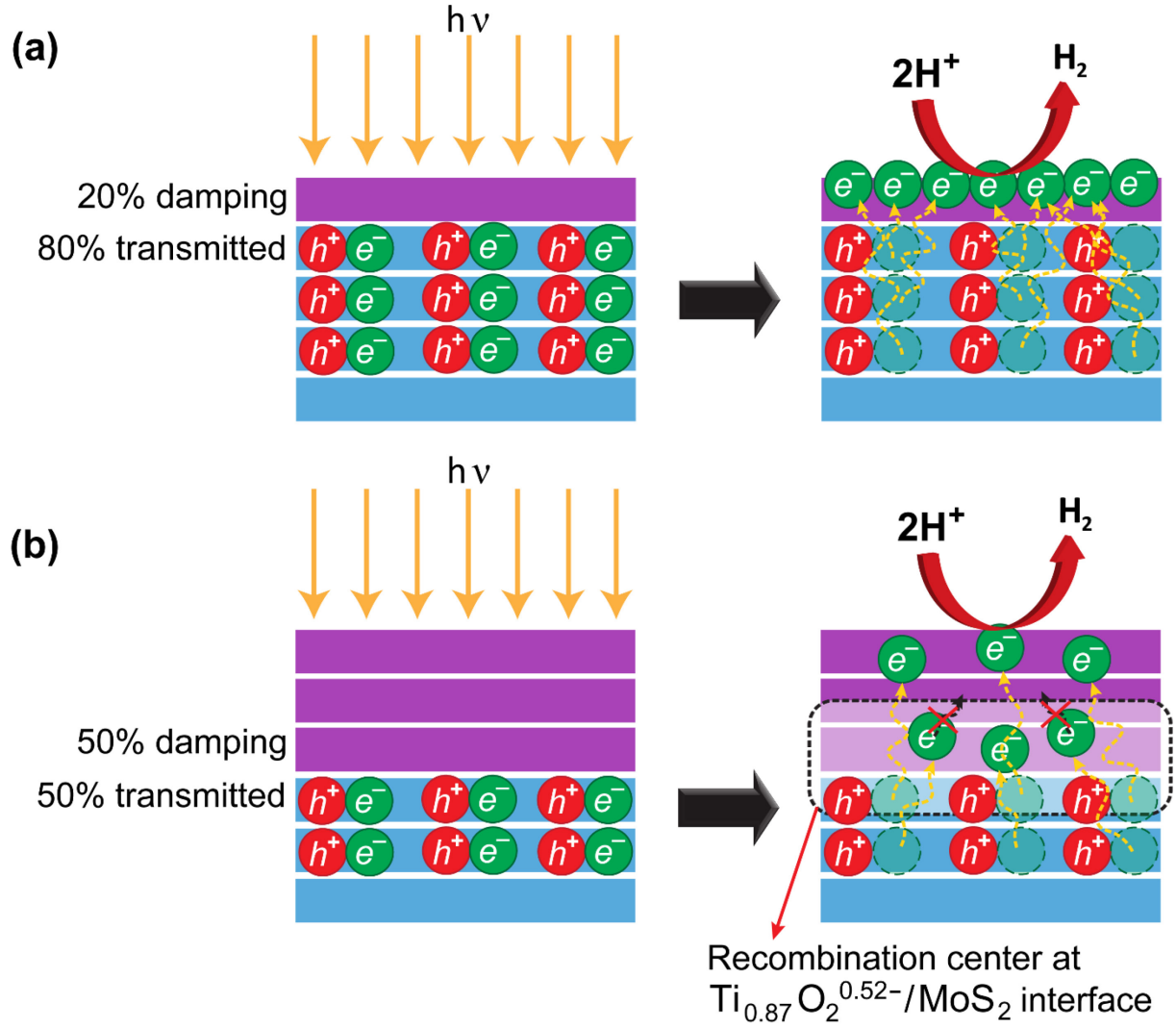

Figure 3.18. Schematic diagram for how the attachment feature affects the photocatalytic activity.

As discussed in sub-section 3.3.3, the ideal monolayer coverage of MoS_2 could be achieved at a theoretical loading of 18 wt% with the assumption that the MoS_2 nanosheets attached to the surface of 15-layered stacks of $Ti_{0.87}O_2^{0.52-}$ nanosheets. Below this amount, an enhancement of the photocatalytic activity is expected with the addition of MoS_2 nanosheets. However, this consideration is outwardly inconsistent with the photocatalytic results, which showed decreased activity at MoS_2 loadings of 5 wt% and above. In

theory, this amount provides sub-monolayer coverage of ~28% with only a ~5% damping of incident light intensity; monolayer MoS_2 shows an absorbance of ~0.1 at λ = 400 nm, which is equivalent to a ~20% damping of the incident light intensity.[44] Thus, this may suggest that the MoS_2 nanosheets were attached as multilayer crystallites above a 5 wt% loading, which provides a plausible explanation for the reduced activity.

In general, co-catalysts are deposited on photocatalysts as a thick and dense body, making the photocatalysts inactive due to light blockade. To this regard, the single-layer attachment of an MoS_2 co-catalyst can be considered as the most desired feature to enhancing the photocatalytic activity (Figure 3.18a), as it provides a low shielding effect for better light harvesting in the restacked $Ti_{0.87}O_2^{0.52-}$. Since the monolayer MoS_2 only results in a ~20% damping of the incident light intensity, the restacked $Ti_{0.87}O_2^{0.52-}$ nanosheets beneath the MoS_2 can still work. In addition, the monolayer feature is beneficial for efficient electron migration from the $Ti_{0.87}O_2^{0.52-}$ nanosheets to the MoS_2 surface, where the charges are eventually utilized for the proton (H^+) reduction reaction into H_2. If multilayer crystallite MoS_2 as the cocatalyst is attached on the $Ti_{0.87}O_2^{0.52-}$ surface, the transmitted light intensity beneath the MoS_2 should be reduced by ~37 and ~50% for the attachment of bilayer and trilayer MoS_2 nanosheets, respectively.[44] Such a considerable damping of the light intensity should significantly reduce the number of photocatalytic active sites beneath the MoS_2 (Figure 3.18b). Consequently, the number of photogenerated electron-hole pairs should also reduce. In addition, the electrons would need to hop the interlayer gaps to reach the top-most surface of the MoS_2 multilayers. It is known that interlayer hopping is sluggish[45] because the electrical resistivity of MoS_2 across different layers has been reported to be ~2000 times higher than that within the layer,[46] which leads to a higher probability for the recombination of photogenerated carriers at the $Ti_{0.87}O_2^{0.52-}/MoS_2$ interface. In this case, besides the reduced number of photogenerated carriers, the decrease in the photocatalytic activity at further co-catalyst loadings should be instead attributed to the decreasing rate for catalytic reactions occurring at the co-catalyst/liquid interface.[47–49] This suggests that an optimum loading of MoS_2 co-catalyst is essential to achieve the unilamellar attachment as the important key factor for enhancing the photocatalytic activity.

3.4. Summary

A new class of photocatalyst materials was successfully constructed from the monolayer modification of restacked $Ti_{0.87}O_2^{0.52-}$ nanosheets with metallic 1T-phase MoS_2 *via* a two-step-flocculation. Such a modification was controlled by the difference in the minimum critical concentration of protons required for inducing flocculation on the respective nanosheets, enabling the monolayer attachment of MoS_2 nanosheets on the restacked $Ti_{0.87}O_2^{0.52-}$. The MoS_2-modified restacked-$Ti_{0.87}O_2^{0.52-}$ showed a highly enhanced photocatalytic activity for hydrogen evolution from an aqueous methanol solution. The rate of hydrogen generation was enhanced by about 10 times higher over those of the restacked $Ti_{0.87}O_2^{0.52-}$ alone and P25 nanoparticles. In addition, the activity was also superior to those of control samples from the physical

mixtures of bulk aggregates of independently flocculated $Ti_{0.87}O_2^{0.52-}$/MoS_2 nanosheets and the composites of P25-nanoparticles/MoS_2, emphasizing the significant importance of molecular-level interfacial hybridization of 2D nanomaterials. Our strategy provides a facile and robust route for fabricating such a 2D-heterointerfaces, which is beneficial for large scale production due to its solution processability. We believe that this approach can be exploited for a range of applications, not only for (photo)catalysis but also for optoelectronics and energy storage.

3.5. References and Notes

[1] A. Paracchino, V. Laporte, K. Sivula, M. Grätzel, E. Thimsen, *Nat. Mater.* **2011**, *10*, 456–461.

[2] Y. Hou, B. L. Abrams, P. C. K. Vesborg, M. E. Björketun, K. Herbst, L. Bech, A. M. Setti, C. D. Damsgaard, T. Pedersen, O. Hansen, et al., *Nat. Mater.* **2011**, *10*, 434–8.

[3] A. Fujishima, K. Honda, *Nature* **1972**, *238*, 37–38.

[4] G. Wang, H. Wang, Y. Ling, Y. Tang, X. Yang, R. C. Fitzmorris, C. Wang, J. Z. Zhang, Y. Li, *Nano Lett.* **2011**, *11*, 3026–3033.

[5] A. J. Nozik, *Nature* **1975**, *257*, 383–386.

[6] S. Hoang, S. Guo, N. T. Hahn, A. J. Bard, C. B. Mullins, *Nano Lett.* **2012**, *12*, 26–32.

[7] J. Nowotny, C. C. Sorrell, L. R. Sheppard, T. Bak, *Int. J. Hydrogen Energy* **2005**, *30*, 521–544.

[8] Y. Ma, X. Wang, Y. Jia, X. Chen, H. Han, C. Li, *Chem. Rev.* **2014**, *114*, 9987–10043.

[9] S. Kundu, A. Patra, *Chem. Rev.* **2017**, *117*, 712–757.

[10] F. E. Osterloh, *Chem. Soc. Rev.* **2013**, *42*, 2294–2320.

[11] H. Tong, S. Ouyang, Y. Bi, N. Umezawa, M. Oshikiri, J. Ye, *Adv. Mater.* **2012**, *24*, 229–251.

[12] J. Yang, D. Wang, H. Han, C. Li, *Acc. Chem. Res.* **2013**, *46*, 1900–1909.

[13] W. Peng, Y. Li, F. Zhang, G. Zhang, X. Fan, *Ind. Eng. Chem. Res.* **2017**, *56*, 4611–4626.

[14] K. Chang, Z. Mei, T. Wang, Q. Kang, S. Ouyang, J. Ye, *ACS Nano* **2014**, *8*, 7078–7087.

[15] J. Ran, J. Zhang, J. Yu, M. Jaroniec, S. Z. Qiao, *Chem. Soc. Rev.* **2014**, *43*, 7787–7812.

[16] S. K. Dutta, S. K. Mehetor, N. Pradhan, *J. Phys. Chem. Lett.* **2015**, *6*, 936–944.

[17] S. Bai, W. Yin, L. Wang, Z. Li, Y. Xiong, *RSC Adv.* **2016**, *6*, 57446–57463.

[18] J. Low, J. Yu, M. Jaroniec, S. Wageh, A. A. Al-Ghamdi, *Adv. Mater.* **2017**, *29*, 1601694.

[19] J. K. Wassei, R. B. Kaner, *Acc. Chem. Res.* **2013**, *46*, 2244–2253.

[20] X. Huang, Z. Zeng, H. Zhang, *Chem. Soc. Rev.* **2013**, *42*, 1934–46.

[21] S. Ida, T. Ishihara, *J. Phys. Chem. Lett.* **2014**, *5*, 2533–2542.

[22] L. Wang, T. Sasaki, *Chem. Rev.* **2014**, *114*, 9455–9486.

[23] R. Ma, T. Sasaki, *Acc. Chem. Res.* **2015**, *48*, 136–143.

[24] X. Zhang, Z. Lai, C. Tan, H. Zhang, *Angew. Chem. Int. Ed.* **2016**, *55*, 8816–8838.

[25] C. Tan, X. Cao, X.-J. Wu, Q. He, J. Yang, X. Zhang, J. Chen, W. Zhao, S. Han, G.-H. Nam, et al., *Chem. Rev.* **2017**, *117*, 6225–6331.

[26] J. Low, S. Cao, J. Yu, S. Wageh, *Chem. Commun.* **2014**, *50*, 10768.

[27] T. Sasaki, M. Watanabe, *J. Phys. Chem. B* **1997**, *101*, 10159–10161.

[28] N. Sakai, Y. Ebina, K. Takada, T. Sasaki, *J. Am. Chem. Soc.* **2004**, *126*, 5851–5858.

[29] U. Maitra, U. Gupta, M. De, R. Datta, A. Govindaraj, C. N. R. Rao, *Angew. Chem. Int. Ed.* **2013**, *52*, 13057–13061.

[30] G. Eda, H. Yamaguchi, D. Voiry, T. Fujita, M. Chen, M. Chhowalla, *Nano Lett.* **2011**, *11*, 5111–5116.

[31] Q. Ding, F. Meng, C. R. English, M. Cabán-Acevedo, M. J. Shearer, D. Liang, A. S. Daniel, R. J. Hamers, S. Jin, *J. Am. Chem. Soc.* **2014**, *136*, 8504–8507.

[32] Y. Li, H. Wang, L. Xie, Y. Liang, G. Hong, H. Dai, *J. Am. Chem. Soc.* **2011**, *133*, 7296–7299.

[33] M. A. Lukowski, A. S. Daniel, F. Meng, A. Forticaux, L. Li, S. Jin, *J. Am. Chem. Soc.* **2013**, *135*, 10274–10277.

[34] D. Voiry, M. Salehi, R. Silva, T. Fujita, M. Chen, T. Asefa, V. B. Shenoy, G. Eda, M. Chhowalla, *Nano Lett.* **2013**, *13*, 6222–6227.

[35] J. Israelachvili, *Intermolecular and Surface Forces*, Academic Press, New York, **1991**.

[36] N. I. Lebovka, *Adv. Polym. Sci.* **2014**, *255*, 57–96.

[37] D. H. Everett, *Basic Principles of Colloid Science*, Royal Society Of Chemistry, Cambridge, **1988**.

[38] J. Heising, M. G. Kanatzidis, *J. Am. Chem. Soc.* **1999**, *121*, 11720–11732.

[39] L. Li, R. Ma, Y. Ebina, K. Fukuda, K. Takada, T. Sasaki, *J. Am. Chem. Soc.* **2007**, *129*, 8000–8007.

[40] K. S. W. Sing, *Pure Appl. Chem.* **1985**, *57*, 603–619.

[41] P. Du, Y. Zhu, J. Zhang, D. Xu, W. Peng, G. Zhang, F. Zhang, X. Fan, *RSC Adv.* **2016**, *6*, 74394–74399.

[42] B. Mahler, V. Hoepfner, K. Liao, G. A. Ozin, *J. Am. Chem. Soc.* **2014**, *136*, 14121–14127.

[43] K. Chang, X. Hai, H. Pang, H. Zhang, L. Shi, G. Liu, H. Liu, G. Zhao, M. Li, J. Ye, *Adv. Mater.* **2016**, *28*, 10033–10041.

[44] In principle, one cannot define a macroscopic optical-absorption coefficient in the normal direction for a monolayer MoS_2, since the magnitude should be averaged over several unit cells at the macroscopic scale. Nevertheless, the equivalent optical-absorption coefficient, α, for monolayer MoS_2 can be estimated from Beer–Lambert's law as $\alpha = A/(0.434 \times z) = 3.6 \times 10^6$ cm^{-1} at λ=400 nm, where the variable A is the absorbance and z is the thickness of single-layer MoS_2 nanosheet (=0.65 nm). Thus, the intensity of light, transmitted into restacked $Ti_{0.87}O_2^{0.52-}$, should be reduced to an exponential factor of $-(\alpha z)n = -0.23n$, where n is the number of layers of the MoS_2 nanosheets.

[45] Y. Yu, S.-Y. Huang, Y. Li, S. N. Steinmann, W. Yang, L. Cao, *Nano Lett.* **2014**, *14*, 553–558.

[46] H. Tributsch, *Berichte der Bunsen-Gesellschaft für Phys. Chemie* **1977**, *81*, 361–369.

[47] V. Subramanian, E. E. Wolf, P. V. Kamat, *J. Am. Chem. Soc.* **2004**, *126*, 4943–4950.

[48] P. V. Kamat, *J. Phys. Chem. Lett.* **2012**, *3*, 663–672.

[49] Y. Ben-Shahar, F. Scotognella, I. Kriegel, L. Moretti, G. Cerullo, E. Rabani, U. Banin, *Nat. Commun.* **2016**, *7*, 10413.

Chapter 4.
Summary and Outlook

4.1. Summary

The work described in this thesis is aimed to examine the nature of chemically exfoliated MoS_2 nanosheets in aqueous suspensions and their potential application as a building block for the development of a new class of photocatalyst materials *via* the hetero-assembly with $Ti_{1-\delta}O_2^{4\delta-}$ nanosheets. The main and important results described in this thesis can be summarized as follows.

1. Although the preparation of MoS_2 nanosheets *via* chemical exfoliation has been established since three decades ago, insights into the underlying mechanism, production of high-quality nanosheets, and long-term stability were limited. Detailed investigations into these aspects were carried out to provide a deeper understanding of the intrinsic nature and characteristics of chemically exfoliated MoS_2, as well as to identify and elaborate the factors influencing the stability and quality of the nanosheets. The suspension stability and nanosheet quality of chemically exfoliated MoS_2 were strongly influenced by the reoxidation process. To this regard, the atmospheric composition had a determining role in controlling and maintaining the stability and quality of the nanosheets. The reoxidation process led to the deterioration of the nanosheets, where the nanosheets were broken into laterally fractured small fragments, followed by aggregation upon prolonged aging. The XRD study of the restacked nanosheets suggested that the nanosheets were reoxidized sheet by sheet and the oxidation states of the sheets should be discrete only at two values of Mo^{4+} and $Mo^{(4-\delta)+}$. Upon reoxidation, the nanosheets exhibited metastable structures of neutral 1T MoS_2. Storing the nanosheet in an inert atmosphere could effectively preserve the stability and quality of the nanosheets and suppress the reoxidation process.

2. To overcome limitations of particle-based heterointerfaces of photocatalyst materials, where co-catalysts are typically impregnated as a thick and dense body, 2D nanomaterials were utilized to construct specially designed nanostructured hybrid materials. A new class of photocatalyst materials was successfully constructed from the monolayer attachment of a metallic 1T-phase MoS_2 co-catalyst on restacked $Ti_{0.87}O_2^{0.52-}$ nanosheets *via* a two-step flocculation of their colloidal suspensions, where the $Ti_{0.87}O_2^{0.52-}$ and metallic 1T-phase MoS_2 nanosheets were employed as the photoactive material and co-catalyst, respectively. The acid concentration in the solution played a key role in controlling the attachment of the MoS_2 nanosheets on the restacked $Ti_{0.87}O_2^{0.52-}$. The MoS_2-modified restacked-$Ti_{0.87}O_2^{0.52-}$ exhibited a highly efficient photocatalytic activity for hydrogen generation from an aqueous methanol solution. A maximum evolution rate of approximately 1.2 mmol h^{-1} g^{-1} was

achieved at an optimum MoS_2 loading of 2.5 wt%. The activity was three times higher than those of the control samples from physical mixtures of bulk aggregates of independently flocculated $Ti_{0.87}O_2^{0.52-}$/MoS_2 nanosheets and the composites of P25-nanoparticles/MoS_2. Clearly, these results emphasize the significant importance of molecular-level interfacial hybridization of 2D nanomaterials, which cannot be achieved with a system fabricated from the nanoparticle or bulk-scale counterparts.

4.2. Outlook

The hetero-assembly of two different types of 2D nanomaterials, which utilizes the coupling effect achieved by their intimate interfacial interaction, has appeared as an attractive strategy to develop new and unique artificial materials and systems. So far, the most studied MoS_2-based 2D heterostructures have been limited to graphene or other TMD materials. In contrast, the hetero-assembly of MoS_2 with oxide or hydroxide nanosheets remain underexplored. Various oxide and hydroxide nanosheets has been successfully synthesized[1–3] and studied for a range of applications from electronics/dielectrics (mainly oxide nanosheets)[4–9] to energy storage and catalysis (some oxide and hydroxide nanosheets).[10–15] The integration of MoS_2 with oxide/hydroxide nanosheets may open an avenue to explore new or enhanced functionalities. Recently, a superlattice-like hetero-assembly of metallic 1T-phase MoS_2 and r-GO was reported for efficient sodium storage and hydrogen evolution.[16] Following this direction, the superlattice-like hetero-assembly of metallic 1T-phase MoS_2 and layered double hydroxide (LDH) nanosheets may show an enhanced performance for use in supercapacitors and electrocatalytic H_2/O_2 evolution. The insertion of monolayer 1T-phase MoS_2 in LDH stacks may increase the interfacial charge transfer within the systems, which would lead to better electron transport. In light of this possible benefit, the superlattice-like heterostructure of 1T-MoS_2/LDH may also show an intriguing function in biosensing applications. Although LDHs are insulators, they possess excellent biocompatibility, high charge density, and good adsorption selectivity for some biomolecules and proteins.[17–20] Since MoS_2 nanosheets exhibit a potential application in FET devices,[21–23] the hetero-assembly of MoS_2 and redox-active oxide nanosheets (such as $MnO_2^{\delta-}$ nanosheets) may show an attractive electrochemical biosensing activity by fabricating FET-based electrochemical biosensors.[17,23–25]

4.3. References

[1] R. Ma, T. Sasaki, *Adv. Mater.* **2010**, *22*, 5082–5104.

[2] Q. Wang, D. O'Hare, *Chem. Rev.* **2012**, *112*, 4124–4155.

[3] R. Ma, T. Sasaki, *Acc. Chem. Res.* **2015**, *48*, 136–143.

[4] M. Osada, Y. Ebina, K. Fukuda, K. Ono, K. Takada, K. Yamaura, E. Takayama-Muromachi, T. Sasaki, *Phys. Rev. B* **2006**, *73*, 2–5.

[5] M. Osada, Y. Ebina, H. Funakubo, S. Yokoyama, T. Kiguchi, K. Takada, T. Sasaki, *Adv. Mater.* **2006**, *18*, 1023–1027.

[6] M. Osada, Y. Ebina, K. Takada, T. Sasaki, *Adv. Mater.* **2006**, *18*, 295–299.

[7] M. Osada, K. Akatsuka, Y. Ebina, H. Funakubo, K. Ono, K. Takada, T. Sasaki, *ACS Nano* **2010**, *4*, 5225–5232.

[8] M. Osada, G. Takanashi, B. W. Li, K. Akatsuka, Y. Ebina, K. Ono, H. Funakubo, K. Takada, T. Sasaki, *Adv. Funct. Mater.* **2011**, *21*, 3482–3487.

[9] B. Li, M. Osada, T. C. Ozawa, T. Sasaki, *Chem. Mater.* **2012**, *24*, 3111–3113.

[10] J. E. ten Elshof, H. Yuan, P. Gonzalez Rodriguez, *Adv. Energy Mater.* **2016**, *6*, 1600355.

[11] X. Li, D. Du, Y. Zhang, W. Xing, Q. Xue, Z. Yan, *J. Mater. Chem. A* **2017**, *5*, 15460–15485.

[12] R. Subbaraman, D. Tripkovic, K.-C. Chang, D. Strmcnik, A. P. Paulikas, P. Hirunsit, M. Chan, J. Greeley, V. Stamenkovic, N. M. Markovic, *Nat. Mater.* **2012**, *11*, 550–557.

[13] P. Xiong, R. Ma, N. Sakai, X. Bai, S. Li, T. Sasaki, *ACS Appl. Mater. Interfaces* **2017**, *9*, 6282–6291.

[14] R. Ma, X. Liu, J. Liang, Y. Bando, T. Sasaki, *Adv. Mater.* **2014**, *26*, 4173–4178.

[15] W. Ma, R. Ma, J. Wu, P. Sun, X. Liu, K. Zhou, T. Sasaki, *Nanoscale* **2016**, *8*, 10425–10432.

[16] P. Xiong, R. Ma, N. Sakai, L. Nurdiwijayanto, T. Sasaki, *ACS Energy Lett.* **2018**, *3*, 997–1005.

[17] D. Chimene, D. L. Alge, A. K. Gaharwar, *Adv. Mater.* **2015**, *27*, 7261–7284.

[18] R. Kurapati, K. Kostarelos, M. Prato, A. Bianco, *Adv. Mater.* **2016**, *28*, 6052–6074.

[19] W. Sun, Y. Guo, Y. Lu, A. Hu, F. Shi, T. Li, Z. Sun, *Electrochim. Acta* **2013**, *91*, 130–136.

[20] L.-M. Liu, L.-P. Jiang, F. Liu, G.-Y. Lu, E. S. Abdel-Halim, J.-J. Zhu, *Anal. Methods* **2013**, *5*, 3565.

[21] B. Radisavljevic, A. Radenovic, J. Brivio, V. Giacometti, A. Kis, *Nat. Nanotechnol.* **2011**, *6*, 147–150.

[22] R. Yang, Z. Wang, P. X.-L. Feng, *Nanoscale* **2014**, *6*, 12383–12390.

[23] D. Sarkar, W. Liu, X. Xie, A. C. Anselmo, S. Mitragotri, K. Banerjee, *ACS Nano* **2014**, *8*, 3992–4003.

[24] X. Li, J. Shan, W. Zhang, S. Su, L. Yuwen, L. Wang, *Small* **2017**, *13*, 1602660.

[25] Y. Yuan, S. Wu, F. Shu, Z. Liu, *Chem. Commun.* **2014**, *50*, 1095–1097.

Appendix 1.
Preparation of MoS_2 Nanosheets *via* the Chemical Exfoliation Method

This chapter is devoted to describe the preparation of MoS_2 nanosheets *via* a chemical exfoliation method used throughout the research. The detailed procedures on the preparation and the characterization of the nanosheets are presented.

A1.1. Chemical Exfoliation of MoS_2 Nanosheets

A1.1.1. Pre-expansion of MoS_2 Crystals

Bulk MoS_2 crystals were subjected to a pre-expansion treatment according to a modification of the previously reported procedure.[1] Approximately 1-2 g of MoS_2 crystals were treated by refluxing in 100 cm^{-3} N_2H_4 at 130 °C for 24 h. Shortly, the crystals expanded voluminously by approximately 100 times compared to their original volume. The expanded crystals were then filtrated, washed with water and ethanol, and dried at 120 °C overnight.

A1.1.2. Li Intercalation and Exfoliation

The chemical exfoliation of MoS_2 crystals was carried out according to a procedure from a previous report.[2] The pre-expanded crystals were lithiated by reacting with a 2.5-fold molar excess of a *n*-butyllithium solution (1.6 M in hexane) for 5 days in an Ar-filled dry box. The lithiated crystals, Li_xMoS_2, were then recovered by filtration. Washing with *n*-hexane was needed to remove the excess lithium and organic residues. Exfoliation was achieved by immediately treating the Li_xMoS_2 crystals with water and ultrasonication for 1 h. The mixture was then centrifuged at 2000 rpm to separate the unexfoliated crystals. The top supernatant was sedimented by centrifugation at 12,000 rpm, followed by re-dispersion in water.

A1.1.3. Determining and Controlling the Li Content

The Li content of the suspension was determined using a Li-ion selective electrode with a Mettler Toledo DX207-Li. The Li content of the suspension was re-adjusted by adding a specific amount of a LiOH solution.

A1.2. Characterization

The structures of the MoS_2 crystal upon the pre-expansion treatment and the lithiated product were examined using powder XRD analysis with a Rigaku Rint ULTIMA IV diffractometer. SEM images of the MoS_2

crystals was obtained using a JEOL JSM-6010LA. The morphology, lateral size, and thickness of the exfoliated nanosheets were examined with a Hitachi SPA 400 AFM. TEM images and SAED patterns were obtained using a JEOL JEM-3000F. UV-visible spectra of the suspensions and the monolayer film were measured with a Hitachi U-4100 spectrophotometer. The ICP-OES measurement was carried out using a Hitachi High-Tech SPS3520UV-DD. The samples were dissolved in a mixture of sodium hydroxide and bromine solution. The subsequent addition of nitric acid under continuous heating was applied to remove the bromine. Then, the solution was diluted with water before the measurement. The Li content of the suspension was determined using a Mettler Toledo Li-ion selective electrode DX207-Li.

A1.3. Results

A.1.3.1. Pre-expansion Treatment and Li intercalation

Bulk MoS_2 crystals were pre-expanded by treating with hydrazine (N_2H_4) at 130 °C for 24 h under a refluxing condition. Clearly, the MoS_2 crystals were massively expanded (Figure A1.1). Zheng *et al.*[1] suggested that the expansion mechanism of MoS_2 crystals proceeds upon intercalation of $N_2H_5^+$ (oxidized form of N_2H_4) into MoS_2 layers. The $N_2H_5^+$ will decompose to N_2, NH_3 and H_2 gases upon heating at high temperature. Such a process expands the MoS_2 sheets by >100 times from the original volume. The XRD analysis indicated that the pristine structure the MoS_2 crystals remained unchanged after the pre-expansion (Figure A1.2). Morphological differences were hardly observed after the pre-expansion treatment (Figure A1.3). The expansion treatment created cracks and spaces, which is beneficial for facilitating Li intercalation. After Li intercalation, the interlayer spacing of MoS_2 increased from 0.612 to 0.635 nm (Figure A1.4).

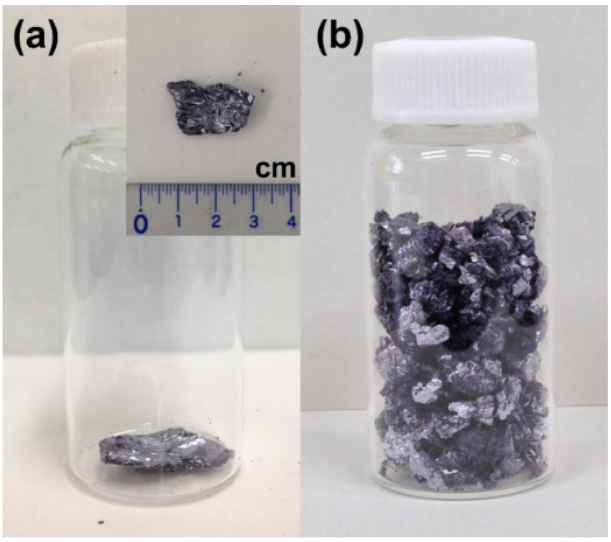

Figure A1.1. (a) Photographs of a piece of bulk MoS_2 crystals before pre-expansion. The initial size is ~2×1 cm. (b) MoS_2 crystals after pre-expansion treatment.

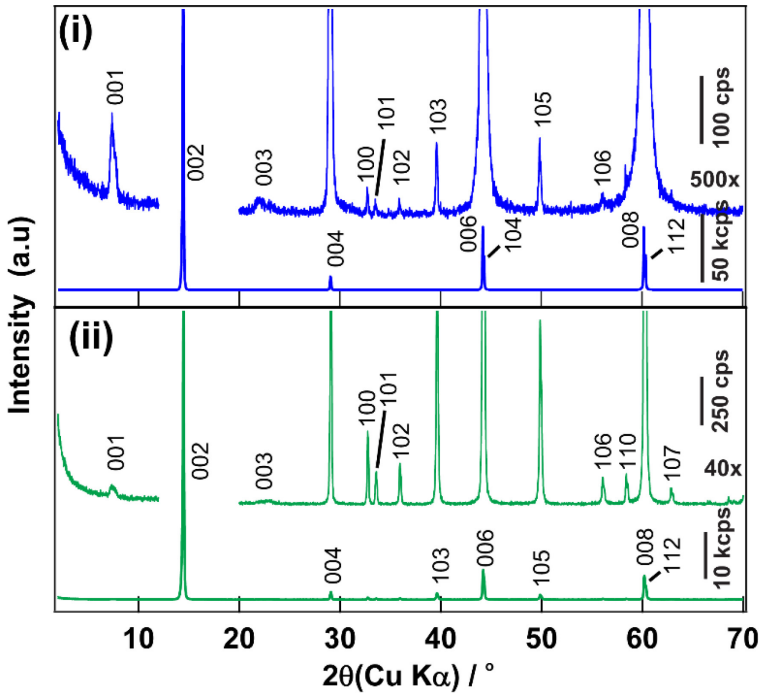

Figure A1.2. XRD patterns of (a) starting MoS_2 crystals and (b) pre-expanded MoS_2 crystals (the top patterns in (a) and (b) are the magnified plot of the bottom at 500 and 40 times, respectively).

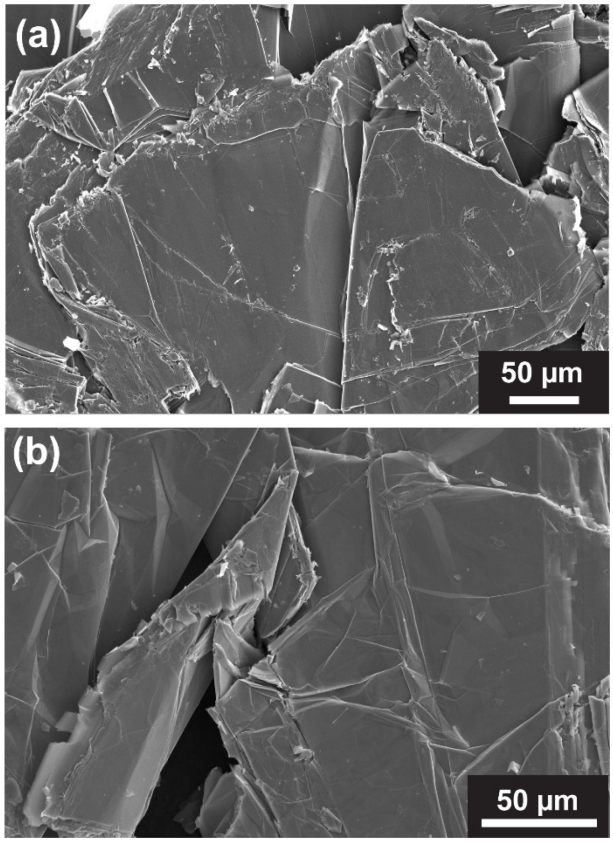

Figure A1.3. SEM image of (a) starting and (b) pre-expanded MoS_2 crystals.

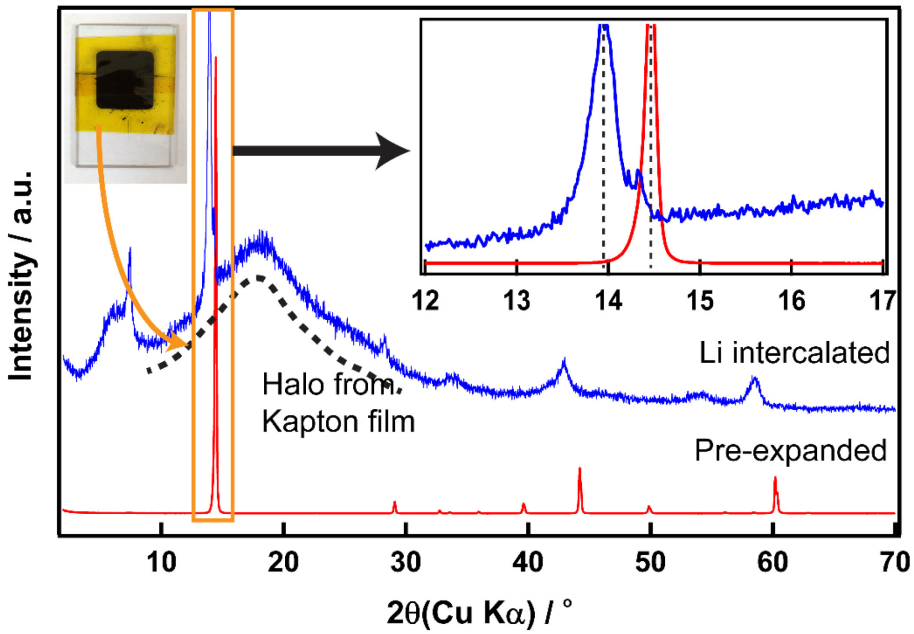

Figure A1.4. XRD patterns of MoS_2 crystals upon lithiation. Due self-heating nature in air, the specimen was covered with Kapton tape to isolate the sample from ambient air. The basal peak of the lithiated product ($2\theta \cong 14.4°$) shifted to a lower diffraction angle, indicating ~0.23 Å interlayer expansion.

A.1.3.2. Unilamellar MoS_2 Nanosheets Prepared from Chemical Exfoliation

Figure A1.5 depicts a typical AFM image of the as-exfoliated MoS_2 nanosheets, showing the successful delamination into unilamellar nanosheets. The lateral dimension of the nanosheets was 0.3-1 μm. The nanosheets exhibited a uniform thickness of ~1.2 nm, confirming the monolayer regime. The apparent thickness was approximately 0.5 nm larger than their crystallographic thicknesses (~0.65 nm),[3] which is attributed to water molecules adsorbed on both nanosheet surfaces.[4,5] Figure A1.6 displays the TEM image and corresponding SAED pattern of the as-prepared nanosheets, showing six-fold hexagonal spots with 2-fold periodicity along the (100) and (010) directions. The as-exfoliated MoS_2 exhibited $\sqrt{3}\times1$ superstructure based on a 2D rectangular cell. The structure can also be identified as 2×2 superstructure. Note that the lateral dimension of the as-exfoliated sheets can be considered relatively large. It is possible that the sheets may contain more than one microdomain.[6] The 2×2 superstructure can thus be understood due to twinning the $\sqrt{3}\times1$ sublattice by 3-fold rotation.[7] The SAED analysis is consistent with the in-plane XRD data. Thus, the $\sqrt{3}\times1$ superstructure be regarded as the intrinsic 2D structure of chemically exfoliated MoS_2.

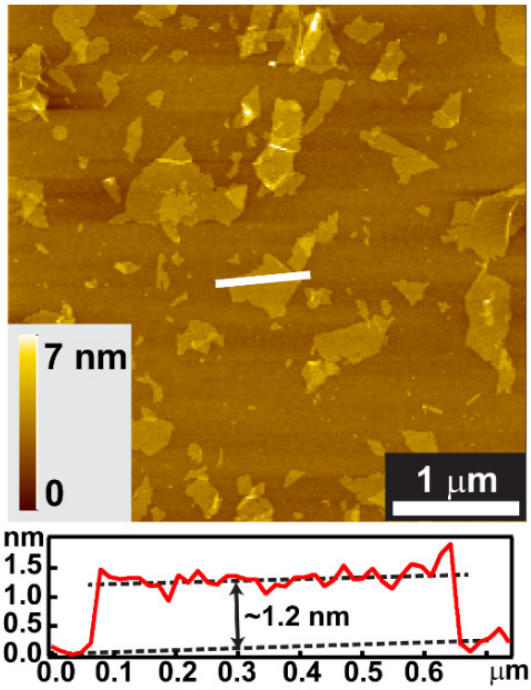

Figure A1.5. Typical AFM image of as-exfoliated MoS_2 nanosheets.

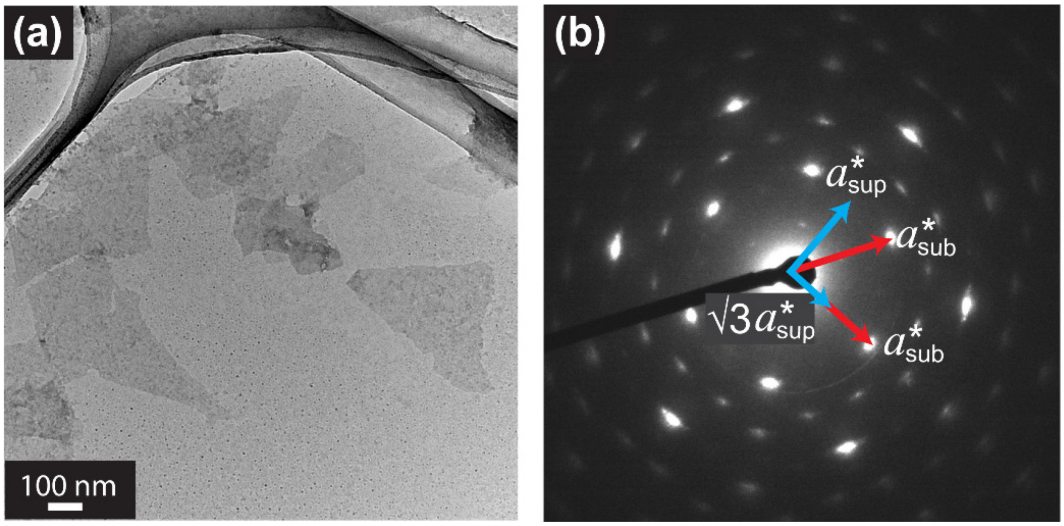

Figure A1.6. (a) TEM image and (b) corresponding SAED pattern of as-exfoliated MoS_2 nanosheets, giving rise to a $\sqrt{3}\times1$ superstructure.

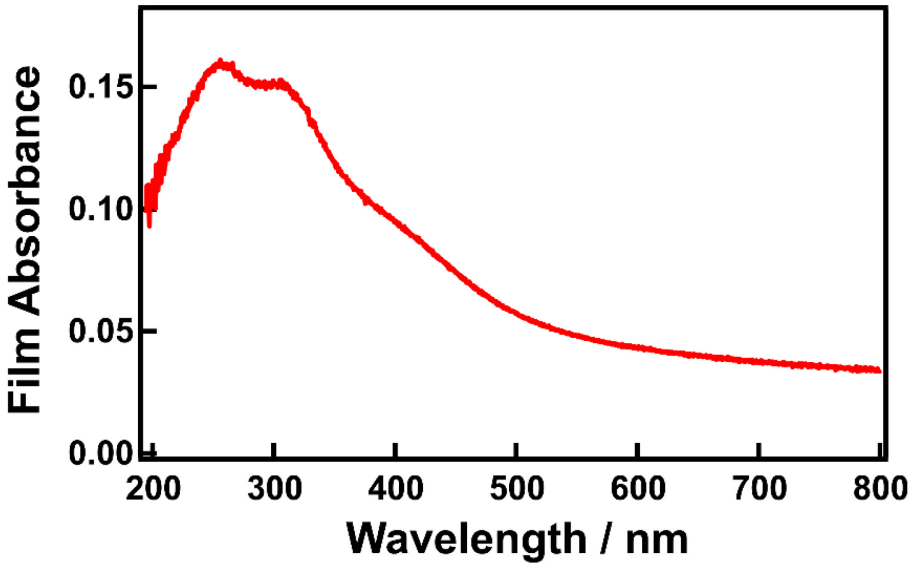

Figure A1.7. UV-visible spectra of a monolayer film of as-exfoliated MoS_2 nanosheets deposited on a quartz glass substrate. Monolayer film of MoS_2 nanosheets prepared from chemical exfoliation shows an absorbance ~0.1 at 400 nm.

A.1.3.3. Determining the Concentration of Exfoliated MoS_2

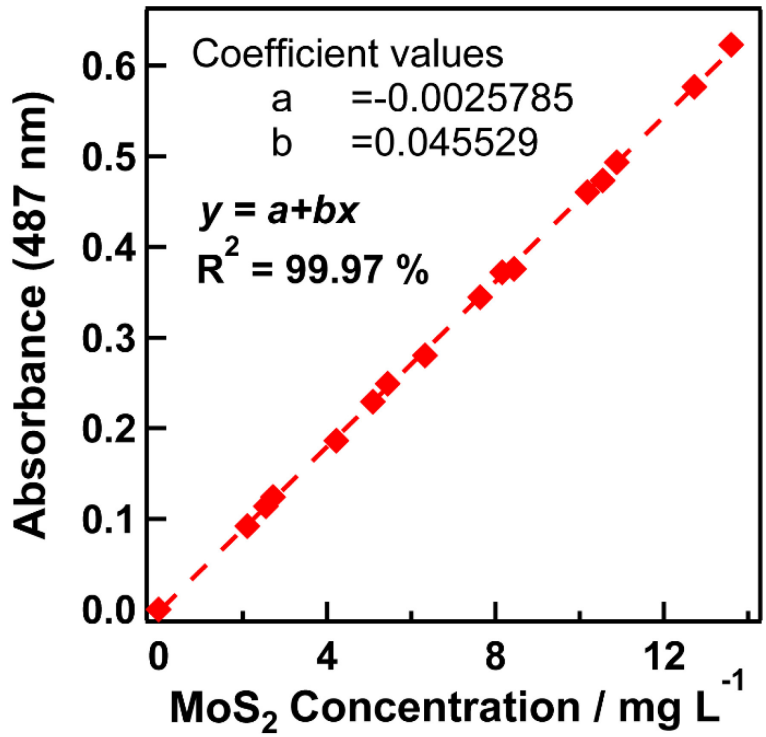

Figure A1.8. Standard curve of absorbance at 487 nm as a function of the concentration of MoS_2.

The concentration of the exfoliated MoS_2 suspension was determined using a chemical analysis (ICP-OES). The chemical analysis was performed immediately after the exfoliation to avoid any change in the suspension. The suspension was always stored in an inert N_2 atmosphere before the analysis. Simultaneously, a standard curve was prepared from the same suspension by measuring the UV-visible absorption spectrum. Throughout the research, the concentration of a newly prepared MoS_2 suspension was simply determined from the standard curve.

A.1.3.4. Dispersion Stability of As-Prepared MoS_2 Suspension

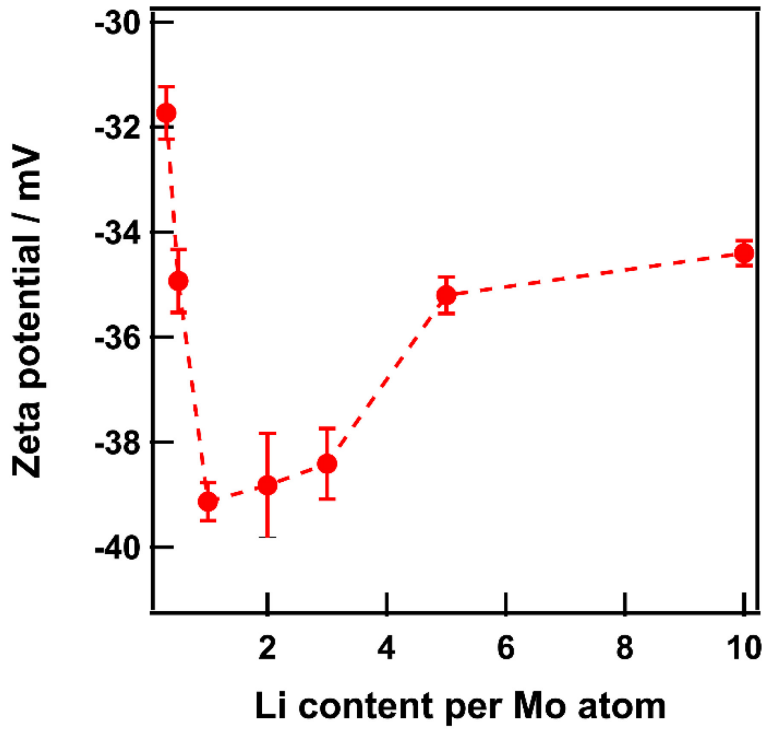

Figure A1.9. Zeta potential of MoS_2 nanosheets in aqueous suspensions as a function of Li content.

A good dispersion of chemically exfoliated MoS_2 nanosheets requires a specific amount of counter-ions to balance the negative charges. In this case, Li ions act as the counter-ions. The amount of Li ions in the as-prepared MoS_2 suspension was typically 0.2-0.25 per Mo atom. This value is comparable to those reported previously.[8–10] Figure A1.9 shows zeta potential values of the suspensions upon the adjustment of Li content. The values were more negative than −30 mV, indicating good dispersibility due to sufficient mutual repulsion.[11–13] The most stable dispersion of the as-prepared nanosheets was achieved at Li/Mo = 1.

A.1.3.5. Change in the Electronic and Chemical Nature upon Heating

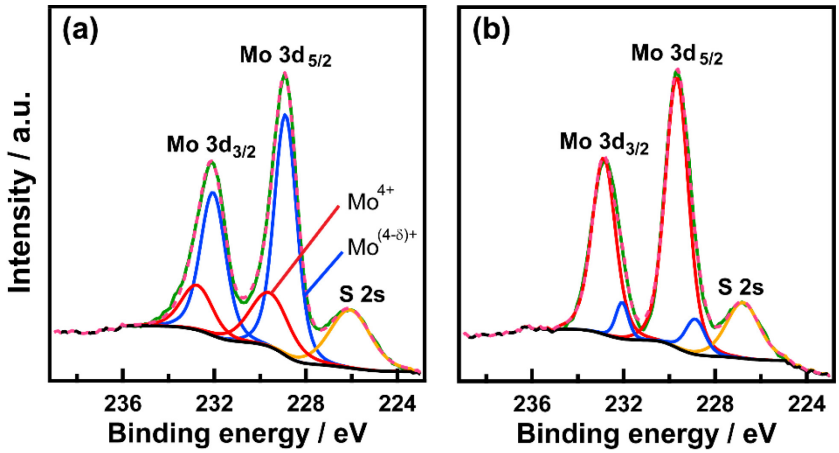

Figure A1.10. XPS spectra at the Mo 3d core levels of (a) freshly as-prepared MoS_2 nanosheets and (b) after annealing at 300 °C in Ar atmosphere.

We performed annealing on the freshly as-prepared MoS_2 nanosheets at 300 °C in Ar atmosphere in comparison to the freshly as-prepared on (Figure A1.10). Clearly, the oxidation state of the nanosheets restored to the original Mo^{4+}, with the proportion of more than 90%. This result is consistent with a previous report.[14]

A.1.3.6. Optical Properties after Heating

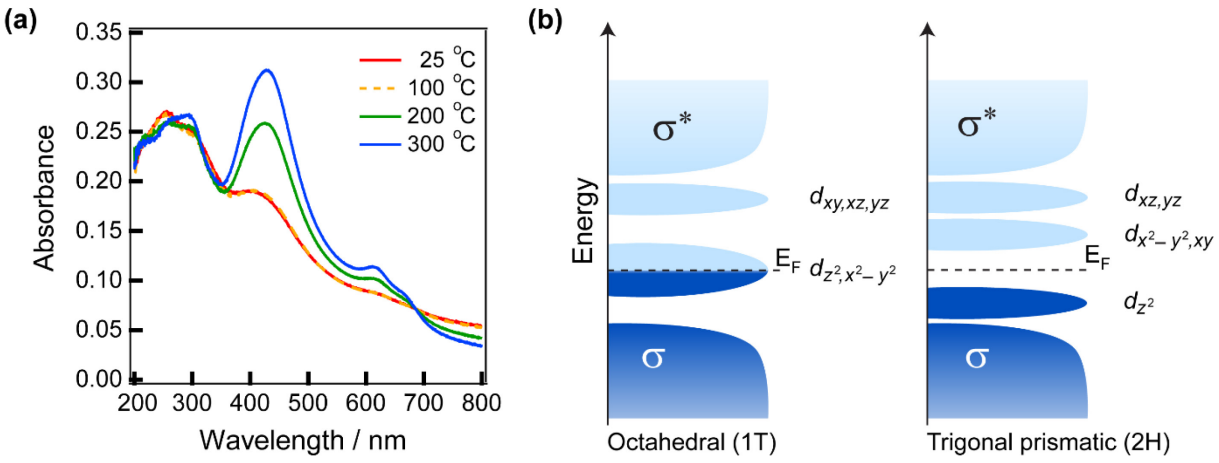

Figure A1.11. (a) UV-visible absorption spectra of a MoS_2 nanosheet film at different heating temperatures. The MoS_2 film was substantially in a monolayer although there is a possibility of overlaps to some extent.

(b) Simplified *d*-orbital filling within bonding (σ) and anti-bonding (σ*) states representing the electronic character of MoS_2 with different crystal structures.[15] Occupied and empty states are indicated in dark and light blue, respectively.

Figure A1.11a displays the UV-visible absorption spectra of a monolayer film of MoS_2 nanosheets as a function of the heating temperature. The freshly as-prepared nanosheets exhibited a prominent absorption near the UV region (200-350 nm), showing the high energy excitonic features.[14] The spectra from the visible region to the near infrared region revealed the free-carrier-like broad absorption feature, which indicates the metallic character of the as-prepared chemically exfoliated MoS_2.[16] Upon annealing, two prominent absorption peaks were progressively observed at approximately 600-700 nm, which arise from the A and B band-edge excitons at the *K* point of the Brillouin zone. This corresponds to the interband transitions from the filled dz^2 orbitals to the empty $dx^2–y^2,xy$. The absorption bands at 400-500 nm can be ascribed to the C and D interband transitions from the dz^2 to the dxz,xy orbitals.[14,16,17] The evolution of these absorption features indicates the structural restoration from 1T to 2H.

A1.4. Summary

In summary, unilamellar MoS_2 nanosheets have been successfully prepared *via* chemical exfoliation method.

A1.5. References

[1] J. Zheng, H. Zhang, S. Dong, Y. Liu, C. T. Nai, H. S. Shin, H. Y. Jeong, B. Liu, K. P. Loh, *Nat. Commun.* **2014**, *5*, 2995.

[2] P. Joensen, R. F. Frindt, S. R. Morrison, *Mater. Res. Bull.* **1986**, *21*, 457–461.

[3] R. G. Dickinson, L. Pauling, *J. Am. Chem. Soc.* **1923**, *45*, 1466–1471.

[4] T. Sasaki, Y. Ebina, Y. Kitami, M. Watanabe, T. Oikawa, *J. Phys. Chem. B* **2001**, *105*, 6116–6121.

[5] T. Tanaka, Y. Ebina, K. Takada, K. Kurashima, T. Sasaki, *Chem. Mater.* **2003**, *15*, 3564–3568.

[6] F. Wypych, C. Solenthaler, R. Prins, T. Weber, *J. Solid State Chem.* **1999**, *144*, 430–436.

[7] J. Heising, M. G. Kanatzidis, *J. Am. Chem. Soc.* **1999**, *121*, 638–643.

[8] S. S. Chou, M. De, J. Kim, S. Byun, C. Dykstra, J. Yu, J. Huang, V. P. Dravid, *J. Am. Chem. Soc.* **2013**, *135*, 4584–4587.

[9] J. Heising, M. G. Kanatzidis, *J. Am. Chem. Soc.* **1999**, *121*, 11720–11732.

[10] A. S. Golub', G. A. Protsenko, L. V. Gumileva, A. G. Buyanovskaya, Y. N. Novikov, *Russ. Chem. Bull.* **1993**, *42*, 632–634.

[11] A. Gupta, V. Arunachalam, S. Vasudevan, *J. Phys. Chem. Lett.* **2015**, *6*, 739–744.

[12] D. H. Everett, *Basic Principles of Colloid Science*, Royal Society Of Chemistry, Cambridge, **1988**.

[13] D. Li, M. B. Müller, S. Gilje, R. B. Kaner, G. G. Wallace, *Nat. Nanotechnol.* **2008**, *3*, 101–105.

[14] G. Eda, H. Yamaguchi, D. Voiry, T. Fujita, M. Chen, M. Chhowalla, *Nano Lett.* **2011**, *11*, 5111–5116.

[15] M. Chhowalla, H. S. Shin, G. Eda, L.-J. Li, K. P. Loh, H. Zhang, *Nat. Chem.* **2013**, *5*, 263–75.

[16] W. Zhao, R. M. Ribeiro, G. Eda, *Acc. Chem. Res.* **2015**, *48*, 91–9.

[17] L. A. King, W. Zhao, M. Chhowalla, D. J. Riley, G. Eda, *J. Mater. Chem. A* **2013**, *1*, 8935.

Appendix 2.
Preparation of $Ti_{0.87}O_2^{0.52-}$ Nanosheets

This chapter is devoted to describe the preparation of $Ti_{0.87}O_2^{0.52-}$ nanosheets used throughout the research.

A2.1. Preparation Methods

The detailed procedure for the preparation of $Ti_{0.87}O_2^{0.52-}$ nanosheets was reported in the previous report.[1,2] The parent material of $K_{0.8}Ti_{1.73}Li_{0.27}O_2$ was synthesized *via* a conventional solid-state calcining process.[1] K_2CO_3, TiO_2, and Li_2CO_3 powders were mixed and intimately ground in a mortar at a molar ratio of 0.4:1.73:0.135 and subjected to decarbonation by heating at 800 °C for 1 h. After cooling down to a room temperature, the mixture of powders was ground and calcined at 1000 °C for 20 h. The phase formation and the purity of the final product, $K_{0.8}Ti_{1.73}Li_{0.27}O_2$, were confirmed using XRD. In the second step, 20 g of the $K_{0.8}Ti_{1.73}Li_{0.27}O_2$ powder was subjected to acid exchange to form a protonated phase ($H_{1.07}Ti_{1.73}O_4{\cdot}H_2O$), by treating with 1 dm^3 of a 1 mol dm^{-3} HCl solution for 72 h. The HCl solution was decanted and replaced daily with a fresh solution. The resulting $H_{1.07}Ti_{1.73}O_4{\cdot}H_2O$ (4 g) was exfoliated in 1 dm^3 of a 0.026 mol dm^{-3} tetrabutylammonium hydroxide solution with a reciprocal agitator at 180 rpm for 7 days.

A2.2. Characterization

The morphology, lateral size, and thickness of the exfoliated $Ti_{0.87}O_2^{0.52-}$ nanosheets were examined with a Hitachi SPA 400 AFM. UV-visible spectra of the suspensions were measured with a Hitachi U-4100 spectrophotometer.

A2.3. Results

Unilamellar $Ti_{0.87}O_2^{0.52-}$ nanosheets has been successfully obtained. Figure A2.1 displays a typical AFM image of the nanosheets, showing monodisperse unilamellar nanosheets with the thickness of 1.1 nm and lateral size of 0.3-2 μm. UV-vis absorption spectra of the nanosheets showed a sharp absorption feature in the UV region with a peak top at 265 nm (Figure A2.2). Such a unique feature confirm the unilamellar character of the obtained $Ti_{0.87}O_2^{0.52-}$ nanosheets.

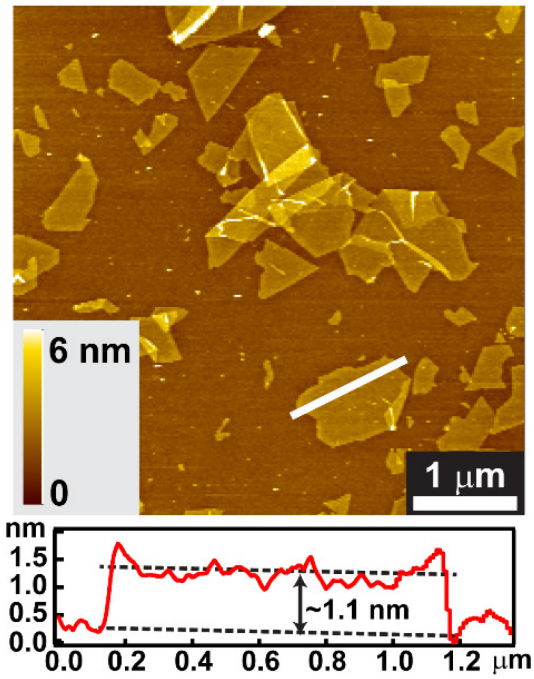

Figure A2.1. Typical AFM image of as-exfoliated $Ti_{0.87}O_2^{0.52-}$ nanosheets.

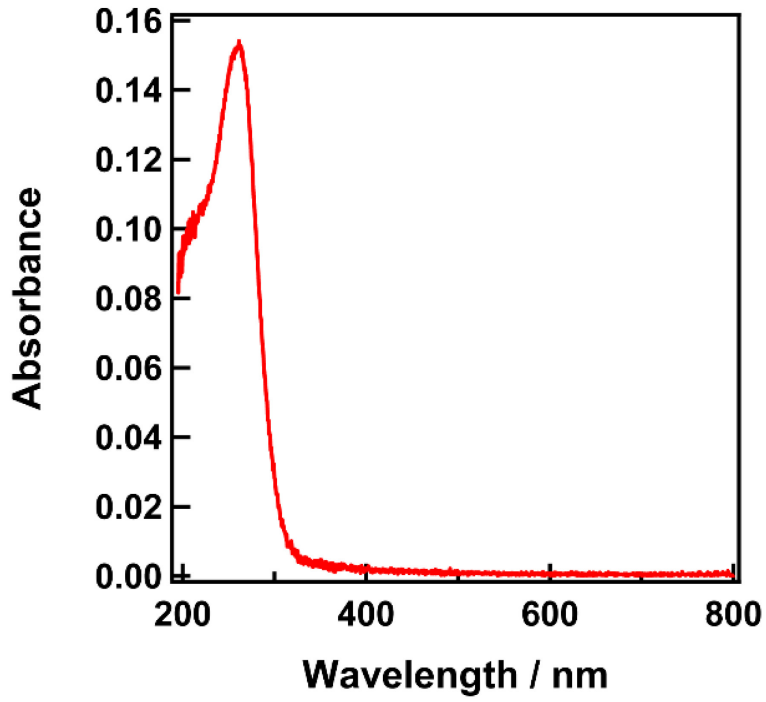

Figure A2.2. Typical UV-vis absorption spectra of unilamellar $Ti_{0.87}O_2^{0.52-}$ nanosheets.

A2.4. References

[1] T. Sasaki, F. Kooli, M. Iida, Y. Michiue, S. Takenouchi, Y. Yajima, F. Izumi, B. C. Chakoumakos, M. Watanabe, *Chem. Mater.* **1998**, *10*, 4123–4128.

[2] T. Sasaki, M. Watanabe, *J. Am. Chem. Soc.* **1998**, *120*, 4682–4689.

Appendix 3.
Control Experiments for the Photocatalytic Hydrogen Generation

This chapter is devoted to describe the experimental procedures for the sample preparation of physical mixtures of bulk aggregates of $Ti_{0.87}O_2^{0.52-}/MoS_2$ nanosheets and composites of TiO_2-nanoparticles/MoS_2. The tests for the photocatalytic hydrogen generation were carried out using the same procedure for the 2D-heterointerface sample described in Chapter 3, sub-section 3.3.6.

A3.1. Preparation Methods

Physical mixtures of bulk aggregates of independently flocculated $Ti_{0.87}O_2^{0.52-}$/1T-MoS_2. Figure A3.1 shows the schematic diagram of the sample preparation. Colloidal suspensions of 1T-phase MoS_2 and $Ti_{0.87}O_2^{0.52-}$ nanosheets were separately flocculated with the addition of HCl. They were subsequently mixed under vigorous stirring at a designated proportion. The mixtures were then recovered by centrifugation, washed with water, and freeze dried.

Composites of TiO_2-nanoparticles/1T-MoS_2. Figure A3.2 depicts the schematic diagram of the sample preparation for TiO_2/1T-MoS_2 composites. Commercial P25 nanoparticles were used as the TiO_2 nanoparticles. First, the TiO_2 nanoparticles were dispersed in water (0.2 g dm^{-3}) under ultrasonication. Subsequently, a 2 cm^{-3} HCl solution (0.5 mol dm^{-3}) was added to a 200 cm^{-2} TiO_2 dispersion (pH = ~2.3). Under this condition, the resultant dispersion was fairly stable, as indicated by the zeta potential value of >30 mV. No sedimentation was observed. A designated amount of 1T-phase MoS_2 was then added to the dispersion, yielding a sedimentation of mixtures of TiO_2/MoS_2. Through this process, the MoS_2 nanosheets were expected to wrap the TiO_2 nanoparticles. The resulting mixtures were then recovered by centrifugation, washed with water, and freeze dried.

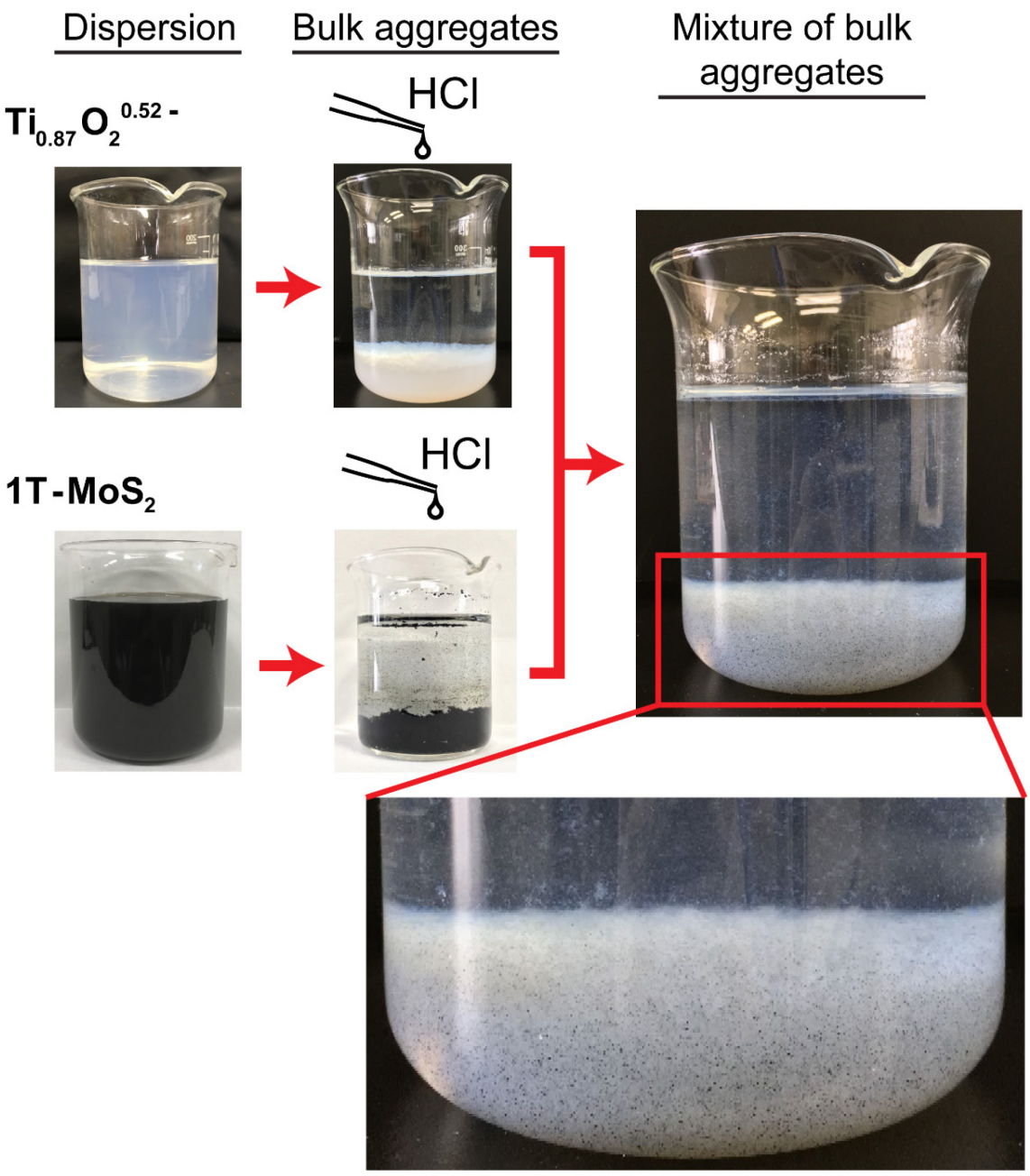

Figure A3.1. Schematic diagram for the preparation of mixtures of bulk-aggregates of independently flocculated $Ti_{0.87}O_2^{0.52-}$/1T-MoS_2 nanosheets. Clearly, the MoS_2 aggregates are inhomogeneously distributed within the mixture.

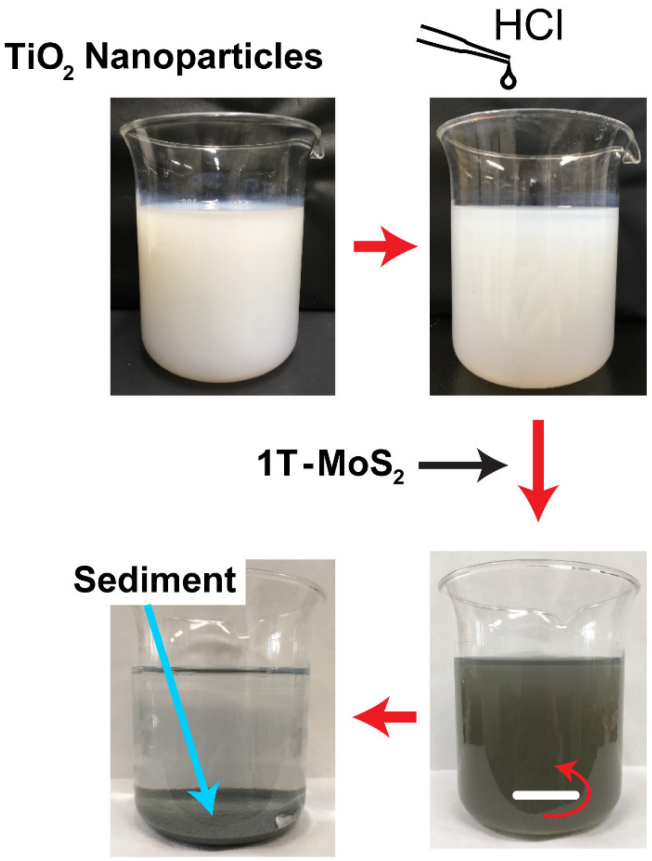

Figure A3.2. Schematic diagram for the preparation of TiO_2-nanoparticles/1T-MoS_2 composites.

A3.2. Results

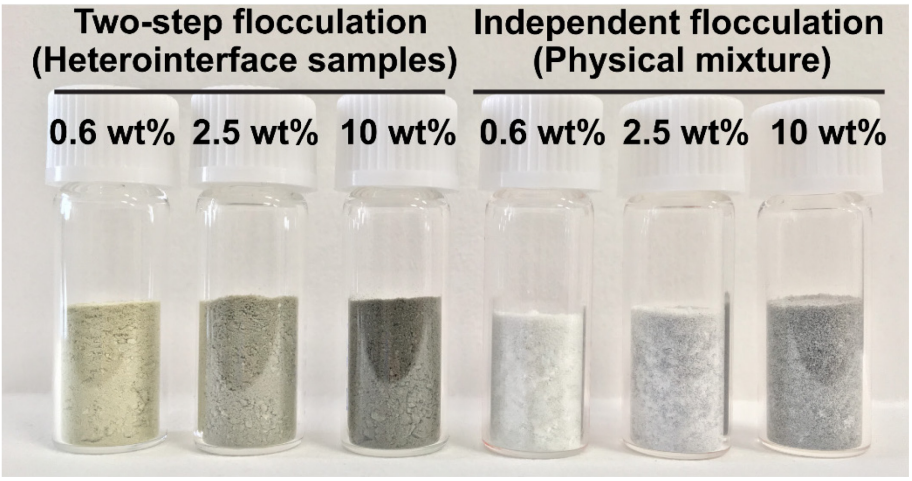

Figure A3.3. The appearance of the 2D-heterointerface samples obtained from the two-step flocculation (left), in comparison to the samples prepared from physical mixtures of bulk-aggregated $Ti_{0.87}O_2^{0.52-}$/1T-MoS_2 nanosheets (right). They were synthesized at a range of loading amount of MoS_2 (0.6-10 wt%).

Different from the 2D-heterointerface samples, the samples obtained from the physical mixtures of independently flocculated nanosheets showed a non-uniform grayish color (Figure A3.3). This indicates that "face-to-face" interfacial contact between the individually restacked nanosheets was hardly realized at the nanoscale by the simple mixing.

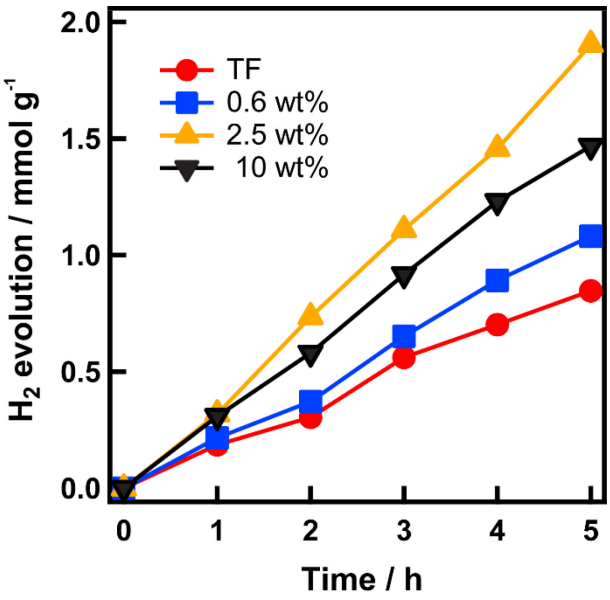

Figure A3.4. Time course of H_2 evolution over control samples from the physical mixtures of bulk-aggregated $Ti_{0.87}O_2^{0.52-}$/1T-MoS_2 nanosheets. The highest photocatalytic activity was achieved at ~0.38 mmol h^{-1} g^{-1} from the sample with a 2.5 wt% MoS_2 loading.

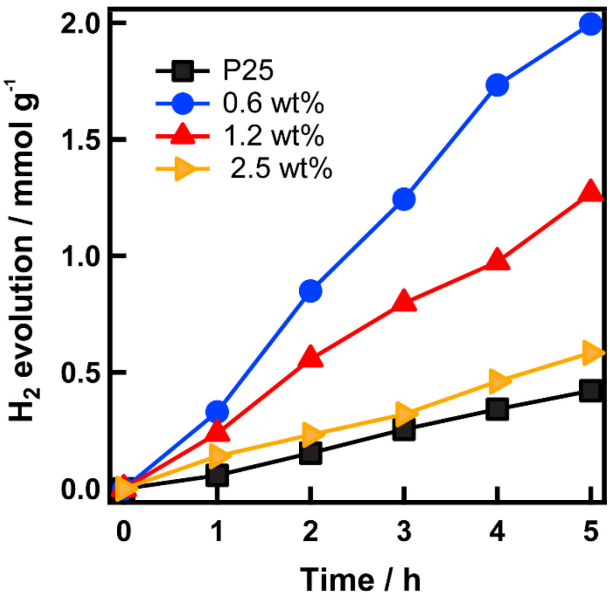

Figure A3.5. Time course of H_2 evolution over TiO_2-nanoparticles/1T-MoS_2 composites. The highest photocatalytic activity was achieved at ~0.4 mmol h^{-1} g^{-1} from the sample with a 0.6 wt% MoS_2 loading.

Figure A3.4 and Figure A3.5 display the photocatalytic activities of the two-designed control samples. The highest activities were ~0.38 and ~0.4 mmol h^{-1} g^{-1} for the physical mixtures of bulk-aggregated $Ti_{0.87}O_2^{0.52-}$/1T-MoS_2 nanosheets and TiO_2-nanoparticles/1T-MoS_2 composites, respectively. The activities were three times lower than that of the 2D-heterointerface samples of restacked-$Ti_{0.87}O_2^{0.52-}$/1T-MoS_2 nanosheets.

List of Publication

1. L. Nurdiwijayanto, R. Ma, N. Sakai and T. Sasaki. Stability and Nature of Chemically Exfoliated MoS_2 in Aqueous Suspensions. *Inorg. Chem.* 2017, 56, 7620–7623.
2. L. Nurdiwijayanto, R. Ma, N. Sakai and T. Sasaki. Insight into the Structural and Electronic Nature of Chemically Exfoliated Molybdenum Disulfide Nanosheets in Aqueous Dispersions. *Dalton Trans.* 2018, 47, 3014–3021.
3. X. Pan, R. Ma, N. Sakai, L. Nurdiwijayanto, and T. Sasaki. A Unilamellar Metallic MoS_2/Graphene Superlattice for Efficient Sodium Storage and Hydrogen Evolution. *ACS Energy Lett.* 2018, 3, 997−1005.
4. L. Nurdiwijayanto, J. Wu, N. Sakai, R. Ma, Y. Ebina, and T. Sasaki. Monolayer Cocatalyst of Metallic MoS_2 on Restacked Titania Nanosheets for Efficient Photocatalytic Hydrogen Generation. 2018, *(Submitted)*.

Acknowledgement

Foremost, I would like to express my deepest gratitude to my supervisor, Prof. Takayoshi Sasaki, for the opportunity of conducting doctoral research in Soft Chemistry Group, WPI-MANA, NIMS. The understanding of fundamental knowledge and scientific research from Prof. Sasaki is excellent. I received a lot of benefit from fruitful discussions with him. I am also greatly indebted to his guidance and patience in shaping and improving my writing and presentation skills. I can feel that my writing and presentation skills gradually improved during this research work, although my skills are still far from perfect. I greatly appreciate his continuous support, motivation, encouragement, helpful guidance and suggestion on my Ph.D. study. Without his help and direction, I might not be able to finish this thesis.

I would also like to express my sincere gratitude to the researchers as well as my collaborators in Soft Chemistry Group: Dr. R. Ma, Dr. N. Sakai, Dr. Y. Ebina, Dr. J. Wu, and Dr. X. Pan. I really appreciated their supports to include research directions, experimental techniques, data analyses and presentations, and paper writings. The knowledge and skills they taught are very important for my future career. Especially, Dr. Ma and Dr. Sakai have significant contribution in helping me to improve the quality of the published papers. Dr. Wu taught me in the chemical exfoliation of MoS_2. We also had a collaboration in the hybridization of MoS_2 and titania nanosheets. Dr. Pan helped and taught me in the sample preparation and electrochemical measurement for Li-ion battery.

My great appreciation also goes to Prof. Takao Mori, Prof. Naoki Fukata, and Prof. Takahiro Kondo as the committee of my Ph.D thesis. Thank you for the time that the committee spent in evaluating my Ph.D thesis and defense.

I acknowledge NIMS for providing the financial support as a NIMS junior researcher.

I would like to express my appreciation to all lab members: Dr. N. Iyi, Dr. M. Osada, Dr. T. Taniguchi, Dr. M. Shuaib Khan, Dr. Andrés, Dr. M. Mazur, Dr. P. Sun, Dr. W. Ma, Dr. C. Xingke, Ms. E. Yokota, Ms. Y. Ohashi, Dr. X. Li, Dr. X. Lu, Ms. Y. Song, Mr. H. Trevyn, Mr. X. Zhou, Mr. F. Chen, Mr. Y. Lin, Mr. H. Wan, Mr. T. Hoshide, Mr. K. Kamanaka, Mr. K. Inoue, Ms. H. Yano, and Mr. T. Kikuchi. Especially, Mr. Kamanaka, Mr. Inoue, and Ms. Yano have helped me in ordering chemical reagents and experimental apparatuses. Ms. Yokota and Ms. Song often helped me with Japanese, especially those related to the thesis defense application. Dr. Iyi have helped me with FTIR measurement and analysis using his instrument. Dr. Osada and Dr. Taniguchi have allowed me to use their Raman instrument as well as taught me how to operate. Mr. Hoshide taught me in the synthesize of titania nanosheets. Mr. Chen and Mr. Wan helped and taught me with the electrochemical measurement. Ms. Yokota and Ms. Ohashi have provided me a lot of assistance, especially to deal with the official matters.

I also thank many close friends who have helped me in any way during my stay in Japan and made the life abroad easier.

Last, but not least, I would like to thank my family, to which this thesis is dedicated, for their continuous support, encouragement, patient, love, and best wishes (*du'a*).